A novel mini pressure swing adsorption plant for oxygen concentration

JNCASR

Ritwik Das

Engineering Mechanics Unit
Jawaharlal Nehru Centre for Advanced Scientific Research

This dissertation is submitted for the degree of
M.S.(Engg.)

May 2023

I would like to dedicate this thesis to my late grandfather …

Declaration

I declare that the matter embodied in the thesis entitled **"A novel mini pressure swing adsorption plant for oxygen concentration"** is the result of investigations carried out by me at the Engineering Mechanics Unit, Jawaharlal Nehru Centre for Advanced Scientific Research, Bangalore, India under the supervision of Dr. Diwakar S. Venkatesan and that it has not been submitted elsewhere for the award of any degree or diploma

In keeping with the general practice in reporting scientific observations, due acknowledgement has been made whenever the work described is based on the findings of other investigators.

Ritwik Das.

Ritwik Das
May 2023

CERTIFICATE

I hereby certify that the matter embodied in this thesis entitled **A novel mini pressure swing adsorption plant for oxygen concentration** has been carried out by **Mr. Ritwik Das** at the Engineering Mechanics Unit, Jawaharlal Nehru Centre for Advanced Scientific Research, Bengaluru, India under my supervision and that it has not been submitted elsewhere for the award of any degree or diploma.

Dr. Diwakar S. Venkatesan
(Research Supervisor)

Acknowledgements

I would like to thank the institute and the people who have played key roles in the successful completion of this research work.

I sincerely wish to thank my research supervisor Dr Diwakar S. Venkatesan, for accepting me as his student, imparting his knowledge and guiding me through the research. I would also like to acknowledge him for his constant support and continuous motivation and for teaching me some of the basic human intellects. Throughout my M.S, I cherished the freedom I had while working with him; it was an experience of a lifetime.

I would also like to take this opportunity to thank Prof. Arvind Rajendran for valuable discussions and suggestions about my research work.

I would like to thank Prof. Santosh Ansumali, Prof. Ganesh Subramaniam, Prof. K.R.Sreenivas and Prof. Meheboob Alam for their untiring and honest efforts in teaching the subject fundamentals during the coursework.

I would like to thank Dr Abhijit Dhamanekar for his constant support, supervision and advice in the project.

Again I'd thank my advisor for giving me the opportunity to undertake challenging work and for his belief in my ability from the beginning. I earnestly thank him and my lab mates and colleagues for their enthusiastic participation in discussions and important suggestions at crucial points in my research.

The support extended by Mr Arun Kumar (Eiwave Digitech) for his help with the electronics side of the setup of the PSA process used in this thesis. He was extremely helpful in providing the necessary improvements to the apparatus to allow me to conduct the experiments I wished to perform.

My special thanks go to my dear friends Poulami Goswami, Saumyakanta Mishra, Suryadev Pratap Singh, Pavan Singeetham, Prateek Anand, and Anomitra Saha. I wish to thank them for scientific and non-scientific discussions, which have helped me become a better human.

Finally, I would like to thank my parents and family for their unwavering support

Abstract

The second wave of COVID-19 led to a severe scarcity of medical oxygen in the country, as cryogenic distillation plants could not entirely meet the exigent oxygen requirements for medical usage. Consequently, there has been a growing impetus to utilise the non-cryogenic air separation process for medical oxygen generation. In this regard, the pressure swing adsorption (PSA) process has emerged as a practical and suitable substitute for cryogenic distillation in separating oxygen from the air.

The goal of the current work is to design, develop, and optimise a novel mini PSA plant that is pertinent to the conditions of a country like India. The device, thus developed, is configured to be portable and will provide at least 40 litres of oxygen per minute to support a minimum of 6 to 8 patients in a small hospital scenario. The device is rugged with medical-grade components and can handle both lithium-based and sodium-based zeolites.

The overall procedure involved designing and testing multiple versions of the device, starting from tabletop models with LiX (X represents aluminosilicate) zeolite to a current experimental design with NaX zeolite as the adsorbent. A typical PSA cycle is essentially controlled by three parameters: pressurisation, purge, and equalisation times, which are the duration of different processes involved in the cycle. In the current work, we have carried out parametric studies on each version of the experimental setup by varying the above three times for the given input and output conditions. Each subsequent version of the device was evolved to address the issues faced by all the earlier designs. This finally led to the development of the device's final version that provided a 92% enhanced oxygen stream at 40-45 litres per minute. It was observed from the different experimental trials that the critical design factors of the adsorption column are two: one, the length-to-diameter ratio (l/d) and the second, the dead volume. We observed experimentally that the 'l/d' ratio should be between 4 and 6 to avoid both flow mal-distribution and large pressure drop inside the adsorbent column. Consequently, for the final experimental setup, the l/d ratio is 5.71. Note that the dead volume of the zeolite cylinder should be as low as possible (0.16% for the present experimental design) to avoid mixing trapped nitrogen with the oxygen-enriched air.

For the final design, we conducted a systematic parametric study at different output flow rates to determine the optimum value of the three important time scales. Correspondingly,

the three flow times (pressurisation, purge and equalisation times) are 30, 2 and 4 seconds, respectively.

In the second part of our work, we have developed a detailed mathematical model to reproduce our experimental results. These simulations have been performed using ANSYS FLUENT package with the integration of the adsorption kinetics through different adsorption isotherm models via specialised User Defined Functions (UDFs). A simplified axisymmetric configuration, corresponding to our experimental setup, has been evolved to mimic the behaviour of the complete PSA system. The current numerical model has been thoroughly validated by simulating different breakthrough curves reported in the literature. The results obtained using the modified Langmuir-Freundlich isotherm successfully reproduces our experimental results. Apart from providing an understanding of the intrinsic operation of the device, these numerical simulations offer further scope for optimising the device.

Table of contents

List of figures

List of tables

Chapter 1

Introduction

1.1 General overview

The end of year 2019 saw the outbreak of a new kind of respiratory disease that was first identified in Wuhan, China. This highly contagious disease, called Corona Virus Disease 2019 (COVID-2019), is caused by the Severe Acute Respiratory Syndrome Corona Virus-2 (SARS-CoV-2). The often observed symptoms of COVID-19 include shortness of breath, fever, loss of smell and taste, etc.

According to [6] the initial wave of COVID-19 infections reached its peak in September 2020, and the first case of COVID-19 was reported in India on January 30th, 2020. The second wave of COVID-19, which was even more severe, started in March 2021 and led to a severe scarcity of medical oxygen in the country. As the second COVID wave surged, all health care facilities, from small nursing homes to large private and public hospitals, struggled to provide necessary patient care. With a significant number of patients presenting symptoms more severe than those observed in the first wave, oxygen resources were depleting at a much faster level. Many prudent steps were taken by the competent authorities to address the issue. Of these, the most notable initiatives include the localised development of oxygen concentrators that work on the Pressure Swing Adsorption (PSA) process. The current work deals with one such initiative wherein a novel PSA device has been developed to address the specific demands of Tier-II and Tier-III cities/towns in the country. Before proceeding to understand the design and characterisation of this new device, the various factors that have motivated the present work are discussed in this chapter.

1.2 Oxygen scenario in India before and during the pandemic

We now begin our discussions by looking at the country's oxygen demand and supply scenario before and during the second wave of COVID-19.

1.2.1 Before the pandemic

The pre-COVID daily oxygen production/consumption data in India is shown in Table 1.1. The total production of oxygen was recorded as 7200 metric tonnes, of which 59.6% of the total oxygen was required for industrial use, 16.8% of the oxygen was required for medical use, and approximately, 23.6% of the total oxygen was recorded as the excess capacity.

Capacity	**Pre-COVID Scenario**
Total Production capacity	7200 MT
Industrial usage	4290 MT
Medical usage	1210 MT
Excess capacity	1700 MT

Table 1.1 Pre-COVID oxygen scenario

Industrial use

Within the industrial category, the oxygen use and purity requirement vary based on the type of industry. A few of these scenarios are given below.

- Steel/Metal Industry: The steel industry is one of the leading oxygen consumers. Modern steel/metal making relies largely on the use of oxygen in blast furnaces and open-hearth furnaces to enrich air and enhance combustion efficiency. Oxygen enrichment helps increase the production capacity and, at the same time, reduce energy requirements. Also, it allows for the replacement of coke with other combustible materials.
- Chemical Industry: Oxygen is used as a raw material in a wide range of oxidation processes in the petroleum, chemical, and pharmaceutical industries. The rundown

incorporates the development of ethylene oxide, propylene oxide, union gas from halfway oxidation of a large number of hydrocarbons including coal, ethylene dichloride, hydrogen peroxide, nitric corrosive, vinyl chloride, phthalic corrosive, and so on.

- Pulp and Paper industry: Oxygen is essentially used as a bleaching agent in the pulp and paper industry. Though chlorine has been employed in the past, new oxygen-based techniques are now being used to reduce water contamination. The use of oxygen in the oxidation of black liquor minimises the amount of sulfur pollutants released into the atmosphere.
- Environmental use: The use of oxygen, rather than air, in waste-water treatment allows the existing treatment plants to expand their capacity. Injecting oxygen into sewers minimises the generation of hydrogen sulfide, thereby reducing corrosion and stink. The use of oxygenated water is an essential practice in aquaculture for breeding fish and other aquatic life forms.

Medical Use

Apart from the various industrial applications described above, high purity oxygen forms an integral part of the healthcare systems/infrastructure. It is an essential medicine and is employed in a variety of medical scenarios like surgeries, trauma care, neonatal care, childbirth, elderly care, and treatment of respiratory illnesses such as pneumonia, COVID-19, etc. The World Health Organization (WHO) has stipulated guidelines on O_2 purity requirements for different medical applications. Only devices used for oxygen therapy are allowed to have a purity as low as 82%. In all the other cases, the use of high purity (>90%) medical grade oxygen is mandated.

Until the second wave of COVID-19 hit the country, the overall oxygen requirement for both industrial and medical uses was primarily met by cryogenic distillation. The process exploits the difference in the boiling points of air constituents to separate and purify them. The details of the procedure are briefly explained in Chapter 2. The sophistication involved in this procedure makes it economically viable only when done at large industrial scales. The high purity liquid oxygen is often directly supplied to large hospitals having proper storage/conversion/distribution facilities. A typical hospital-side infrastructure is shown in Fig. 1.1. In the case of smaller hospitals, intermediaries facilitate the liquid-to-gas conversion process and supply oxygen through pressurised cylinders.

Fig. 1.1 Typical LOX and Compressed O_2 Cylinder system in a large hospital setup

1.2.2 During the pandemic

The COVID-19 pandemic uncovered a serious flaw in the above medical oxygen production and distribution systems, i.e., its in-elasticity. Despite the best efforts by various authorities to deliver medical oxygen, demand outstripped the supply during the pandemic, and infected patients were left to struggle as hospitals in several jurisdictions ran out of medical oxygen. In India, demand for medical oxygen soared when the state of Maharashtra began to see an increase in the COVID-19 cases in February 2021. The situation deteriorated when the second COVID wave further spread in March 2021. The country's medical oxygen demand peaked (Fig. 1.2) beyond 10,000 MT/day in the month of May 2021, up from 2,000 MT/day in the first week of April 2021.

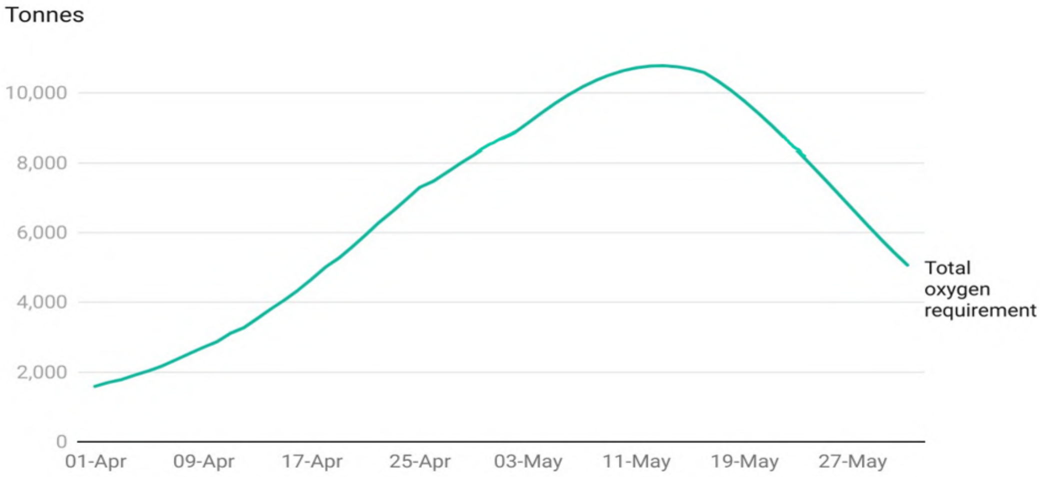

Fig. 1.2 Oxygen crisis during the second wave in India[34]

Given that several hospitals were experiencing scarcity simultaneously, the delivery of liquid oxygen using tankers became a logistical nightmare. Many lives were lost due to the delay in oxygen delivery. Notably, medical institutions and healthcare centers in rural/Tier-III locations suffered significantly more as it took a long time for the oxygen supply network to fulfill their requirements. Overall, the crisis highlighted the urgent need for diversified/localised oxygen generation. In this regard, the bulkiness of cryogenic plants makes them economically impractical for small-scale/distributed operations, even though the process is the cost-effective in large-scales. Consequently, there has been a growing interest in using different non-cryogenic techniques for localised oxygen generation.

1.3 Non-cryogenic separation process

Unlike cryogenic plants, the non-cryogenic air separation procedures are processed at near-room temperature conditions and at pressures slightly higher than atmospheric pressure. The technique essentially exploits differences in some chemical/physical properties other than the boiling point (cryogenic distillation) to separate the gases. The common technologies utilised in non-cryogenic air separation facilities are

I Adsorption process

II Membrane separation

III Chemical process

The non-cryogenic procedures may not result in ultra-high pure products in one step, as in the case of cryogenic distillation. Nevertheless, the purity obtained is sufficient for the majority of practical applications. Typical non-cryogenic air separators working on the zeolite-based PSA process can give up to 95.5% pure oxygen. Those operating using Carbon Molecular Sieves (CMS) can yield a maximum purity of 99.5 % pure nitrogen. These products can be further processed to obtain higher purity in case of necessity. Cryogenic plants may be energy efficient at the scale at which they operate. However, non-cryogenic plants are smaller, simpler, and less expensive, and they require lower power to operate. They also come in handy when the demand is not continuous, as they are very swift to boot up. In the present work, our focus is on the popular adsorption-based systems, briefly described in the following section.

1.4 Air separation using adsorption

Air containing different gas components can be filtrated into its significant components depending on the selective adsorption of gases on specific zeolite materials. For instance, sequestration of nitrogen over O_2 and Ar can result in oxygen separation on an adsorbent material. Due to the higher quadrupole moment of nitrogen as compared to oxygen and argon, the nitrogen gets adsorbed due to the non-uniform distribution of charge in the zeolite material. This would result in separating O_2 and Ar as the end products. Consequently, adsorption gas separation's oxygen purity limit is roughly 95%. Aluminosilicate microporous minerals known as zeolites are frequently utilized as commercial adsorbents and catalysts. Generally known as "atomic strainers", they essentially comprise silicon, aluminium and oxygen with the overall recipe $M_xAl_xSi_{1-x}O_2.yH_2O$, where M is the metal component, x lie between 0 and 1, and y is the number of water molecules [92]. It should be noted that zeolites also have a high propensity to adsorb other air components, such as H_2O and CO_2, so pre-activating the zeolite material and removing these components from the zeolite material is essential to extract an optimum performance during the adsorption process.

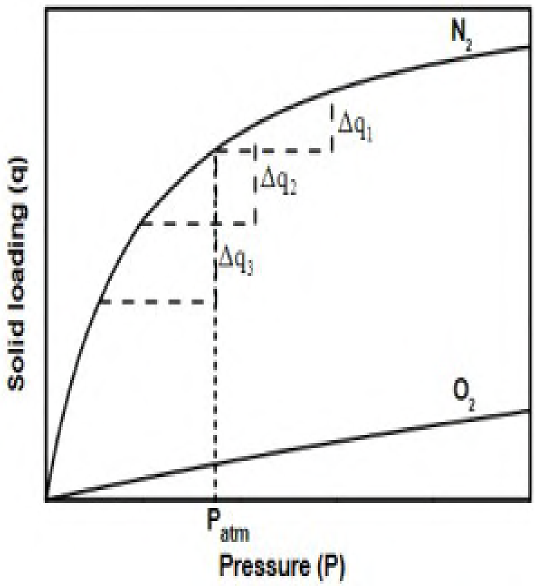

Fig. 1.3 N_2 and O_2 loading as functions of pressure [1]

The adsorption process is a strong function of the system's pressure and temperature, and one can perform a continuous process of O_2 separation utilizing cycling one of these parameters. Figure 2.4 shows the N_2 loading on zeolite as a function of pressure. Using the fact that N_2 adsorption varies significantly with pressure, one can cyclically change the latter to bring out a continuous supply of the desired output component, say oxygen. The process typically consists of two columns filled with zeolite material undergoing adsorption and desorption alternatively. At any time, one column would be under adsorption wherein it is pressurized to effectuate the adsorption of N_2 (Fig. 2.4) and separation of O_2 for further use. Simultaneously, the pressure in the other column is reduced to effectuate the desorption of N_2, which is thrown back into the atmosphere.

Based on the material used, say LiX or NaX, different pressure cycles can be classified as

(i) Pressure Swing Adsorption (PSA): The process is normally carried out in NaX zeolite material. The pressure swing happens between a high pressure of 6-7 bar and the atmospheric pressure.

(ii) Vacuum Swing Adsorption (PVSA, VSA or VPSA): This method is more relevant to the LiX zeolites. The pressure swing is performed between sub-atmospheric and super-atmospheric ($\approx$ 1 to 1.5 bar) pressures.

1.5 Common PSA systems


(a) (b)

Fig. 1.4 Adsorption based oxygen separation device (a) Portable oxygen concentrator (b) 100-1000 sLPM PSA plant

The commercial PSA systems typically come in two flavours: the personal use concentrators and large PSA plants. The various parameters of these devices have been compared in table 1.2. The portable oxygen concentrator device is primarily for personal use, and the maximum flow rate that can be expected from such devices is around 5-10 standard liters per minute (sLPM). The upstream pressure of the device is approximately 1 bar. Both the flow rate and the upstream pressure restrict the device's usability for severe COVID patients. Additionally, the device's cost is high compared to the number of patients it can sustain, thus

	Portable Oxygen Concentrator	**PSA plant**
Capacity	5-10 sLPM	100-1000 sLPM
Price (INR)	$\approx$ 1 lakhs	> 20 lakhs
Area occupied	Portable	> 100 sq.ft.
Upstream pressure	$\approx$ 1 Bar	$>$ 4 Bar

Table 1.2 Comparison of O_2 concentration devices

making the device impractical for hospital use involving multiple patients. The device's conciseness and portability sometimes come at the cost of its durability, particularly concerning moisture filtration and removal. On the other hand, PSA plants typically yield between 100 sLPM and 1000 sLPM with upstream pressure greater than 4 bar. The produced oxygen can be directly used in intensive care units (ICU) and sustain multiple COVID patients with mild and severe symptoms. The issues with these large PSA plants are their high setup cost and sizing (>100 sq. ft). Additionally, most of these plants require highly skilled labour to operate and maintain the correct functionality. All these factors restrict the widespread usage of the PSA plants in small/medium size hospitals, particularly in tier II/III towns and cities. Thus, the need of the hour is a ruggedised PSA system with a small footprint and the ability to serve small hospitals with medical-grade oxygen at pressures suitable for ICU/CCU scenarios.

1.6 Overview of the thesis

This thesis presents the progression of steps taken to develop a novel 40 sLPM mini-PSA plant in detail. The first part of the work deals with the experimental implementation of a device based on pressure swing adsorption (PSA) to obtain medical-grade oxygen at desired flow rates. The overall procedure has involved designing and testing multiple device versions of the device starting from tabletop models with LiX zeolite as the adsorbent. Parametric studies have been carried out on each of these versions by varying pressurisation, purge, and equalisation times, along with modifications to the adsorption column's length/diameter (l/d) ratio. Each version, having its pros and cons, helped in the ultimate evolution of the device that provides 92% enhanced oxygen stream at 40-45 liters per minute. Here, transient relevant data such as the pressure variation in the two cylinders, the output flow rate, and purity have been obtained for each experimental trial.

The second part of the work involves detailed numerical simulations that mimic the present PSA cycle. These simulations have been performed using Ansys Fluent package with the integration of adsorption kinetics via specialised User Defined Functions (UDFs). The complete numerical model has been thoroughly validated by simulating different breakthrough curves reported in the literature. A simplified axisymmetric configuration has been utilised to emulate the complete system's behaviour. The influences of different process timings and the system's geometry have been thoroughly analysed and compared with the obtained experimental data.

The current thesis describes all the above activities via five chapters, including the present introduction chapter. The second chapter gives a detailed review of the available literature relating to the PSA process for oxygen concentration. Particularly, critical reviews and comparisons of different PSA processes involved in oxygen concentration have been carried out. The third chapter discusses the different versions of the prototypes developed in the present work, with their pros and cons. Chapter 4 presents the basic numerical model involving the porous media flow and the adsorption kinetics. Systematic validations of the model with the published literature have also been discussed. Chapter 5 provides a summary and conclusions of the work, along with discussions on the scope for future extension.

Chapter 2

Literature Review

2.1 Introduction

The present chapter provides a detailed overview of the different aspects of Pressure Swing Adsorption (PSA) process and its implementation. The chapter begins by describing the fundamentals of cryogenic and non-cryogenic air separation processes. This is followed by a section on the fundamentals of adsorption in zeolite materials. Various advancements in the PSA technology, such as the decarbonisation of flue gas, filtration of novel gases, and development of the pressure equalisation step, etc., are discussed in the subsequent section, along with a summary of the patents related to mobile oxygen concentrators. Finally, we discuss the overall development and modifications carried out for oxygen concentration.

2.2 Oxygen separation techniques

The oxygen separation techniques can be categorised into cryogenic and non-cryogenic separation processes. The working principle of these processes is briefly discussed below.

2.2.1 Cryogenic Oxygen separation process

Figure 2.1 shows the schematic of a typical cryogenic air separation system. In this process, the constituent gases are separated by cooling the air until liquefication and selectively distilling the components at their respective boiling points. Typical cryogenic separation plants consist of a proper combination of heat exchangers and filtration columns to provide maximum efficiency. A conventional cryogenic oxygen plant constitutes three essential building blocks: a warm end container, a cold box, and storage.

In the first part, the air pressure is increased to 5-7 bar by compressing it using a screw-type or centrifugal compressor. Subsequently, the compressed air is cooled to 12°C by passing it through a refrigerant-based chiller. The next step uses an air purification unit to remove the residual water vapour and carbon dioxide in the gas mixture. Eliminating these components from the air stream is essential as they would otherwise freeze and clog the cold parts of the plant. The air purification unit consists of twin molecular sieve driers that alternatively separate the carbon dioxide and moisture from the process air.

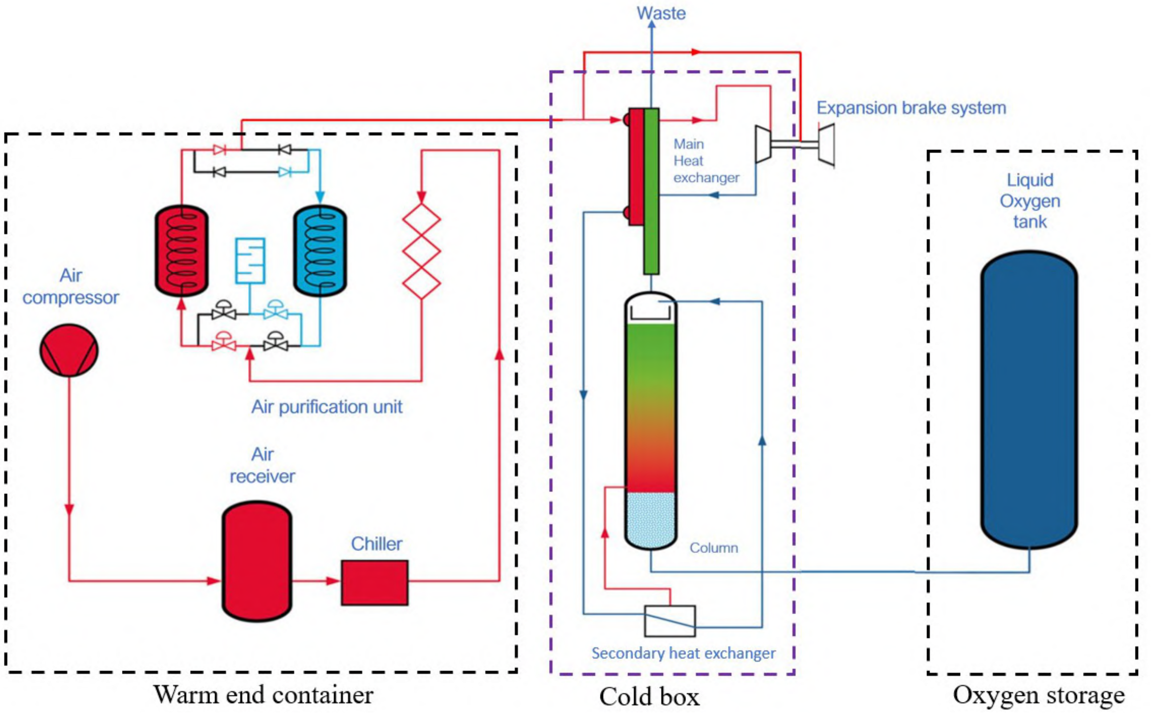

Fig. 2.1 Cryogenic separation of oxygen [31]

After the air is purified in the warm end container, it enters the cold box and reaches the main (primary) heat exchanger. Here, it is cooled by the counter-flowing waste gas stream that liquefies it partially. The gas then exits the main heat exchanger, nearly at -112°C. The complete liquefaction of air occurs in the secondary heat exchanger (boiler) through the evaporating of liquefied oxygen. The liquefied air enters the distillation column (top) through the purity control valve and descends through the packing material. The evaporated O_2 vapour from the secondary heat exchanger is also returned to the distillation column, where it rises and meets the descending processed liquid air. As the air descends further, it gradually gets rid of nitrogen and has a high concentration of oxygen; this is ultimately collected at the base as pure liquid O_2. A turbine that expands a high-pressure gas stream is used to provide refrigeration for the whole process in the cold box.

A cryogenic liquid pump is used to increase the pressure of the liquid O_2. This can be optionally vaporised in an evaporator to obtain gaseous oxygen for further usage.

2.3 Non-cryogenic separation process

As mentioned before, the cryogenic air separation process is energy intensive and is not economical at small scales. Thus, it is unsuitable for in-situ oxygen production. Hence, we now turn our focus to the non-cryogenic separation processes, which are classified as

1. Membrane-based air separation process
2. Pressure Swing Adsorption-based separation process
3. Chemical process for air separation

2.3.1 Membrane-based air separation process

The first process we discuss here is the gas separation by membranes, which is a pressure-driven process. Selectivity and permeability are the two major deciding criteria for determining the performance of a membrane. The penetrant's size also typically influences the choice of membrane and its permeability. It is found that the diffusion coefficient of large gas molecules is small. Thus the space within the permeable membrane must be large enough for the gaseous molecules to diffuse through. It should be noted that the diffusion coefficient is impacted by the flexibility of the polymer chain and the membrane material's free volume in the polymer[92]. In a binary separation scenario, the permeability ratio of two gases determines a membrane's selectivity.

Figure 2.2 shows the membrane's gas separation process[62]. This is a pressure driven process where the membrane is permeated by an additional gas, which exits as a low-pressure stream known as permeate. Retentate is often termed as the excess gas leaving as a high-pressure stream. Depending on the application and purity, the interest could be either retention or permeation.

The membrane is categorized as either porous or non-porous based on its porosity. The non-porous membranes have one polymer chain space induced by thermal vibration of 0.3 to 1 nm. In contrast, the pore sizes of porous polymer membranes range from 5 to 100 nm. The non-porous membranes are therefore commonly used for gas separation[62]. In general (fig 2.3), the gas separation performed using membrane is based on any one of the diffusion processes: 1) Knudsen diffusion, 2) molecular sieving, and 3) solution diffusion [62, 71], as shown in the figure below.

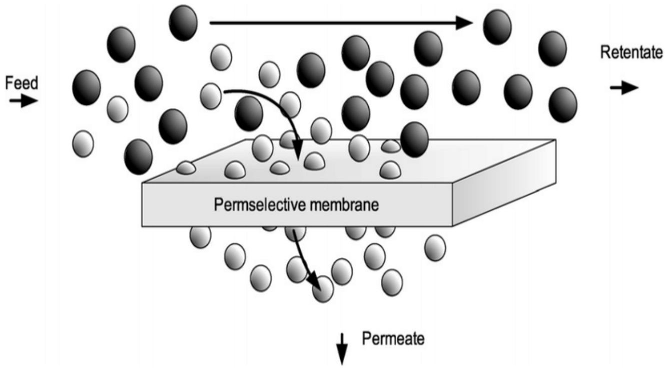

Fig. 2.2 Schematics of membrane separation [62]

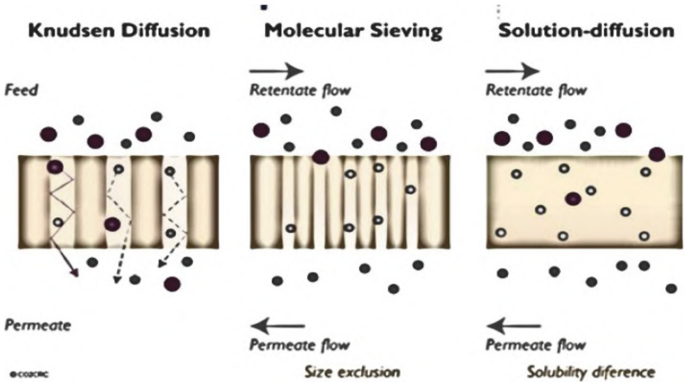

Fig. 2.3 Illustration of permeation of gases via membranes [71]

Knudsen diffusion occurs when two primary conditions are satisfied: 1) the pores in the membrane are smaller than 0.1μ, and 2) diameter of the pores is equal to the mean free path of the gas molecule[62]. Intuitively, the lower molecular gases tend to diffuse more quickly because of the small diameter compared to the heavier ones. The desired gas molecules strongly interact with the pore walls compared to the rest, which ultimately leads to its separation. High selectivity is possible when a component exhibits preferential adsorption. Molecular sieving aids in the separation of molecules of various sizes. Large molecules can't pass through the membranes' tiny pores, so they don't make it into the membranes. Darcy's law, which governs pressure-driven convective flow through capillaries, best describes the movement of the molecules in these situations. However, the solution diffusion process is a more general model for membrane separation.

The solution diffusion process is treated as a standardised separation method and is widely used in processes like- dialysis, reverse osmosis, separation of gases, pervaporation etc. [71]. The mass transfer is governed by the concentration gradient between the upstream and downstream phases of the membrane[62]. The diffusion of the solution is determined by the composition of the membrane and the molecules penetrating it. It should also be noted that across the membrane, the chemical potential is only expressed in terms of the concentration gradient, and the pressure is assumed to be constant for the solution-diffusion model. Differences in the membrane material's molecular interactions with permeating species cause differences in solubility. Different permeates are separated based on the differences in their amount of diffusion through the membranes.

2.3.2 Pressure Swing Adsorption (PSA)

Air containing different gas components can be filtrated into its significant components depending on the selective adsorption of gases on specific zeolite materials. For instance, sequestration of nitrogen over O_2 and Ar can result in oxygen separation on an adsorbent material. As the nitrogen molecules have a greater quadruple moment compared to oxygen and argon[89], it gets adsorbed in the zeolite framework,[92] mainly due to its random charge distribution. This would result in separating O_2 and Ar as the end products. Consequently, adsorption gas separation's oxygen purity limit is roughly 95%. Aluminosilicate microporous minerals, known as zeolites, are frequently utilized as commercial adsorbents and catalysts. Generally known as "atomic strainers", they essentially consist of silicon, aluminium and oxygen[92]. It should be noted that zeolites also have a high propensity to adsorb other air components, such as H_2O and CO_2, so pre-activating the zeolite material and getting rid of these components is necessary to get the best performance during nitrogen adsorption.

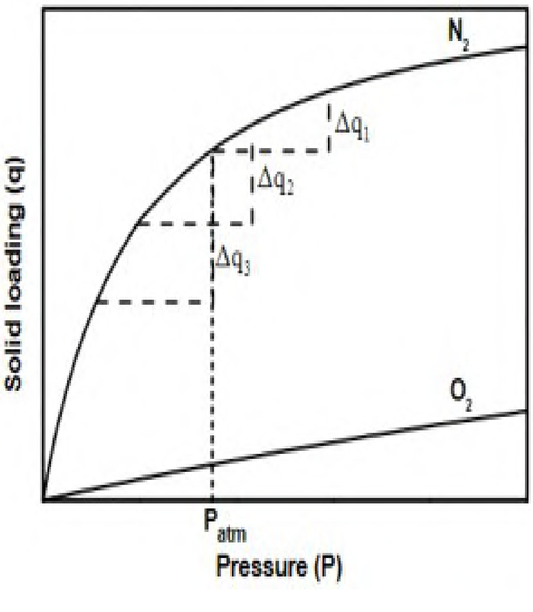

Fig. 2.4 N_2 and O_2 loading as a function of pressure [1]

The imposed pressure and temperature typically regulate the adsorption process, and one can perform a continuous process of O_2 separation by cycling one of these parameters. Figure 2.4 shows the N_2 loading on zeolite as a function of pressure. Using the fact that N_2 adsorption varies significantly with pressure, one can cyclically change the latter to bring out a continuous supply of the desired output component, say oxygen. The process typically consists of two columns filled with zeolite material undergoing adsorption and desorption alternatively. At any time, one column would be under adsorption wherein it is pressurized to effectuate the adsorption of N_2 (Fig. 2.4) and separation of O_2 for further use. Simultaneously, the pressure in the other column is decreased to regulate desorption of N_2, which is thrown back into the atmosphere.

Based on the material used and imposed parameter, say LiX or NaX, different pressure and temperature cycles can be classified as:

(i) Pressure Swing Adsorption: This process is mainly carried out in NaX and LiX zeolites where the system operates within the range of high pressure (6-7 bar) and normal atmospheric pressure.

(ii) Vacuum Swing Adsorption (PVSA, VSA or VPSA): This method is more relevant to the CaX zeolites [16]. The operating pressure range for nitrogen adsorption is 1.5-1.8 bar, whereas the nitrogen desorption step employs vacuum at 0.2-0.5 bar pressure.

(iii) Temperature Swing Adsorption (TSA): The adsorption of gas components on a zeolite is an exothermic reaction. Temperature swing adsorption is a periodic variation of the temperature for adsorption and desorption. The process is a vital function of temperature. When the temperature is low, adsorption of gases takes place, and the bed regeneration is done at higher temperatures [15].

The propensity of some natural and manufactured materials to preferentially adsorb either nitrogen or oxygen is the basis for adsorption process technology. This device may create nitrogen or oxygen by flowing compressed air through a tank containing adsorbent materials. Adsorbents are selected based on their adsorption properties. Certain adsorptive materials are utilised as molecular sieves, which can preferentially adsorb specific target gas species. Because the adsorbent bed requires periodic desorption, the adsorbent process is essentially a batch process. As a result, most manufacturing units using this technique incorporate at least two adsorbent vessels to ensure operational continuity. At any moment, one of the vessels produces a product by adsorbing undesirable air components, while the other vessel is regenerated by lowering it to atmospheric pressure[9]. A system of valves swiftly shifts the streams to another vessel as the adsorbing vessel approaches saturation. A surge vessel (buffer vessel) located downstream of the absorbers ensures that the product gas is delivered continuously.

Cycle Description

The fundamental Skastrom cycle (PSA) involves two columns tightly packed with the adsorbent material (zeolite, carbon molecular sieve, MOFs etc.) that selectively adsorb gas molecules. In an oxygen concentrator, the two components of the adsorption process are, “raffinate," which is enriched in oxygen and the other one is the "extract" product enriched in nitrogen. Feed air is allowed to pass through a packed bed of adsorbent wherein nitrogen gets adsorbed while issuing the raffinate (O_2) at the outlet.

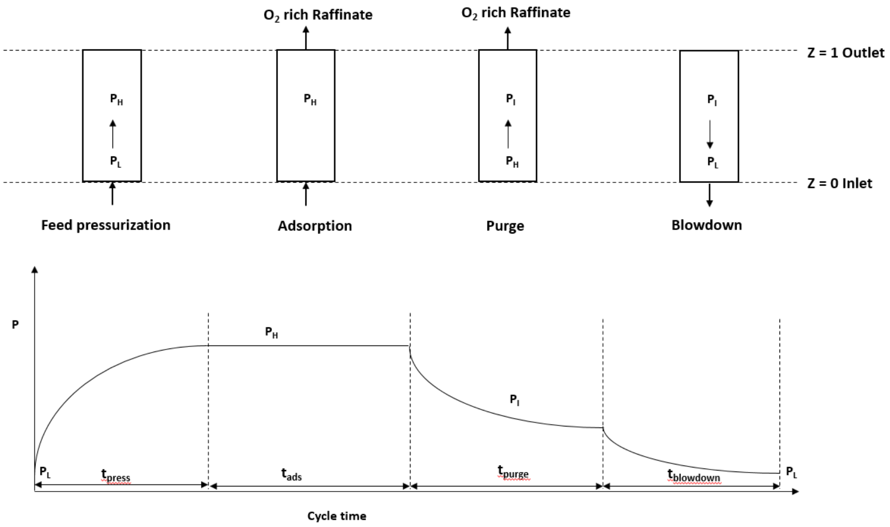

Fig. 2.5 A four-step PSA cycle

Typically, a four-step cycle is implemented in each column of the zeolite columns, as shown in Fig. 2.5[49].

- Feed pressurisation: A feed air containing 21% of O_2 and 79% of N_2 by volume is provided, at 6 bar pressure and 25°C temperature, at the inlet(Z=0) while other end (Z=1) was kept closed. The pressure in the column is increased to P_H [49].

- Adsorption at high pressure: Next, the outlet end of the column (Z=1) is opened while maintaining the column pressure at P_H with the continuous flow of feed air into the column[49].

- Purging: The inlet (Z=0) is kept closed. This step aims to flush out adsorbed nitrogen in the other zeolite column using high-purity oxygen. This is accomplished by keeping the outlet (Z=1) open and by allowing a portion of the O_2 rich raffinate to pass through the other columns[49].

- Blowdown step: When the outlet (Z=1) is kept closed, the trapped nitrogen is desorbed by decreasing the column pressure to P_L[49].

2.3.3 Chemical process for air separation

Electrolysis is an alternative method for separating oxygen or other gaseous mixtures. The procedure utilises porous catalytic electrodes oriented in opposite directions and separated by an electrolyte transport and barrier phase. The following reactions occur, and oxygen gas is selectively removed and transported to the anode[91].

$$O_2 \,+\, 2H_2O \,+\, 4e^- \,->\, 4OH^- \;\text{(at the cathode)} \tag{2.1}$$

$$4OH^- \,->\, O_2 \,+\, 2H_2O \,+\, 4e^-\text{(at the anode)} \tag{2.2}$$

where $4OH^-$ is transported through the electrolyte to the anode. An external voltage is applied to overcome the overvoltage loss in reactions, concentration, and ohmic polarization.

2.4 Fundamentals of adsorption

Since the present aim is to develop and model a novel PSA device, we now focus some more on the fundamentals of the adsorption process. Based on interaction forces, adsorption can be classified as

1. Physical or physisorption: It is due to the weak Vander Waals forces between the adsorbate and the adsorbent.
2. Chemical or chemisorption: It is due to solid chemical forces of bonding between the adsorbate and the adsorbent.

When a gas molecule's interaction potential energy ϕ equals the amount of work required to bring it to the adsorbed state, adsorption of a gas molecule on a solid surface occurs[92]. The total potential energy between the adsorbate (gas molecules) and the adsorbent (zeolite) is the sum of potential energies generated by the adsorbate-adsorbate and adsorbate-adsorbent interactions [92][77]. For physical adsorption, this is defined as

$$\phi = \phi_D + \phi_R + \phi_{Ind} + \phi_{F\mu} + \phi_{\dot{F}Q}[77] \tag{2.3}$$

where ϕ_D is dispersion energy, ϕ_R is the close-range repulsive energy, ϕ_{Ind} is induction energy (interaction between the induced dipole and the electric field), $\phi_{F\mu}$ is the interaction between electric field (F) and permanent dipole, and $\phi_{\dot{F}Q}$ is the interaction between field gradient $\dot{F}$ and the quadrupole moment Q. The first two terms, "ϕ_D+ϕ_R", are non-specific (Barrer 1980 [77]) and non-electrostatic. The last three terms are contributions from the charges on the solid surface.

A quadrupole can be modelled as two dipoles [92] as shown in figure 2.6. A force acting on each dipole is proportional to the local gradient. Since the forces and subsequent torques on the quadrupole will cancel each other, the quadrupole will not result in a symmetric field, unlike a dipole. The charge on the nucleus of a molecule, like nitrogen's quadrupolar nuclei, can be distributed symmetrically or asymmetrically. If the charge dissemination is symmetric, the interaction of the nuclei with the electric field gradient is direction-independent. In the case of an asymmetric charge distribution, the electric field gradient may then exert a torque on the nucleus due to its interaction with the nucleus. A quadrupole moment will be observed in these nuclei, referred to as quadrupolar nuclei.

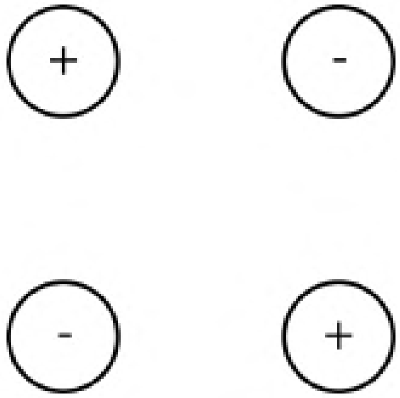

Fig. 2.6 A 2D quadrupole moment representation

The permanent dipoles and quadrupoles can significantly influence the total energy of the zeolite material. Nitrogen lacks a permanent dipole, despite having a moderately strong quadrupole; Consequently, $\phi_{F\mu}$ is zero. In terms of applications for air separation, N_2 and O_2 are particularly interesting. Nitrogen is more preferentially adsorbed by zeolite than oxygen because of its higher quadrupole moment (nearly four times)[92].

The zeolite's physical structure, adsorption mechanism and adsorption kinetics are discussed in the following sections.

2.4.1 Zeolite adsorbents for PSA process

As described earlier, zeolite adsorbents are used for the separation and purification of gases. Basically, zeolite is microporous in nature that enhances adsorption by providing greater surface area. It also provides some mobility to adsorbate molecules within the adsorbent[92]. Because of their distinct structure and composition, adsorbents can interact with various kinds of molecules differently. Any adsorption process must use the appropriate adsorbent to achieve the desired separation. Type A, Type X, or Type Y[83] are the three types of synthetically produced zeolites that are available commercially. Zeolites are composed of microporous, crystalline aluminosilicate with the chemical formula,

$$M_x[Al_xSi_{1-x}O_2].yH_2O, \tag{2.4}$$

where y is the number of water molecules, M is the metal ion, and x has values between 0 and 1.

Due to their unique crystalline structure, zeolites are often differentiated from other adsorbents. This structure enables them to function as efficient molecular sieves. It provides proper pore size for the adsorption of gas molecules too[92]. The zeolites are characterized in light of the pore size according to IUPAC [90]:

1. Micropores: <2 nm
2. Mesopores: 2-50 nm
3. Macropores: >50nm

The specific molecular characteristics of the zeolite, such as the size of the pores, its shape, its polarity, etc., govern the adsorption and desorption processes within a zeolite[90]. Zeolites are composed of the oxides of silicon and aluminium, having a tetrahedral arrangement with oxygen bridges[92]. The zeolite structure is constructed from a number of smaller secondary units. The elementary building blocks of secondary units shown in Fig. 2.7. The

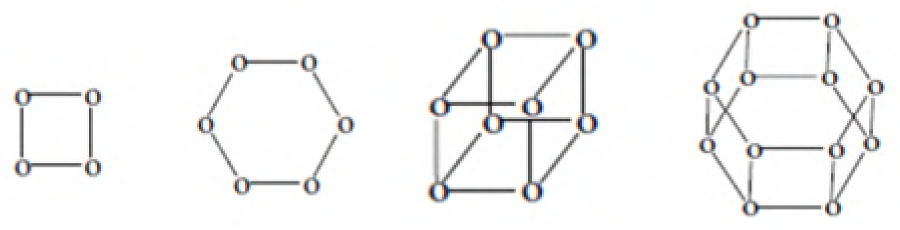

Fig. 2.7 Basic secondary structures of zeolite[23]

secondary structures make up the different zeolites- Types A, X, and Y[92]. Additionally, these secondary structural units create a porous crystalline structure.

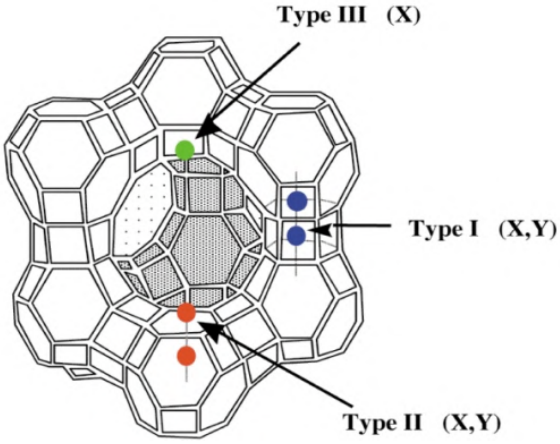

Fig. 2.8 Structure of zeolite [67]

There is a considerable range of Si/Al ratios in zeolite, ranging from one to infinity, as silicon and aluminium atoms can be interchanged, albeit with difficulty. The structure experiences a net negative charge when an aluminium atom is added, which necessitates using an exchangeable cation to maintain electroneutrality, i.e., lowering the Si/Al ratio. The structure will collapse as a result. However, it should be noted that for specific purposes, Si/Al ratio and the exchangeable cation type can be altered in a zeolite[92]. The hydrophobic nature of a substance with a higher Si/Al ratio makes it more effective at removing organics from water. Zeolites are majorly classified as per the ratio of Si to Al: between 1.5 and 3 for Type Y and between 1 to 1.5 for Type X [92][89]. A higher capacity to attract polar molecules like water is provided by a lower Si/Al ratio. Na^+, Li^+, and $Ca2+$ are some of the common exchangeable cations. Apart from this, cations also determine the pore size and other zeolite properties [92]. As depicted in Fig. 2.8, there are three exchangeable ion location sites within the zeolite structure: Types I, II, and III. Among these three, Type I are the most accessible sites and, thus, they get filled first. Type II are the last to get filled since they are the most inaccessible[92].

2.4.2 Zeolite adsorption

Due to their unique surface chemistry, zeolites have many unique adsorption properties. Firstly, the oxygen atoms mainly form the framework's surface, while Si and Al are hidden behind the oxygen atom's tetrahedra. Adsorbate molecules cannot easily access them because they are not entirely exposed. Secondly, anionic oxygen atoms are more prevalent and polarizable than Al and Si cations. Thus, the anionic oxygen atoms dominate the van der Waals interactions with the sorbate molecules [92]. In addition to this, anionic oxygen cations are present at various locations, some of which the adsorbate molecules cannot access. However, some additional cations can be found above the oxygen surface. To reduce the system's free energy, the cations disperse themselves. The heat treatment temperature, cationic species, and hydration level influence the distribution of these cationic sites. The total potential for interactions between adsorbate molecules with permanent dipoles and quadrupoles is frequently dominated by interactions with these exposed cations.

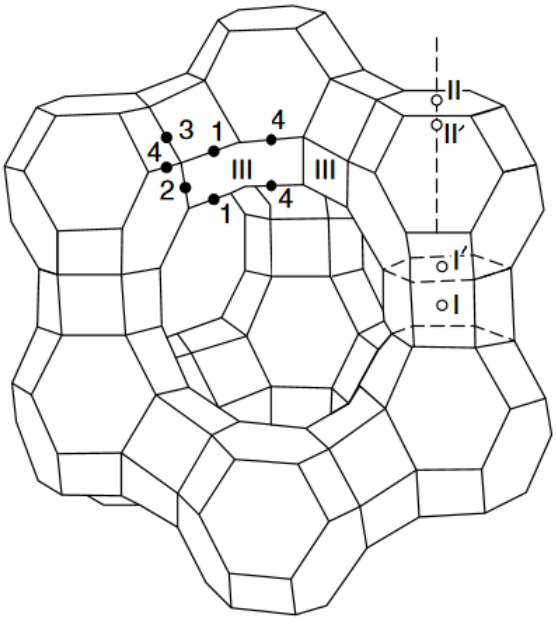

Fig. 2.9 Cationic sites of X type zeolite [92]

The cations sites in X-type zeolite have been schematically represented in Fig. 2.9. Sites I, I', and II' are inaccessible to adsorbate molecules because they are not exposed. Cations obtained from alkaline earth metals (Ca^+) mostly occupy site II, whereas the cations of alkali metals Li^+, Na^+ etc. occupy both the sites[92].

For N_2/O_2 adsorption on X-type zeolite, the effect of cationic sites is crucial. There are 196 cation sites in X-type zeolite, but only 96 cations use them. It should be noted that all compounds try to attain the lowest energy state in their stable formation. So, when the zeolite is heated or activated to 350°C, the cations migrate to the areas with the lowest energy to maintain their structural stability. Migration is an activated process that is affected by the cation's size, time, and temperature. Unfortunately, the super cage cavity cannot see the most stable sites with the lowest energies. These are the sites with the greatest coordination number.

Molecule or Ion	$-\phi_{total}$ (KJ/mol)
O_2-Li^+	32
O_2-Na^+	20
N_2-Li^+	51
N_2-Na^+	36

Table 2.1 The energies of interaction (ϕ) between molecules and cations that are isolated [92]

N_2 reacts more with Li^+ as compared to Na^+ due to the higher charge density of Li^+ ion and higher $\phi_{\dot{F}Q}$ (electric field gradient - quadrupole) potential. Due to the higher charge density of Li^+, it polarises the nitrogen molecule, which results in a significantly higher quadrupole moment compared to oxygen. The total interaction energy is shown in Table 2.1 [92]. O_2 and N_2 are non-polar molecules; however, these molecules develop a quadrupole moment in the zeolite structure's induced field gradient of cations. The difference in the quadrupole results in a significant difference when the same ion interacts with O_2 and N_2.

2.5 Advancement in PSA process

We now focus on literature essentially concerning the advancement of the PSA process for sequestration, modification in the Skarstrom cycle and the recent developments in the PSA process for oxygen concentration.

Over the years, there has been significant work conducted to develop and modify the PSA process for the separation of different gaseous components, including- hydrogen purification ([18], [75], [57], [79], [51], [50]), air separation process ([27], [13], [44], [42], [72]), novel gas purification using PSA process ([26], [81]) and CO_2 capture ([80], [58], [17], [49]). As discussed earlier, the advantage of using the PSA process emanates from its low energy consumption and capital requirement. As a result, the PSA process is extensively used for separating the gas components when required. Much work has been carried forward to advance and optimize the PSA plants. In several years, many patents have been filed to develop the PSA process. A few of them are mentioned below.

Kratz and Sircar [48] received a patent for a medical oxygen concentrator that used a PSA cycle to deliver high-purity medical oxygen to patients at home. They used two molecular sieve layers as adsorbents within a single bed where the base layer made of 13X or 5A zeolite removed moisture and CO_2 while the second layer (calcium and sulfur) adsorbed the N_2[48]. Their medical oxygen concentrator could supply more than 90% purity oxygen.

Using PSA technology and Lithium exchanged zeolite, Dubois *et al.* [30] developed a portable oxygen concentrator for producing 50%-95% of oxygen from air. The device along with an air compression device was having a total weight of less than 10 kg. They suggested combining technical advantages such as faster cycle timing, small Li^+ zeolite particles, and allowing the patient to select the product oxygen flow rate to create a mobile oxygen concentrator.

Based on the PVSA method, Occhialini *et al.* [64] patented a weight-optimized portable oxygen concentrator that used two weight-characterized compressors to separate the pressurized feed air from the product flow. In a five-bed procedure, they stacked the adsorption beds in order to eliminate moisture, CO_2, and N_2 from the surrounding air. The first layer was filled with activated alumina, and the second layer was filled with LSX zeolite. They suggested a few optimizations: 1) the process parameters determine the oxygen concentrator's weight; 2) the device should have a minimum pressure and product flow rate throughout the process cycle. They concluded that the oxygen concentrator used in the above method could provide 93% pure oxygen.

A dual-mode medical oxygen concentrator for portable air separation, including a rechargeable power supply for driving a motor, was developed and patented by Whitley *et al.*[86]. The device supported patients with the pulmonary disease by producing an excellent flow rate. It was portable and operated independently. Finally, they concluded the output of the portable unit was 0.5 to 3 sLPM, whereas the stationary unit's output was higher than the portable one by 2 SLPM.

Atlas *et al.* [14] patented a PSA concentrator with its adsorber filled with Oxysiv and OxysivMDX adsorbents. They claimed that the oxygen concentrator weighed 10 lb overall, had 800 in^3 volume, and had an 8-hour battery life and a maximum rate of pure oxygen provided at 0.9 SLPM.

Using the Vapour Swing Adsorption technique with LiLSX zeolite, Jagger *et al.* [41] developed a PSA system with less than 10 lb essentially for personal medical use. For a flow rate of 5 sLPM, their device gave a recovery rate of 60% and in the pulsed mode generation, it gave an oxygen purity of 85–95% range.

It is to be noted that the advancements in PSA technology have not only focussed on developing new devices, but also on the modifying the Skarstrom cycle. Many works have attempted to introduce additional steps, such as pressure equalization, pressurization, and purge. ESSO research groups developed the pressure equalization step ([13], [27]) where they closed all the valves and allowed the adsorbent cylinder to equalize the pressure between two cylinders. This was extended for the multiple adsorbent cylinders; the more the number of cylinders, more will be the pressure equalization steps ([87], [88]). The pressure equalization step not only helps improve the recovery rate but also helps in saving mechanical power.

Other development in the Skarstrom cycle involves the use of a vacuum in the system. As we discussed earlier, the adsorption/desorption is a function of the pressure ratio, i.e., maximum and minimum pressure. Several studies related to the Vacuum swing adsorption process(VSA) have been put forward for different purposes such as comparison of zeolite performance and optimization of the plant ([37], [52], [94], [42], [46], [39]). Several studies have also been performed in the field of developing a mathematical tools along with an experimental setup. A few of them are reported in the next section.

2.5.1 Recent developments in the modelling of PSA process for oxygen concentration

Modelling of PSA process for oxygen concentration and other sequestration processes has made it possible to identify several issues related to the adsorption cycles, help enhance/develop new designs of machinery, etc. The recent developments in the numerical modelling of oxygen concentrators have helped us understand the gap in research. These new models predict the dynamic behaviour of adsorption process along with the variation of process (pressure, temperature) parameters that significantly affect the device's performance.

Papai *et al.* [66] developed a numerical model to investigate the sequestration process of nitrogen and oxygen in the zeolite. They stated that the adsorption is a vital function of isolated charge of Na^+ and Li^+ cations which led to the adsorption of N_2 and O_2 separation process.

In a case study, Kayser and Knaebel found that with the use of 13X zeolite, the designed PSA cycle for air separation was affected by isotherm non-linearity in an equilibrium-based model[47]. As the adsorption and desorption pressures depart from the linear portion of the isotherm, the model exhibits a decrease in oxygen recovery. Doong and Yang [29] developed an equilibrium simulation model using performance curves to compare the various PSA cycles. Rege and Yang [69] later simulated air sequestration to compare the adsorption properties of LiX and Nax zeolite. They observed a higher propensity for the air sequestration process in LiX, which provides higher efficiency, higher recovery rate, and low bed size factor (BSF) than the NaX-based process, at a pressure ratio of two. Later, Chou and Huang performed a numerical simulation for a four-bed complex process using the zeolite 5A to 1) first verify the experimental results from Chiang*et al.*[22] and to illustrate four-bed PSA modelling, 2) and for different production rates, the existence of optimum purge rates[24]. They classified their findings into two parts, 1) in the absence of breakthrough, the alternative bed, which undergoes depressurization in the pressure equalization step, gives a relatively higher recovery with an oxygen purity of 95%, 2) in the presence of breakthrough curves, they observed a unique purge rate for maximum recovery and varied purge rate to obtain maximum purity. They concluded that dispersion in the PSA column results in a decrease in oxygen purity and recovery at high pressure rising rate and also demonstrated that during the adsorption step, the pressure rate directly affected the cycle's performance[59]. Shin *et al.* [73] investigated the effect of the equalization step in the PSA cycle, and they compared complete and incomplete pressure equalization (PE) steps for air separation using 13X zeolite.

Webley and He [85] performed a finite volume analysis for PSA/VSA with second-order accuracy to handle the different types of boundary conditions involved in the process. They compared the linear isotherm models with their analytical solution, which showed a good agreement. Later, Béchaud *et al.* [10] performed a hydrodynamic stability analysis of a gas mixture in porous media for a PSA process. In this regard, they developed a numerical solution to investigate the effects of concentration and pressure perturbations. They concluded that the instability occurs at a higher perturbation amplitude at the inlet, requiring a higher amplitude of pressure and concentration to stabilize the adsorption/dispersion process.

Jee *et al.* [43] performed an analysis based on the three-bed PVSA process that exceeded 94% purity during oxygen concentration by using two adsorbents; 10X zeolite and one carbon molecular sieve. With this configuration, they could achieve >94% purity at 2 sLPM. Additionally, they successfully predicted the cyclic behaviour using a non-isothermal dynamic model. Lu *et al.* [53] studied a dual-bed pressure vacuum swing adsorption system to adjust the parameters and address the imbalances in the differential pressure profiles. Soo *et al.* [78] revisited the experimental observation of [5] and [63] to observe the effect of D_{disp} (axial dispersion) on fast altered cycle. They observed numerical difficulties in implementing Alpay's experiment conditions, whereas Murray's conditions were consistent even for the plug flow. They concluded that with the increase in D_{disp}, there is a 10-point decrease in oxygen purity.

Ahari *et al.* [2] developed a general dynamic model for both N_2 PSA and O_2 PSA consistent with the experiments. Product purity was investigated with respect to changes in cycle time, inlet feed velocity, and bed length. They concluded that the product purity improves with an increase in bed length or blowdown step duration and decreases with an increase in cycle time and inlet velocity. Later, Todd and Webley [82] contrasted the results of the linear driving force (LDF) and rigorous pellet models for sequestration with a packed bed of LiLSX adsorbent using a fast cycle PSA plant. They highlighted the accurate working of both models when they validated their experimental findings for longer cycle duration without diffusion kinetics. However, the LDF model slightly under-predicted their experimental results compared to their rigorous pellet model because of the overestimation of inter-pellant mass transfer and relatively short cycle duration. The work also revealed no significant effect on process performance from the inter-pellet pressure drop.

The modelling and parametric studies of oxygen concentration using 5A zeolite for a two-bed pressure swing adsorption were studied by Beeyami *et al.* [11] using the finite difference method. They arrived at the ideal parameter values of operation, i.e. the optimum pressure of adsorption, cycle length, feed rate, and production rates were found to be 2.5 atm, 150 seconds, 15 cm^3/s, and 2.55 cm^3/s, respectively, wherein 95.45% oxygen purity and 77.3% recovery was attained. Additionally, they discovered that a longer tubular structure is beneficial for using units with an L/D ratio of 10.5 or above. The decrease in pressure throughout the bed was found to be insignificant.

Chai *et al.* [19] developed a medical-use fast cycle pressure swing adsorption using LiX zeolite. They investigated the effects of various factors, like adsorbent size, pressure, and step duration, on the performance of the PSA process for oxygen concentration. To achieve a specific bed size factor (BSF), oxygen purity and recovery, they used an adsorbent of diameter 0.35mm. They discovered that 230 g of adsorbent was essential to produce 5 sLPM of the mixture at 90 per cent O_2 purity. They showed that reducing the processes' cycle times could not permanently reduce the BSF. Additionally, they proposed a medical oxygen concentrator that could be used for personal medical purposes and was lightweight, quick-attached, and highly portable.

Rao *et al.* [68] developed a novel device based on fast PSA technology for medical oxygen concentrators using lithium LSX as the separation adsorbent for a continuous flow rate of 1-3 sLPM at 90%. They studied the BSF and oxygen recovery with changing cycle time, adsorber pressure and temperature profiles. They reported the inability to reduce the BSF by decreasing the cycle time. Alternatively, the presence of argon in the feed air increased the BSF and reduced the recovery rate. They further concluded that the optimum parameters of the device for a cycle time of 5-6s are BSF = 45.34 kgs/$TPDO_2$ and R = 27%.

Hamed [36] developed an oxygen concentration PSA device with two adsorbent columns along with the four-step operation. The development of the PSA process was studied using 5A zeolite to determine the effect of adsorption pressure on the device's performance. They concluded that the maximum optimized performance obtained is 76% at 4 bar pressure.

Ferreira *et al.* [32] modelled a single-stage PVSA adsorption process for obtaining high-purity oxygen from air using AgLiLSX zeolite. They created a device with two AgLiLSX zeolite-filled adsorption beds operated on a seven-step cycle at room temperature between 0.2 and 1.6 bar. The device provided 0.1 sLPM of oxygen at 99+% . The unit was optimized using the response surface methodology (RSM), and the optimal parameters for the best performance of the device were reported.

Hossein *et al.* [40] used the Silver exchanged adsorbent to obtain the high-purity oxygen. It was reported that due to the similar adsorption properties of argon and oxygen, it was challenging to get high-purity oxygen. To overcome the restriction, they developed a mathematical model by measuring the adsorption isotherm of N_2, O_2 and Ar, and they tried to validate their experimental results using the finite volume technique. They concluded that the feed containing O_2 and Ar 95% and 5 %, respectively, can achieve an oxygen purity of 99% with a recovery of 11.35%.

The selectivity of the adsorbent is an essential factor in deciding the product recovery. Shokroo *et al.* [74] performed a comparative study to investigate the 5A and 13X zeolite performances and reported as to how various parameters such as pressure ratio (P_H/P_L), adsorption step time, and cycle time affect the oxygen purity and recovery. The larger mass transfer zone in 5A zeolite reduces the adsorption propensity of nitrogen as compared to 13X zeolite. They concluded that to obtain oxygen purity of 96%, the pressure ratio should be in the range of 5.5 to 7 and a cycle time of 75 to 90.

Pan *et al.* [65] developed a medical oxygen concentrator with a deep evacuation step which provides an oxygen purity of 90% using Li^+ zeolite. Later, they developed a numerical model in COMSOL to effectively study the pressurization/depressurization of the nano-porous zeolite using pressure vacuum swing adsorption. They further compared their numerical results with their experimental data, found a good agreement with each other, and observed the effect of velocity and concentration profile for further optimization of the device.

Moran and Talu [61] highlighted the limitation of portable PSA concentrators for oxygen generation. They pointed out the need for more experimental evidence relating to the use of minimum BSF for cycle timing. To address the issue, they performed an experiment based on two columns PSA process to measure the minimum BSF and product purity. They concluded that increasing the pressure ratio lowers the BSF, causing an insignificant effect on the cycle time. However, they stated that the macropore diffusional resistance was a significant cause for minimum BSF [61].

The 1D cyclic adsorption process of air with oxygen purity of $\sim$90% at 2 sLPM was studied numerically by Akulinin *et al.* [3] using a double-adsorber PSA unit. They concluded that, on average, the compressor outlet pressure has a $\sim$57 per cent impact on the extraction degree and $\sim$12 vol. per cent on the oxygen concentration.

Makarem *et al.* [55] studied the pressure vacuum swing adsorption experimentally and theoretically. They reported that the device's performance increases with the difference between adsorption and blowdown pressure. They also developed a numerical algorithm using the finite difference and different quadrature methods (DQM) to validate their experimental data.

Yang *et al.* [93] gave a radial-flow absorber model for the PSA process regarding oxygen generation within a range of 2.67-5.83 sLPM flow rates. They investigated the gas distribution, mal-distribution factors, and pressure difference for different types of radial absorbers. They reported an increase in the oxygen flow by 2.19 times and a decrease in the purity by a factor of 18.6% when the flow rate was increased from 2.67 sLPM to 5.83 sLPM.

However, it is observed that the PSA process is susceptible to changes in the atmospheric air. To address this issue, Akulinin *et al.* [4] tried to develop a mathematical model solution for optimization issues in the PSA units using 13X zeolite. They accounted for the uncertainty in the atmospheric air according to the criteria for oxygen recovery.

Mahdi *et al.* [54] investigated the effectiveness of the simultaneous oxygen recovery and nitrogen from the air separation process. They devised a way to pressurize the second unit using the nitrogen-rich, depressurized gas from the first. They showed how the flow conditions, such as adsorption pressure and time, affected the device's performance.

To enhance the mass transfer during the adsorption/desorption, Chang *et al.* [21] tried to replace the traditional single-cylinder adsorbent with semi-circular cylinders, constituting both adsorption/desorption. They proposed this idea to justify the space utilization and increase of mass transfer zone by connecting the two semi-cylindrical adsorbent columns. To move forward, they used 5A zeolite to analyze the behaviour and dynamics of the adsorbent cylinder numerically. They observed the influence of the flow (pressurization, production time, feed pressure diameter of the adsorbent column, and length) and heat transfer parameters (adiabatic conditions) on the adsorption/desorption of gas components.

Arora *et al.* [8] designed a single-bed medical oxygen concentrator to increase the device flexibility for patient use and optimized the device using numerical simulation for PSA and PVSA. They performed a detailed investigation on Lithium X zeolite adsorbents and concluded that LiLSX performed comparatively better than 5A and LiX with an oxygen concentration of 90% at 21.7sLPM for the PSA plant and 93-95.7% pure oxygen at 1-15 sLPM for the PVSA plant[8].

Zhu *et al.* [96] developed a PVSA for oxygen production where they studied the device's performance by focusing on parameters like- time of adsorption/desorption, pressurization/purge and temperature. They obtained a maximum oxygen purity of 90% in their configuration.

2.6 Overview of literature

The literature study reveals that various experiments have been conducted to deal with the development and modifications of PSA process for the separation of different gaseous components. Specifically, significant effort has been dedicated towards improving and optimizing devices operating on the traditional Skarstrom cycle that includes the implementation of the equalization step, which substantially increases the overall performance and saves power consumption. There have also been significant works in the commercial sector with regard to the development and modelling of medical oxygen concentrator as well as large-scale PSA plants for oxygen concentration. However, there is an evident gap in the literature regarding medium-scale devices and their design approach. Most of the work had been performed mainly based on the fact that the device gives a maximum oxygen purity of more than 90% at 5-10 sLPM. Unfortunately, the published numerical modelling data on PSA plants does not help significantly in this regard, as they are often limited to 1D calculations or specific design/material combinations. Additionally, if we want to increase the device's overall performance while keeping the device's portability in mind, the same thing was missing in the literature. Further, there is a gap in the development of 2D or 3D models that accurately predict the PSA plants complete behaviour. In view of these facts, the objectives of the current work are formulated and are mentioned in the following section.

2.7 Objective of the current work

The major objectives of our current work are as follows:

- Designing, developing, and optimizing a novel mini PSA plant that is portable and provides at least 40 liters of oxygen per minute to support a minimum of 6 to 8 patients in a small hospital scenario.
- The device should come in a rugged form with medical-grade components and handle both lithium-based and sodium-based zeolites.
- To perform detailed numerical simulations for understanding intrinsic operation of the device and provide further scope for optimization.
- These high-fidelity simulations will have to model the adsorption process in the porous zeolite columns accurately.

Chapter 3

Experimental setup descriptions and Results

3.1 Introduction

In the current chapter, we deal with the experimental aspects of the present work. To begin with, various details, including information on the PSA cycles, designs of different initial setups built, etc., are briefly described. The final configuration of the setup obtained after overcoming all the limitations of the earlier designs is then discussed in detail. The results obtained from the systematic experimentation on the final design are also discussed.

3.2 Device overview

As mentioned in the previous chapter, the aim of the present work is to develop a mini pressure swing adsorption (PSA) plant capable of delivering oxygen mixture with a purity greater than 90% at flow rates larger than 40 standard liters per minute (sLPM). In order to achieve this objective, the PSA configurations developed here use two zeolite columns with a number of solenoid valves, a flow meter, pressure regulators, and a flow controller. These combinations essentially help obtain a cyclic control of the process necessary for the PSA plant. Here, the cycle can be broadly divided into three parts: pressurisation, purging, and equalisation. We have built six designs in total, wherein pressure equalization was not implemented until the last design. The different variable parameters of the system are the three step-timings (t_{pres}, t_{pur}, t_{eq}), delivery flow rate, inlet pressure (on the compressor side), the geometry of the zeolite tank and the type of zeolite used. With all these parameters set for a given configuration, the interest is to measure the oxygen purity at the outlet. Correspondingly, a systematic trial was performed to understand the capabilities and limitations of all the six designs considered here. It is important to note that lithium X (LiX) zeolite was used for the first two designs, whereas sodium X (NaX) zeolite was utilised for subsequent setups. We now proceed to discuss the details of all six experimental designs in the following section.

3.3 Initial PSA cycle

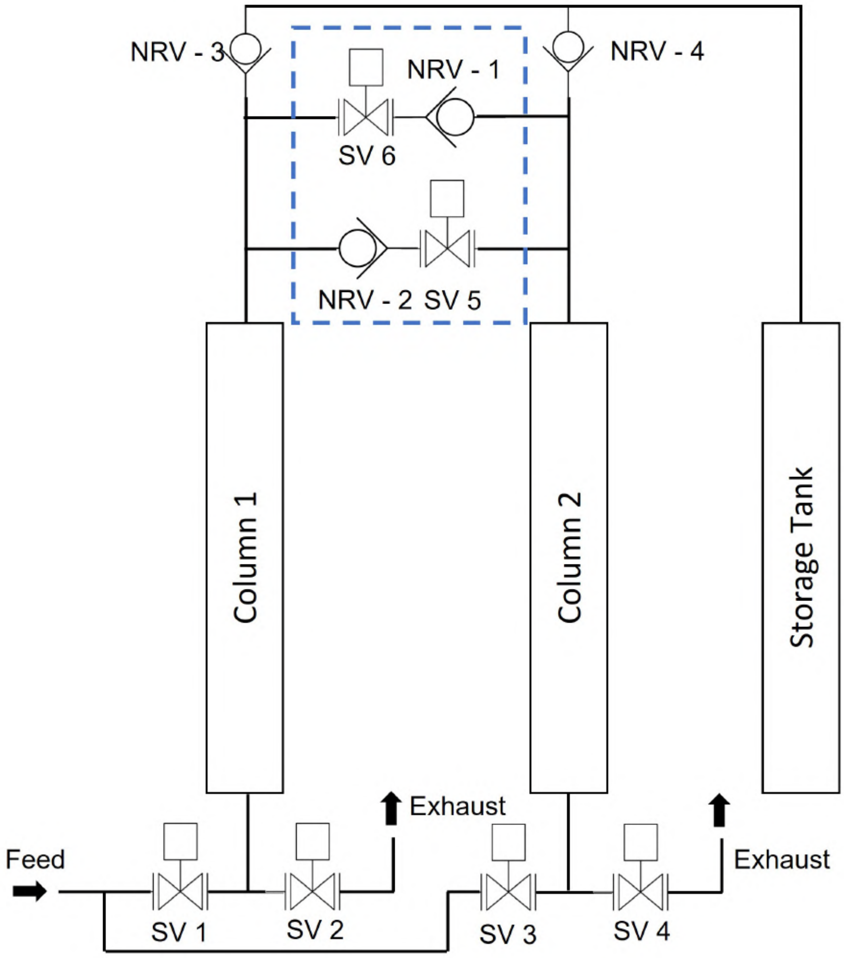

Fig. 3.1 Initial PSA cycle

To begin with, we now discuss the PSA cycle that was implemented for the first five designs developed in the current work. These devices are the typical two-column systems controlled by a set of six 2/2 solenoid valves (SV1, SV2, SV3, SV4, SV5, SV6) and four non-return valves (NRV-1, NRV-2, NRV-3, NRV-4). The 2/2 valves are under normally-closed (NC) condition and they open when energised. As the name suggests, the NRVs allow the

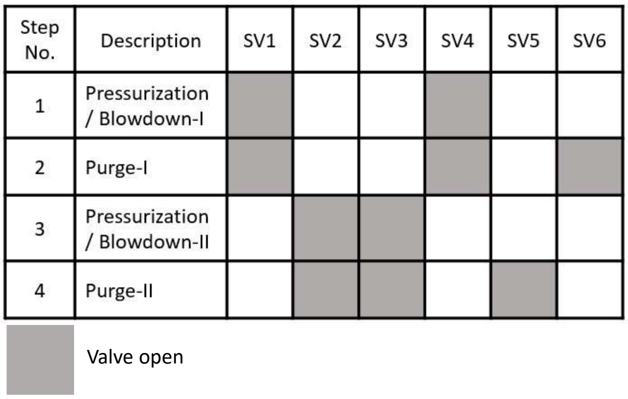

Step No.	Description	SV1	SV2	SV3	SV4	SV5	SV6
1	Pressurization / Blowdown-I	▨			▨		
2	Purge-I	▨			▨		▨
3	Pressurization / Blowdown-II		▨	▨			
4	Purge-II		▨	▨		▨	

▨ Valve open

Fig. 3.2 Valve configuration

flow only in one direction. The schematic of the initial PSA cycle is shown in Fig. 3.1. The cycle essentially uses four steps; one pressurisation and one purging step corresponding to each of the columns present. The sequence of valve opening is represented in Fig. 3.2, and the different steps involved are as follows:

- Pressurization - 1: Feed air, at high pressure, is supplied to Column-1, and the oxygen-rich gas is obtained at the top of the column and is issued to the temporary storage tank shown at the right (Fig. 3.1). Precisely, valve SV1 is energised, and the non-return valve NRV-3 allows the outflow of high-purity oxygen. Valves SV5 and SV6 are kept closed. During this step, Column-2 simultaneously undergoes blow-down, i.e., valve SV4 is opened. This allows for the reduction of pressure in the column and the removal of desorbed nitrogen from the zeolite material.

- Purge - 1: In this purge step, along with SV1 and SV4, valve SV6 is kept open, and all the other valves are kept closed. The objective here is to purge Column-2 with an enriched stream of oxygen. This process replenishes Column-2 by removing de-adsorbed nitrogen from the zeolites and preparing the column for pressurization.

- Pressurization - 2: This step is the opposite of the first. Column-1 undergoes blow-down since valve SV2 is opened to regenerate the adsorbed nitrogen. Meanwhile, Column-2 undergoes pressurization since SV3 is kept open, and all the other valves will be closed.

- Purge - 2: Here, Column-1 is purged while Column-2 nears its saturation with respect to adsorption. In this step, the valves SV2, SV3, and SV5 are opened, and NRV-4 delivers oxygen-rich gas at the top of the second column.

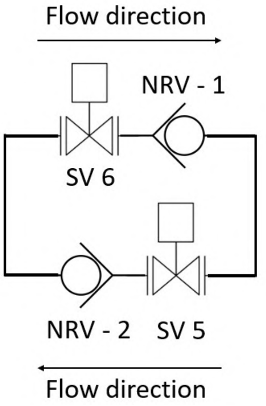

Fig. 3.3 Purging mechanism

The above steps provide a continuous supply of high-purity oxygen. Note that all the solenoid valves used here are essentially unidirectional; hence, there will be a leakage flow even in their “OFF” state when the delivery side of the valve is pressurised. To avoid such leakage, we use NRV-1 and NRV-2 in conjunction with SV6 and SV5. The combination is connected in parallel and is shown separately in Fig. 3.3. During the pressurization steps, when one of the tanks is at higher pressure, the presence of the NRVs prevents the leakage flow in both SV6 and SV5. However, during the ‘Purge - 1’ step wherein the valve SV6 is opened, NRV-1 allows fluid flow from the left to right, and NRV-2 blocks the leakage flow through SV5. Similarly, during the ‘Purge -2’ step, the NRV-2 allows the purge flow through SV5 from right to left and NRV-1 blocks the leakage through SV6.

With the above description of the overall configuration and the process steps, we move towards describing the different versions of the setup, their features, their limitations, etc.

3.4 Different PSA Designs

3.4.1 Design-1

The first design attempted as a part of the present effort is shown in Fig. 3.4. Different parameters of the setup are listed in Table 3.1. Here, the zeolite columns were made of stainless steel filled with zeolite particles (0.4mm to 1.6mm diameter). All the interconnections were done using 8mm pneumatic push-fit fittings. Two desiccant columns were used to separate moisture from the feed air: the first column was packed with activated alumina, whereas the second column contained activated silica. The orifice diameter of the solenoid valve used is 2.1mm. Lithium-based zeolite was used, and its mass in each column was approximately 320gm. The output purity obtained from this setup for different input parameters is listed in

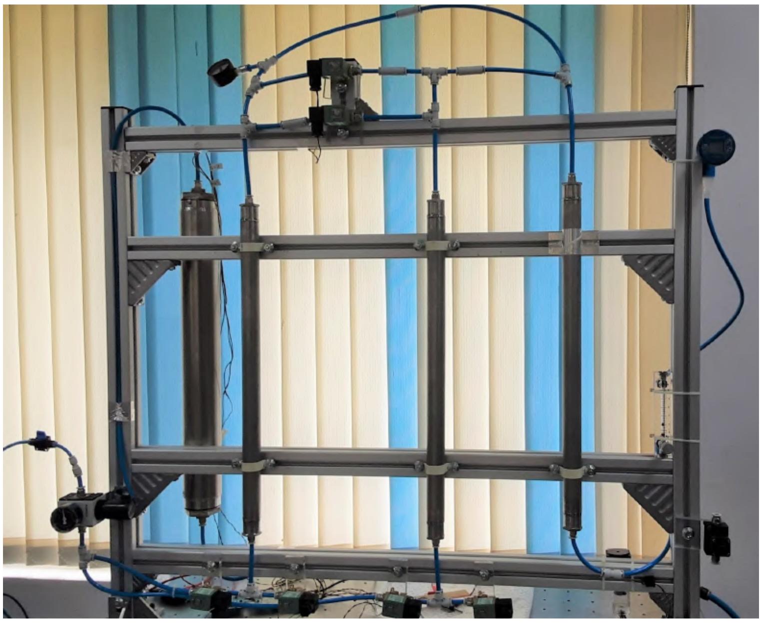

Fig. 3.4 Design-1

Column length	56.7 cm
Column diameter	2.7 cm
Type of zeolite	LiX
Mass of Zeolite in each column	320 gm
L/d ratio	21
Operating pressure	4 bar
Max flow rate	1 LPM
O_2 concentration	90.3%
Desiccant column type	Activated alumina and silica
Compressor power	2HP

Table 3.1 Features of Design-1.

Table. 3.2. While the influence of these parameters would be discussed later, it would suffice at this stage to note that the maximum flow rate at which the desired oxygen purity of $> 90\%$ was obtained is around 1 SLPM. Note that the l/d ratio for this design is around 21.

Trial No	Set Pressure (bar)	Output flow rate (LPM)	t_{press}	t_{pur}	Max pressure (bar)	Min pressure (bar)	O2 conc (%)
1	4	1	3	0.8	2.4	0	90.1
2	4	1.5	3	0.8	2.3	0	89.5
3	4	3	2.5	1	2.2	0	83.6
4	3	3	3	1	2.3	0	81.2
5	4	3	3	1	2.4	0	83.1
6	4	3	3	0.8	2.3	0	84
7	3	3	3.5	1	2.5	0	83.7
8	4	3	3.5	1	2.6	0	82.9
9	4	3	4	1	2.9	0	81.5

Table 3.2 Experimental data for design 1.

3.4.2 Design-2

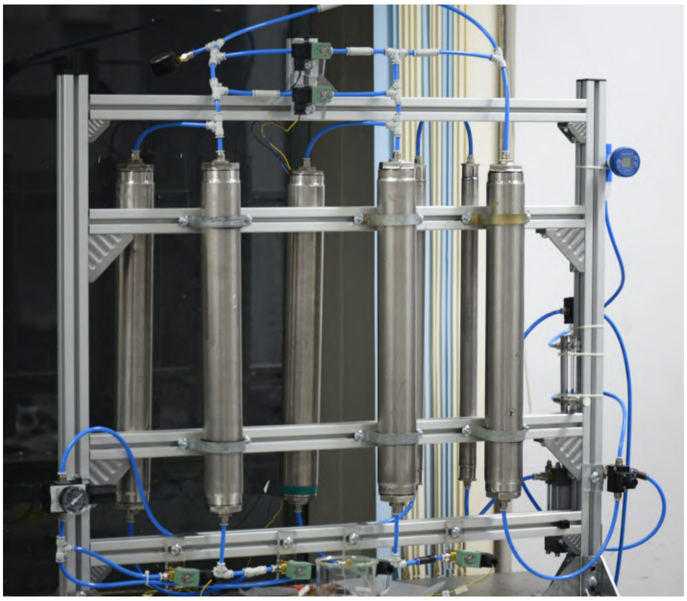

Fig. 3.5 Setup-2

To obtain a better output, the mass of zeolite utilised was increased by four times in the second design. Note that adsorption is a surface phenomenon and thus, increasing the mass of adsorbents should proportionally increase the number of nitrogen adsorption sites. Here, the total mass of zeolite used in each column was 1260 g. In this Design-2 (Fig 3.5), all the valve configurations were similar to Design-1. The pertinent design parameters of this setup have been listed in Table 3.3. Once again, the desiccant columns were packed with activated alumina and silica to remove moisture from the feed air. The device was operated using two 2 HP compressors connected in parallel mode. Table 3.4 shows the output purity obtained for different input parameters. Evidently, the device could deliver oxygen at 90.3% purity for a maximum flow rate of 10 SLPM. This improvement was over and above the factor of increase in the zeolite mass, which was close to four times. One notable factor that helped achieve this improved performance was the reduction of the l/d ratio from 21 in design 1 to 8.46 presently. As the next step, we tried to reduce this l/d ratio further in Design-3 and moved towards using NaX zeolites.

Column Length	56.7 cm
Column Diameter	6.7 cm
Type of Zeolite	LiX
Mass of Zeolite in each column	1259 gm
L/d ratio	8.46
Operating pressure	4 bar
Max Flow rate	10 LPM
O_2 Concentration	90.3%
Desiccant column type	Activated alumina and silica
Compressor	2x2HP

Table 3.3 Features of Design 2.

Trial No	Set Pressure (bar))	output flow rate (sLPM)	t_{press}	t_{pur}	Max pressure (bar)	Min pressure (bar	O2 conc (%)
1	4	5	5	2	3.5	1.4	85.6
2	4	5	8	2	3.7	1	93
3	4	5	10	2	3.8	0.7	94.6
4	4	8	10	2	3.8	0.7	71.5
5	4	8	10	1	3.8	0.7	58
6	4	8	10	3	3.8	0.7	74.9
7	4	8	12	2	3.8	0.5	73
8	4	8	12	3	3.8	0.7	75.3
9	4	8	12	4	3.5	0.3	76.6
10	4	8	12	5	3.6	0.2	69.4
11	5	8	12	4	4.7	0.5	81.2
12	5	8	12	3	4.7	0.5	87.2
13	4	8	14	5	3.8	0	70
14	4	8	14	4	3.8	0	77.6
15	5	8	14	4	4.9	0.3	81.3
16	5	8	14	3	4.8	0.4	86.8
17	5	8	16	4	4.9	0.2	80.5
18	5	8.26	12	3	4.7	0.5	94
19	4	10	13	3	3.8	0.4	90.3

Table 3.4 Experimental data for Design 2.

3.4.3 Design-3

In the interest of further scaling up the device, the mass of zeolite was again increased by a factor of four in the new design. However, this design used NaX zeolite as opposed to LiX zeolite, which was used in the previous two designs. Here, the intention was to make the device more economical, as LiX zeolites are expensive and have limited availability. The configuration of this new device is shown in Fig. 3.6, and the corresponding design parameters have been provided in Table 3.5. The zeolite columns were 4-inch pipes (schedule-5) with welded flanges at both ends. The flange covers with a central 1/4" hole were tightly screwed onto the flanges with the help of appropriate O-rings to prevent any leakage. Here, the desiccant columns were replaced by a 5 CFM PSA-based dehumidifier, which provided air at a dew point of -40°C under standard operating conditions. A 5/2 solenoid valve of 6mm orifice diameter replaced the four 2/2 solenoid valves at the lower part of the schematic. It replicated all the actions of the four valves without impacting the cyclic PSA process. Two 2HP compressors connected in parallel mode supplied the pressurized feed air. Table 3.6

Fig. 3.6 Design-3

Column Length	76 cm
Column Diameter	10.8 cm
Type of Zeolite	NaX
Mass of Zeolite in each column	4000 gm
L/d ratio	7.03
Operating pressure	4 bar
Max Flow rate	15 LPM
O_2 Concentration	91.5±0.2 %
Desiccant column type	5 CFM dryspell dehumidifier
Compressor	2x2HP

Table 3.5 Features of Design 3.

shows the output purity obtained for the different input parameters. It can be observed that the device was able to issue oxygen with 91.5% purity at a flow rate of 15 SLPM. While this was the right step toward achieving the desired scale-up, issues were observed in the design primarily due to the ejection of powdery substance during the blow-down step. Powder formation essentially occurred due to the fluidization of particles within the zeolite columns which led to particle-particle interaction and attrition. Unfortunately, these two processes reinforce each other. Particle attrition typically increases the void space in the column, which could, in turn, lead to increased space for particle fluidization and the resultant attrition. Thus, the continuous attrition of zeolite material inside the column eventually reduces the device's efficiency and leads to other performance issues. In this regard, a spring compression mechanism was utilised in the next design, as discussed below.

Trial No	Set Pressure (bar)	Output flow rate (sLPM)	t_{press}	t_{pur}	Max pressure (bar)	Min pressure (bar)	O2 conc (%)
1	4	15	25	6	4	0	91.5± 0.2
2	4	23.6	25	6	3.9	0	77.75± 0.85
3	4	23.6	20	6	3.7	0	80±0.5
4	6	23.6	30	6	5	0	75±1.5
5	5	23.6	20	6	3.9	0	79±1
6	6	23.6	20	6	6	0	81.8± 0.7

Table 3.6 Experimental data for Design 3.

3.4.4 Design-4

The primary intention behind Design-4 was to increase the flow rate from 15 sLPM to 30 sLPM without the perils of powder formation. Hence, the mass of the zeolite in each cylinder was increased to 12 kg. The zeolite column was manufactured using high-density PVC material and had a diameter and length of 20cm and 45cm, respectively, giving a l/d ratio of 2.25. Design-4 is shown in Fig. 3.8, and the corresponding system parameters are listed in Table. 3.7. In order to address the issue of powder formation, a spring compression mechanism was implemented both at the top and at the bottom of the zeolite columns to keep the zeolite particles in position and prevent fluidization during the pressurization and blow-down steps. Here, the tanks were filled with zeolite particles and electro-fused to prevent gas leakage.

The PSA steps followed here were similar to that of the previous designs. However, all the valves and the push-fit connectors were modified to have a larger orifice diameter of 12mm to accommodate the higher flow rate. A 5HP compressor was used to maintain the set pressure of 7 bar. Despite these changes, the device's performance was sluggish, and the yield at 30 sLPM was only 62% pure (Table 3.8). This behaviour is an unfortunate consequence of two design flaws. This first one is the very low value of l/d ratio, and the second is the large void volume (without zeolite particles) in the tank which was close to

Fig. 3.7 Setup 4

22.2% of the total volume. In fact, the latter issue is of particular concern as the void volume allows for nitrogen localization, which, on mixing with oxygen-enriched output, decreases the device's output efficiency. This is illustrated in Fig. **??** and the issue was particularly addressed in the next design of the device.

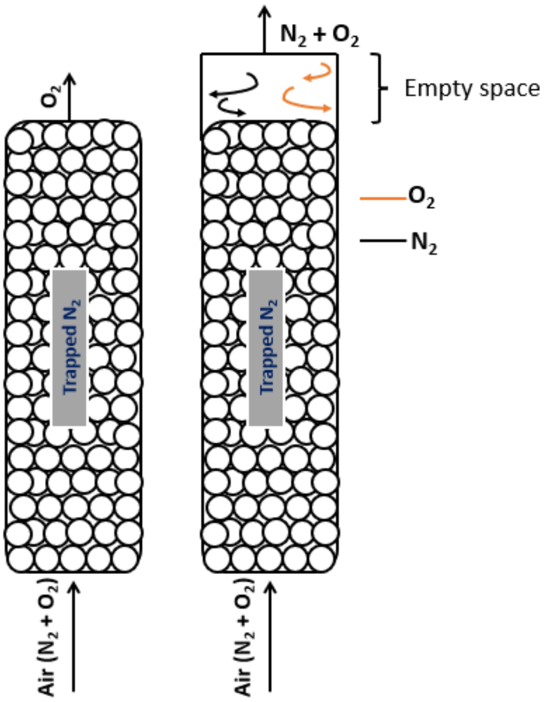

Fig. 3.8 Mixing of O_2 and N_2 due larger dead volume

Column Length	45 cm
Column Diameter	20 cm
Type of Zeolite	NaX
Mass of Zeolite in each column	6000 gm
L/d ratio	2.25
Max Flow rate	30 LPM
Operating Pressure	7 bar
O_2 Concentration	62 ± 1 %
Dead Volume	22.2%
Desiccant column type	10 CFM dryspell dehumidifier
Compressor	1x5HP

Table 3.7 Features of Design 4.

Trial No	Set Pressure (bar)	Output flow rate (sLPM)	t_{press}	t_{pur}	Max pressure (bar)	Min pressure (bar)	O2 conc (%)
1	7	30.7	25	15	6.6	0	34±1.5
2	7	31.21	15	4	4.4	0.2	56±1.5
3	7	31.21	20	4	5.8	0	61±1.1
4	7	31.21	25	4	6.7	0	62±1
5	7	31.21	30	4	6.8	0	59.5±1
6	7	31.21	25	8	6.8	0	59±4
7	7	31.21	25	2	6.6	0	53.5 ±0.5

Table 3.8 Experimental data for Design 4.

3.4.5 Design 5

Fig. 3.9 Setup 5

(a) (b)

Fig. 3.10 Spring compression mechanism

Unfortunately, the process of electro-fusion made the previous PVC design inflexible for alterations. Thus, the zeolite columns were reverted to the stainless steel pipe and flange configuration, as considered in Design-3. In the new design, as shown in Fig. 3.9, the diameter and length of the column were 21.8cm (6" schedule 5 pipes) and 70 cm, respectively. The mass of zeolite in each column was approximately 14 kg. All the components were connected with 12 mm pneumatic tubes with 1/2" BSP connectors. The 5/2 6mm dia solenoid valve was replaced with four 2/2 12mm diameter solenoid valves. In order to reduce the void volume, a spring compression mechanism, as shown in Fig. 3.10, was attached to the flange cover at the top. Four springs formed the connection between the flange cover and a perforated plate (with mesh) which acted as the piston that held the zeolite particles in position. This new configuration eventually allowed us to reduce the void volume from 22.2% in Design-4 to 2.15% in Design-5.

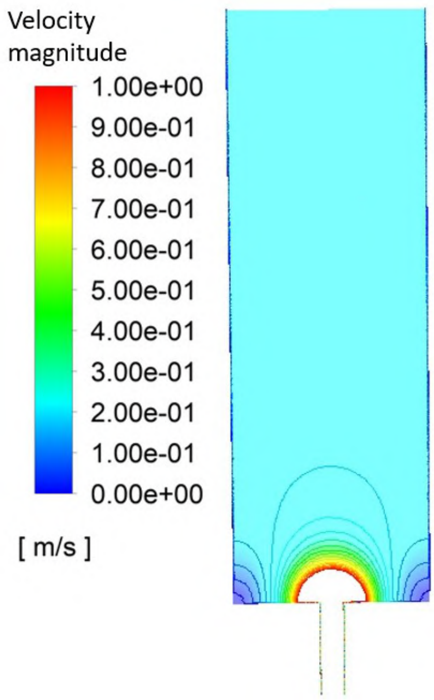

Fig. 3.11 Flow distribution inside the adsorbent cylinder in design 5

Column Length	70 cm
Column Diameter	21.8 cm
Type of Zeolite	NaX
Mass of Zeolite in each column	14000 gm
L/d ratio	3.21
operating pressure	7 bar
Max Flow rate	30 LPM
O_2 Concentration	90.3±0.5 %
Dead Volume	2.15%
Desiccant column type	2x10 CFM dryspell dehumidifier
Compressor	1x5HP, 2x2HP

Table 3.9 Features of Design 5.

Trial No	Set Pressure (bar)	Set flow rate (LPM)	t_{press}	t_{pur}	Maximum pressure (bar)	Minimum pressure (bar)	O2 conc (%)
1	8	29.9	15	4	3.3	0.4	89.5 ±0.3
2	8	29.9	20	4	5	0.9	90.3 ±0.5
3	8	29.9	20	4	4.5	0.2	83.5
4	8	32.8	25	4	5.3	0.1	86.8 ±0.3
5	8	34.5	25	4	5.2	0.2	86.7 ±0.3

Table 3.10 Experimental data for Design 5.

With the increased sizing of the columns, as mentioned above, a proportional increase of the inlet feed was also essential to achieve a proper scale-up of the device. Correspondingly, the device was fed by a combination of 5HP and 2HP compressors. A 20 CFM desiccant-based dehumidifier was used to remove moisture from the feed air. Note that the mass of zeolite in each column here was more than three times the quantity utilised in Design-3. Despite this increase in zeolite mass and the appropriate choice of compressor and dehumidifier, the device produced only 90.3% pure mixture at 30 sLPM. The reason for this poor behaviour is the sub-optimal l/d ratio of the zeolite column, which is 3.21. In order to investigate the sub-optimality further, a simple numerical simulation was carried out to understand the flow distribution within the column. While the numerical model and the simulation details are provided in the ensuing chapter, it would suffice at this stage to look at the velocity magnitude contour shown in Fig. 3.11. It is evident that the flow is mal-distributed at the inlet, leading to a local re-circulation zone at the corner of the cylinder. Such behavior is essentially due to this design's poor l/d ratio. In order to overcome this issue and achieve the desired scale-up, a new design with a dish-end at the bottom was considered subsequently. Alongside, an equalization step was introduced in between the purge and pressurization steps so as to obtain better recovery from the device. We now proceed to discuss this modified PSA cycle in the following section.

3.5 Modified PSA cycle

With the valuable information obtained from the different versions of the device built till now, a novel implementation of the PSA cycle was evolved. The essential idea was to implement

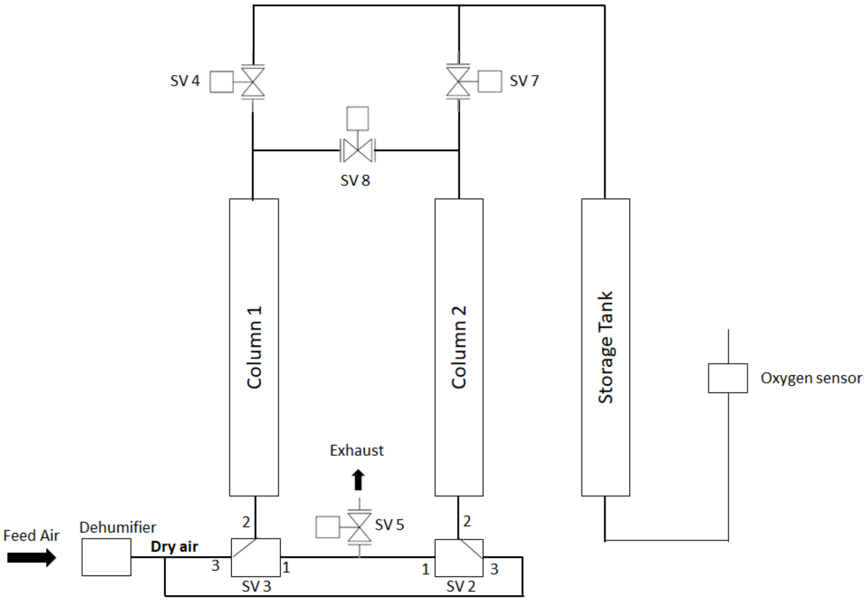

Fig. 3.12 Cycle Description

a pressure equalisation step that would improve the recovery percentage of oxygen from the device by eliminating wastage of the high-pressure air. It was also intended to eliminate all the NRVs in the design as they came with a penalty of pressure drop. The schematic of this modified cycle is shown in Fig. 3.12. The valve opening sequence is represented in Fig. 3.13. The system consists of two zeolite columns, two 3/2 solenoid valves (SV2 and SV3), and four 2/2 solenoid valves. The 3/2 valve will connect ports 1 and 2 by default, and when energised, ports 2 and 3 will be connected. The 2/2 valve will be under normally closed condition and will open if power is supplied. The sequence of operation is as follows:

- Pressurization - 1: Like before, the feed air, at high-pressure, is supplied to Column-1, and the oxygen-rich gas is obtained at the top of the column and is moved to the temporary storage tank (Fig. 3.12). Precisely, valve SV3 (port 2-3) is energised, and valve SV4 is kept open to deliver high-purity oxygen. Valves SV7 and SV8 are kept closed. During this step, Column-2 simultaneously undergoes blow-down, i.e., valve SV2 is de-energised (turned off), and valve SV5 is opened. This allows for the reduction of pressure in the column and the removal of de-adsorbed nitrogen from the zeolite material.
- Purge - 1: In this purge step for Column-2, valves SV5, SV3 (ports 2-3), SV4, and SV8 are kept open, and the other valves are kept closed. Opening SV8 allows for the purging of Column-2 with enriched oxygen mixture. This process replenishes

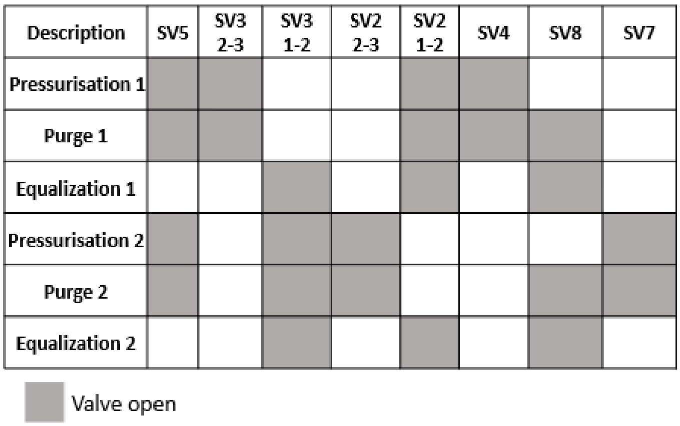

Description	SV5	SV3 2-3	SV3 1-2	SV2 2-3	SV2 1-2	SV4	SV8	SV7
Pressurisation 1	▨	▨			▨	▨		
Purge 1	▨	▨			▨	▨	▨	
Equalization 1			▨		▨		▨	
Pressurisation 2	▨		▨	▨				▨
Purge 2	▨		▨	▨			▨	▨
Equalization 2			▨		▨		▨	

▨ Valve open

Fig. 3.13 Valve configuration

Column-2 by further flushing out the de-adsorbed nitrogen from the zeolites and thus, preparing the column for pressurization.

- Equalization - 1: In the third step, i.e., the pressure equalisation (PE) step, all valves are kept closed except SV8. Valves SV3 and SV2 are held in port 1-2 configuration. There is no input of feed air to the system; also, no oxygen extraction occurs from the zeolite columns. The pressurised output in the buffer tank compensates for this intermittency. The main objective of the step is to equalise the pressure between the two zeolite columns and save on the feed supplied to the system. Basically, at the end of the Purge - 1 step, the adsorption process would be close to saturation in Column-1, and the residual mixture can be reused instead of being thrown back into the atmosphere.

- Pressurization - 2: This is the opposite of the first step. Column-1 undergoes blowdown as the column pressure is lowered desorption of nitrogen. Meanwhile, Column-2 undergoes the pressurization step. Valves SV5, SV3 (port 1-2), SV2 (port 2-3), and SV7 are opened, and all the other valves are kept closed.

- Purge - 2: Here, Column-1 is purged while the Column-2 nears its saturation with respect to adsorption. In this step, the valves SV5, SV3(port 1-2), SV2(port 2-3), and SV8 are opened to purge Column-1, and SV7 is still kept open to deliver the oxygen-rich gas at the top of the second column.

- Equalization - 2: This is precisely the same as the third step. No feed is provided-in, or no extract is taken out from the zeolite columns. The pressure is equalised between Column-1 and Column-2.

The above steps help provide more or less a continuous supply of high-purity oxygen. Small intermittency in flow happens during the equalization step. But as mentioned above, the momentary flow loss is compensated by the presence of the temporary storage tank. We now delve into the final experimental design that essentially incorporates the modified cycle described above.

Fig. 3.14 Design-6

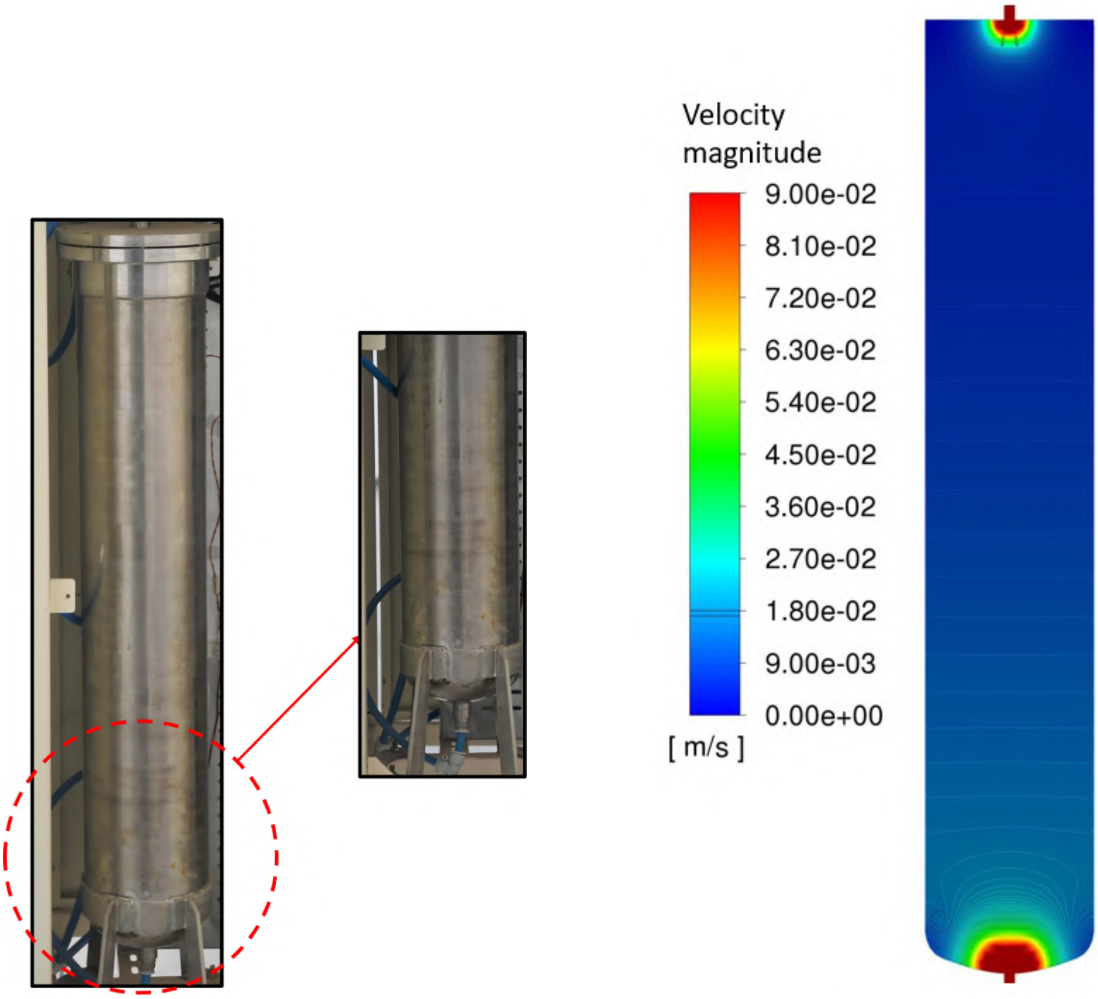

(a) (b)

Fig. 3.15 Modification of zeolite cylinder in design 6 (a) Modification of cylinder in design 6 (b) Flow distribution inside the cylinder in design 6

Column Length	93 cm
Column Diameter	16.3 cm
Type of Zeolite	NaX
Mass of Zeolite in each column	12900 gm
L/d ratio	5.7
Flow rate	45 LPM
O_2 Concentration	90.5±0.7 %
Dead Volume	0.16%
Desiccant column type	20 CFM dryspell dehumidifier
Compressor	1x5HP

Table 3.11 Features of Design 6

3.6 Final experimental setup

Figure 3.14 shows the final experimental setup that could deliver the desired output of 92% O_2 purity at 45 sLPM. The two zeolite columns are not visible in the picture as they are located behind the perforated plate where all the valves and regulators have been mounted. The effective length and diameter of the columns are 93cm and 16.83cm, respectively, corresponding to an L/d ratio of 5.53. The total mass of zeolite in each column is approximately 12.9kg. The bottom of both the columns was welded with a 2:1 ellipsoidal dish-end (Fig. 3.15) to address the issue of flow mal-distribution. Figure 3.15(b) shows the flow distribution inside the cylinder obtained via numerical simulations. It is evident that the local re-circulation zone observed at the corner of the cylinder for Design-5 is now absent (fig 3.11).

Here, a 20-mm thick flange cover was used at the top of the zeolite columns wherein a spring mechanism along with a perforated plate, as shown in Fig. 3.10, was utilised to keep the zeolite particles under compression. The springs for this purpose were chosen appropriately, as there is an optimum valve desired for the spring stiffness. While stiffer springs would significantly prevent particle movement/fluidisation that may lead to their attrition and powder formation, they also might allow for a larger void volume. In this design, the springs were chosen so that the void volume was around 0.16% of the total volume. Note that the void volume should be as minimum as possible, as it can provide space for nitrogen localization and thus result in a significant reduction of oxygen purity at the outlet.

Here, most of the pneumatic tubes were replaced by 12mm diameter stainless tubes, and all the push-fit connectors were replaced by stainless steel half-inch NPT threaded ferrule connectors to provide better sturdiness to the system. All the solenoid valves were replaced by 12mm diameter bi-directional solenoid valves specially designed for oxygen generation. These valves do not allow for leakage flow even when there is a pressure of 8 bar on their delivery side. The overall system was normally run by a 5HP oil-free air compressor capable of delivering air (Free Air Delivery) at a flow rate of $\approx$ 17 cfm. When required, an additional 2HP compressor was operated in parallel. In order to avoid contamination of zeolites with moisture, a special desiccant-based air dryer capable of delivering air at 20 cfm with -40 °C Pressure Dew Point (PDP) was utilised. The feed flow from the air dryer was controlled by a pressure regulator and was fed into the system via the two 3/2 solenoid valves, SV2 and SV3. The values SV4, SV5, SV7, and SV8 were bi-directional 2/2 valve. All the solenoid valves were oxygen rated. The overall valve operations were performed as described above. The outlet oxygen flow from the device was controlled via a small pressure controller. The measurement of flow rate was carried using a Honeywell air flow sensor (AWM700 series) which could scale up to 300 sLPM. Pressure in the individual zeolite cylinders was measured using a Honeywell pressure transducer (PX2CG1XX010BACHX series with pressure ranging from 15psi to 1000 psi), and a Honeywell oxygen sensor (OOM202 series) was used to measure the oxygen purity.

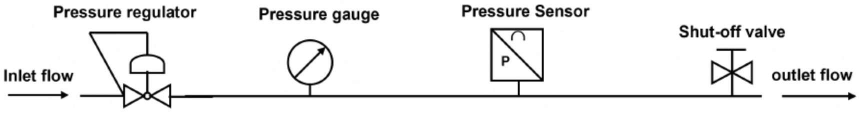

Fig. 3.16 Pressure sensor calibration schematic

The pressure sensor was calibrated using a setup as shown in Fig. 3.16. A single network wherein a pressure regulator, pressure gauge, pressure sensor, and shut-off valve were connected in series. The pressure inside the line was regulated using a pressure regulator and the pressure sensor, whose output in milli-volts was measured against a calibrated gauge. A systematic trial was performed for different pressure ranging from 0.5 bar to 8 bar. The pressure vs. voltage curve is shown in Fig. 3.17(a), and we curve fit to obtain the linear relationship between pressure and voltage (mV).

Similarly, the oxygen sensor, whose output was obtained as milli-volts, was calibrated against the Envitec Oxiquant S oxygen analyser. The linear calibration curve thus obtained is shown in Fig. 3.17(b). Finally, the flow sensor was calibrated against a rota-meter, connected in series. The flow rate was varied between 0 sLPM and 50 sLPM. Figure 3.17(c) shows the calibration curve plotted between the flow rate (sLPM) and the output voltage (mV).

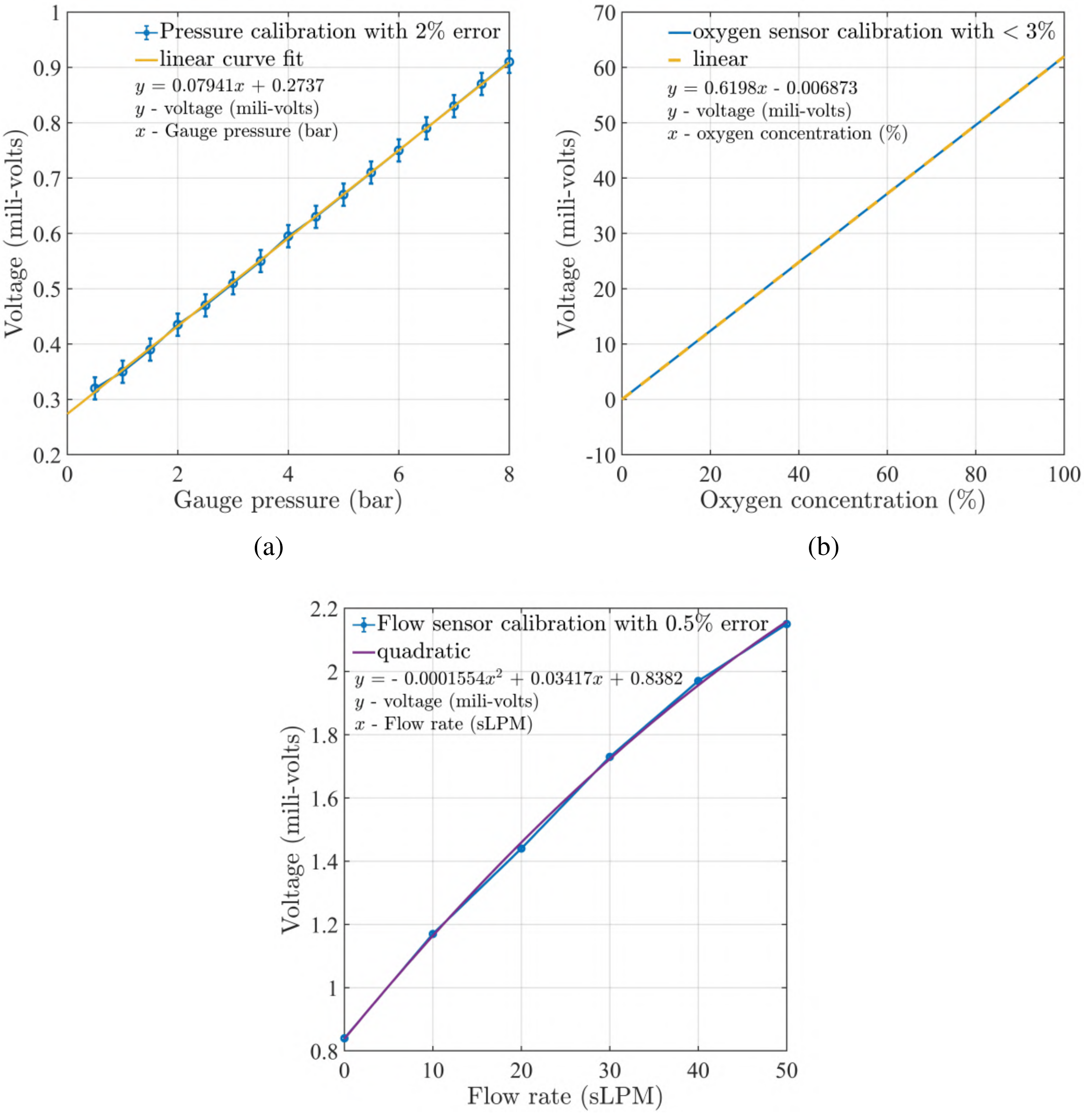

(a) (b)

(c)

Fig. 3.17 Sensor Calibration curves (a) Pressure sensor calibration (b) Oxygen sensor calibration (c) Flow sensor

3.7 Experimental Results and observation

A PSA system can operate with varying degrees of performance based on the several input parameters that control it. These controlling parameters include the pressurisation time, purge time, equalisation time, feed air pressure, and oxygen withdrawal rate from the device. The output is obviously the purity of the oxygen mixture obtained from the device. Typically, the feed air pressure is determined by the compressor's capacity. For the desired configuration of the PSA plant, it would suffice if the compressor could produce flow greater than 15 cfm at 7 bar gauge pressure. In fact, the feed air pressure was maintained at 7 bar for all the experiments considered here. Once the inlet pressure is set, the process simplifies to identifying the optimum times corresponding to pressurization (t_{pres}), purge (t_{pu}), and equalisation (t_{eq}) for obtaining the best purity for a given delivery rate. Hence, different experiments have been performed here by varying these times individually for a set flow rate. As mentioned many times before, the present objective is to obtain >90% O_2 purity mixture from the device at 45 sLPM. In this regard, we carry out systematic optimisation protocol for average flow rates of 31.1 sLPM, 41.7 sLPM, and 45±1 sLPM. Before discussing these optimization results, we now look at the pressure data obtained for the two cylinders for typical values of pressurization, purge, and equalisation times.

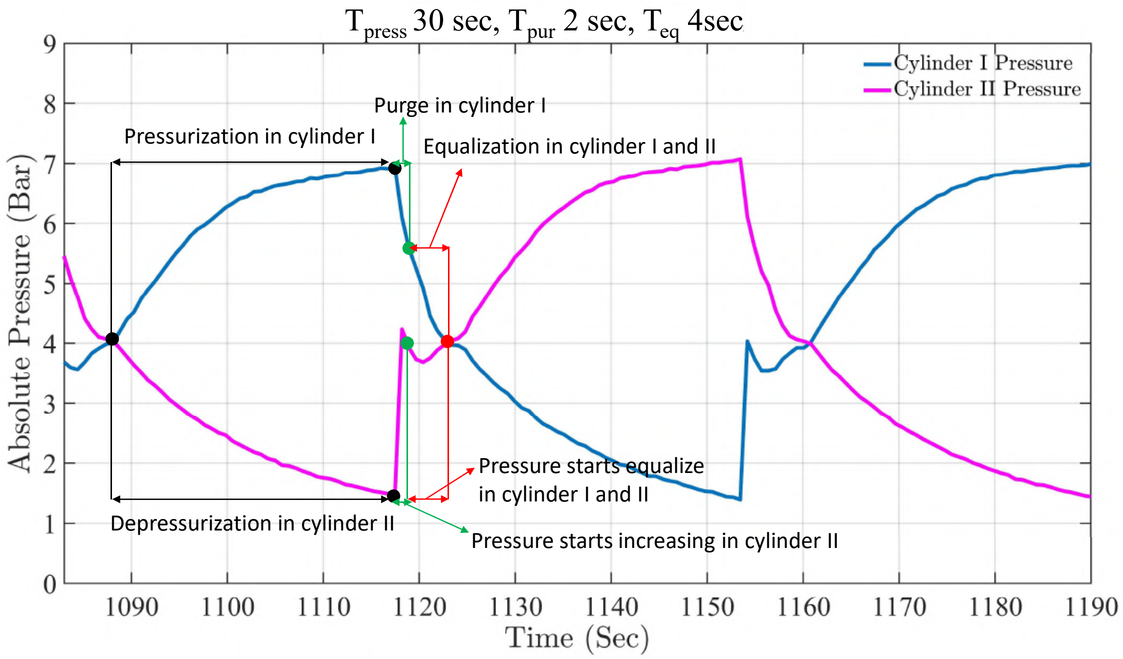

Fig. 3.18 Transient pressure data of both the cylinders

Figure 3.18 shows the experimentally measured pressure data for both the zeolite cylinders for pressurization, purge, and equalization times of 30, 2, and 4 seconds, respectively. Note that the data obtained here corresponds to a state where the system exhibits a cyclic steady state behaviour. The pressure behaviour corresponding to all the constituent steps has been clearly marked in the figure. The pressure signature is identical in both cylinders, and this indicates an excellent symmetry of factors that include sizing of the cylinder, zeolite packing compactness, etc. Here, the cylinders do not reach the set pressure of 8 bar (absolute) during the pressurization step and do not decay to the ambient 1 bar (absolute) pressure during the blow-down process. Since the efficiency of the cycle depends on the peak-to-valley pressure ratio, the observed behaviour might seem sub-optimal. However, it will be shown below that waiting for such pressure targets would be counterproductive with regard to output purity. Note that the purge process increases the pressure of the cylinder undergoing blow-down to around 4 bar before tapering down a bit while the pressure in the other cylinder reduces to $\approx$5.5 bar. In the present configuration, the system allows for backflow from the buffer tank, as it helps quickly flush out the de-adsorbed nitrogen in a short span of 2 sec. During the equalization step, the pressure in the two cylinders equalizes to a value of 4 bar, and there is neither input of feed air to the system nor transfer of gas from the zeolite columns to the buffer tank.

The purity refers to the O2 concentration at the cyclic steady state. In a PSA process, the purity gradually increases once the device start; however, there are some cases where a minor disturbance in the conditions (for example, changing the flow rate and stopping the compressor) alters this transient process. To accommodate all the disturbances in the system, the device is allowed to run for a certain period, where the periodicity is well established, which we often call a cyclic steady state.

So, during our operation, the period was about half an hour, and we observed the oxygen purity to be constant. For example, in table 3.12, the pressurisation time is 26 seconds. For this condition, we ran the device for half an hour and observed that the oxygen purity becomes stable at $94.9\pm1\%$.

t_{pres}	Oxygen concentration (%)	Max gauge pressure (bar)	Min gauge pressure (bar)
14 sec	91.4±0.4	4.565	1.06
18 sec	93.7±0.2	4.935	0.84
22 sec	94.45±0.15	5.4	0.66
24 sec	94.7±0.2	5.566	0.57
26 sec	94.9±0.1	5.825	0.5
30 sec	94.4±0.1	6.23	0.38
34 sec	94.3±0.2	6.615	0.265

Table 3.12 Variation of t_{pres} for flow rate = 31.1 sLPM, t_{pu} = 2.5 s, and t_{eq} = 4 s

t_{pu}	Oxygen concentration (%)	Max gauge pressure (bar)	Min gauge pressure (bar)
1.5 sec	94.45±0.05	5.82	0.505
2.5 sec	94.9±0.1	5.825	0.5
3.5 sec	93.2±0.3	5.765	0.55

Table 3.13 Variation of t_{pu} for flow rate = 31.1 sLPM, t_{pres} = 26 s, and t_{eq} = 4 s

t_{eq}	Oxygen concentration (%)	Max gauge pressure (bar)	Min gauge pressure (bar)
3 sec	94.25±0.15	5.82	0.505
4 sec	94.9±0.1	5.825	0.5

Table 3.14 Variation of t_{eq} for flow rate = 31.1 sLPM, t_{pres} = 26 s, and t_{pu} = 2.5 s

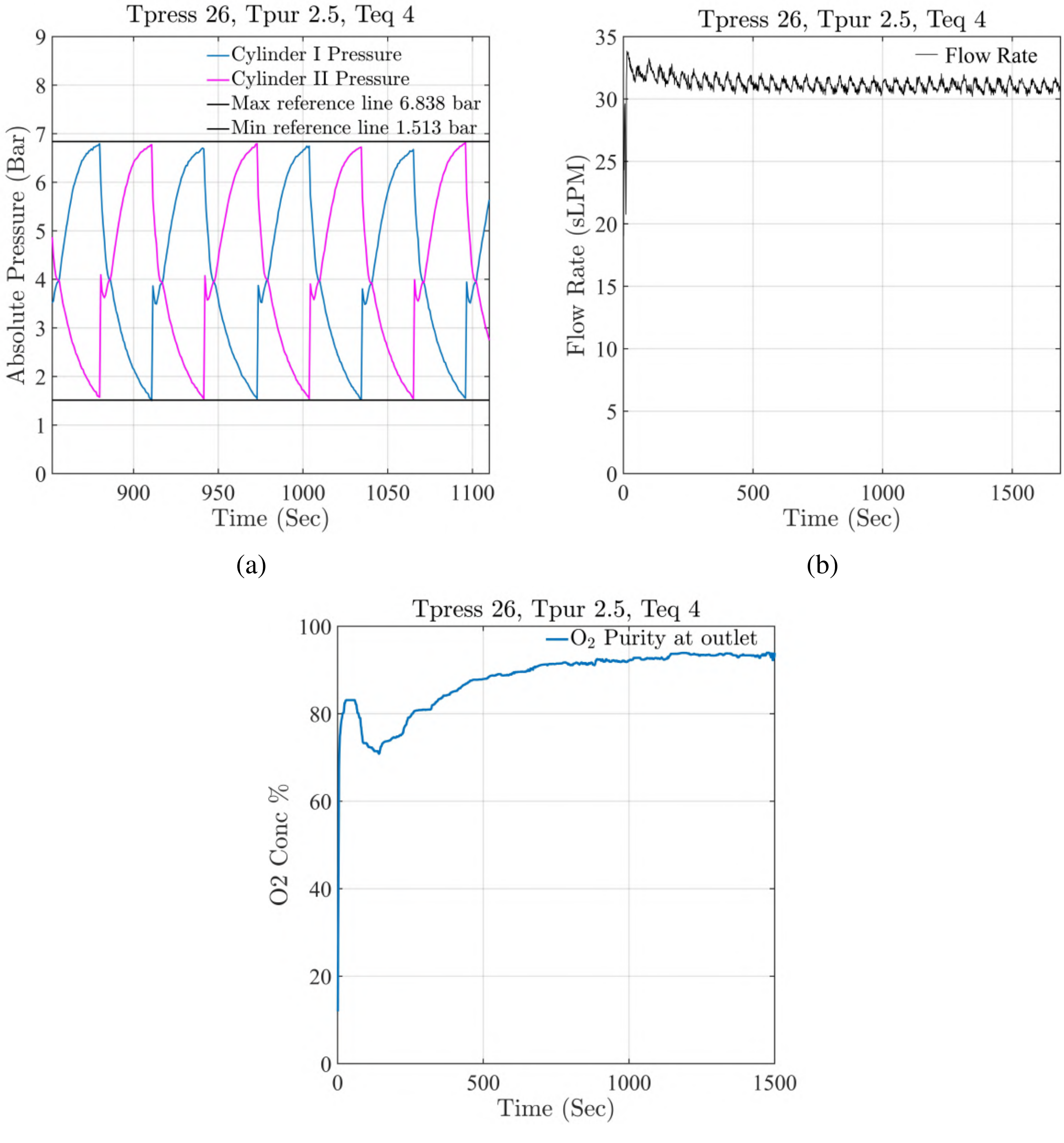

(a)

(b)

(c)

Fig. 3.19 Transient system behaviour for an average flow rate of 31.1 sLPM: (a) Pressure in cylinders 1 and 2 (b) Output flow rate (c) Oxygen purity

t_{pres}	Oxygen concentration (%)	Max gauge pressure (bar)	Min gauge pressure (bar)
18 sec	90.3±0.5	5	0.84
22 sec	91.6±0.4	5.38	0.675
26 sec	92.3±0.5	5.79	0.51
30 sec	92.25±0.55	6.17	0.39
34 sec	92.15±0.45	6.495	0.3

Table 3.15 Variation of t_{pres} for flow rate = 41.7 sLPM, t_{pu} = 2 s, and t_{eq} = 4 s

t_{pu}	Oxygen concentration (%)	Max gauge pressure (bar)	Min gauge pressure (bar)
1.5 sec	92.75±0.55	5.875	0.535
1.75 sec	92.6±0.4	5.84	0.535
2 sec	92.7±0.6	5.845	0.53

Table 3.16 Variation of t_{pu} for flow rate = 41.7 sLPM, t_{pres} = 26 s, and t_{eq} = 4 s

t_{eq}	Oxygen concentration (%)	Max gauge pressure (bar)	Min gauge pressure (bar)
3 sec	92.6±0.4	5.655	0.54
4 sec	92.75±0.55	5.875	0.535
5 sec	91.15±0.55	5.655	0.54

Table 3.17 Variation of t_{eq} for flow rate = 41.7 sLPM, t_{pres} = 26 s, and t_{pu} = 1.5 s

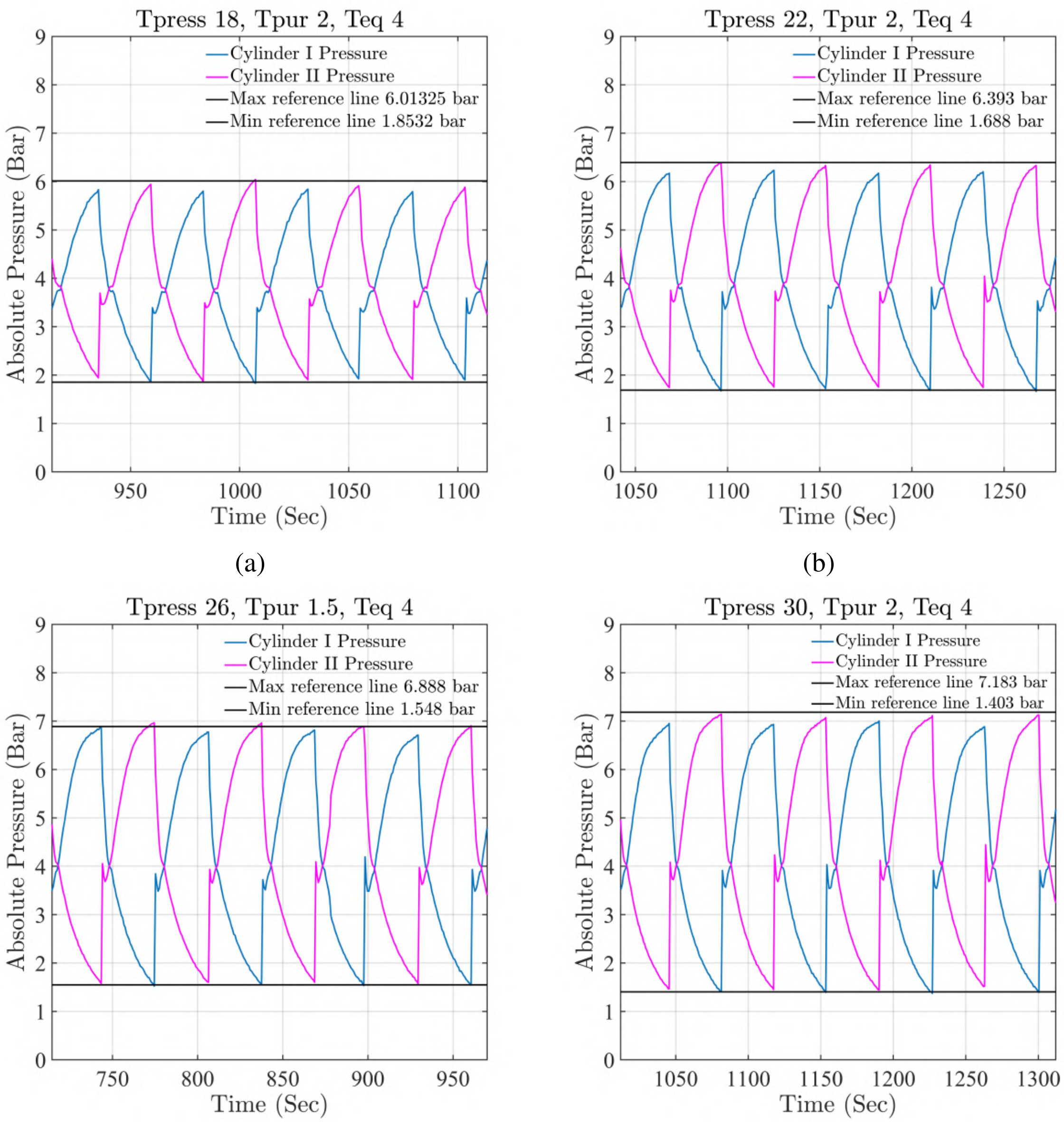

(a) (b)

(c) (d)

Fig. 3.20 Pressure curves comparison for flow rate 41.7 sLPM: (a) $T_{Pres} = 18\,s, T_{Pu} = 2\,s, T_{eq} = 4\,s$ (b) $T_{Pres} = 22\,s, T_{Pu} = 2\,s, T_{eq} = 4\,s$ (c) $T_{Pres} = 26\,s, T_{Pu} = 1.5\,s, T_{eq} = 4\,s$ (d) $T_{Pres} = 30\,s, T_{Pu} = 2\,s, T_{eq} = 4\,s$

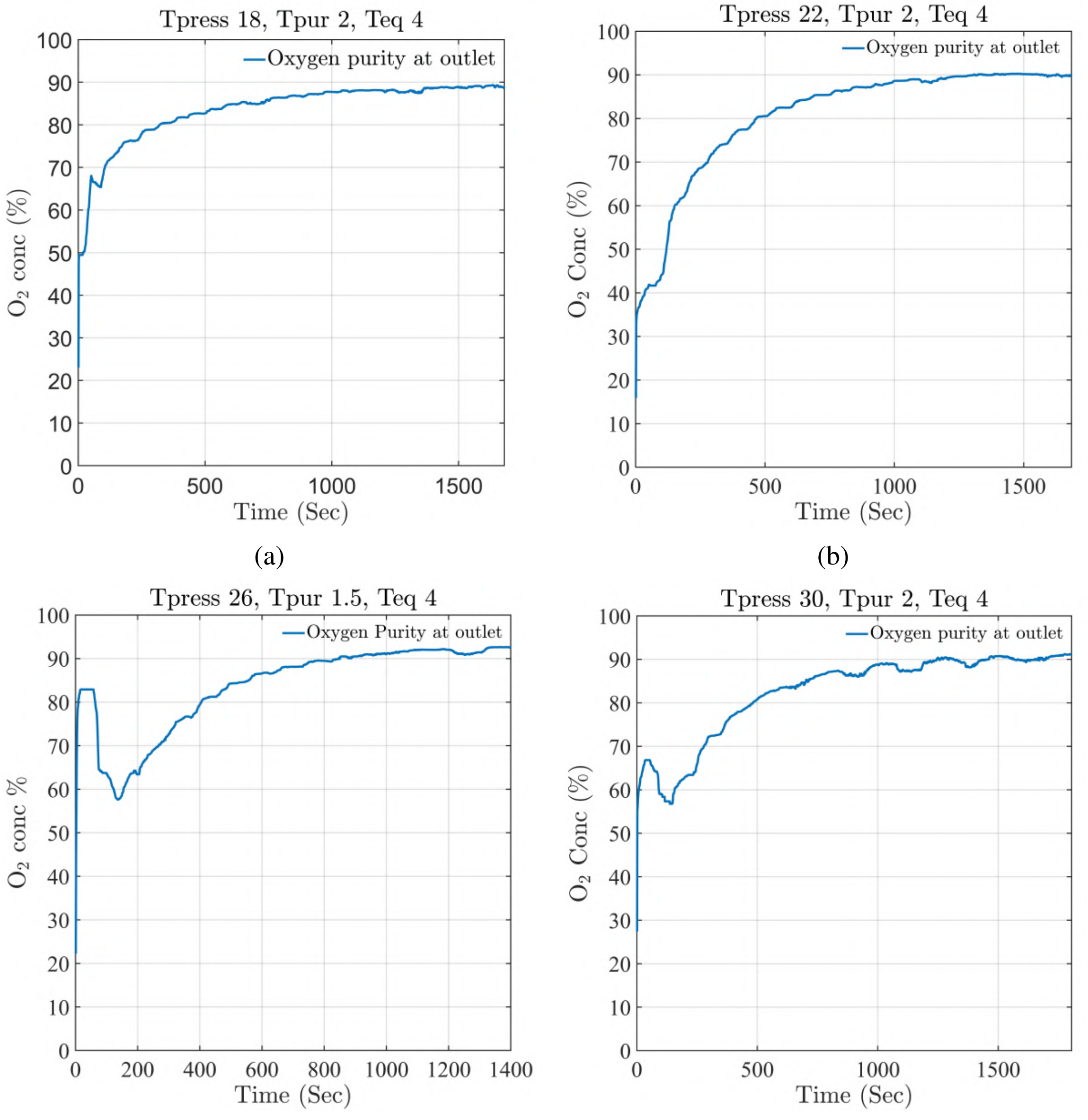

(a) (b)

(c) (d)

Fig. 3.21 Oxygen purity comparison for an average flow rate of 41.7 sLPM (a) $\mathrm{T_{Pres} = 18\,s, T_{Pu} = 2\,s, T_{eq} = 4\,s}$ (b) $\mathrm{T_{Pres} = 22\,s, T_{Pu} = 2\,s, T_{eq} = 4\,s}$ (c) $\mathrm{T_{Pres} = 26\,s, T_{Pu} = 1.5\,s, T_{eq} = 4\,s}$ (d) $\mathrm{T_{Pres} = 30\,s, T_{Pu} = 2\,s, T_{eq} = 4\,s}$

t_{press}	Oxygen concentration (%)	Max gauge pressure (bar)	Min gauge pressure (bar)
18 sec	84.65±0.35	4.865	0.83
22 sec	88.15±0.75	5.1	0.68
26 sec	89.75±0.75	5.45	0.505
30 sec	90.9±0.8	6.045	0.385
34 sec	90.55±0.95	6.385	0.28

Table 3.18 Variation of t_{pres} for average flow rate = 45 sLPM, t_{pu} = 2 s, and t_{eq} = 4 s

t_{pur}	Oxygen concentration (%)	Max gauge pressure (bar)	Min gauge pressure (bar)
1.5 sec	90.05±1.05	6.125	0.39
2 sec	90.9±0.8	6.045	0.385
2.5 sec	89.7±1.4	5.835	0.38

Table 3.19 Variation of t_{pu} for average flow rate = 45 sLPM, t_{pres} = 30 s, and t_{eq} = 4 s

t_{eq}	Oxygen concentration (%)	Max gauge pressure (bar)	Min gauge pressure (bar)
3 sec	90.15±1.15	5.71	0.32
4 sec	90.9±0.8	6.045	0.385
5 sec	90.1±1.4	5.92	0.32

Table 3.20 Variation of t_{eq} for average flow rate = 45 sLPM, t_{pres} = 30 s, and t_{pu} = 2 s

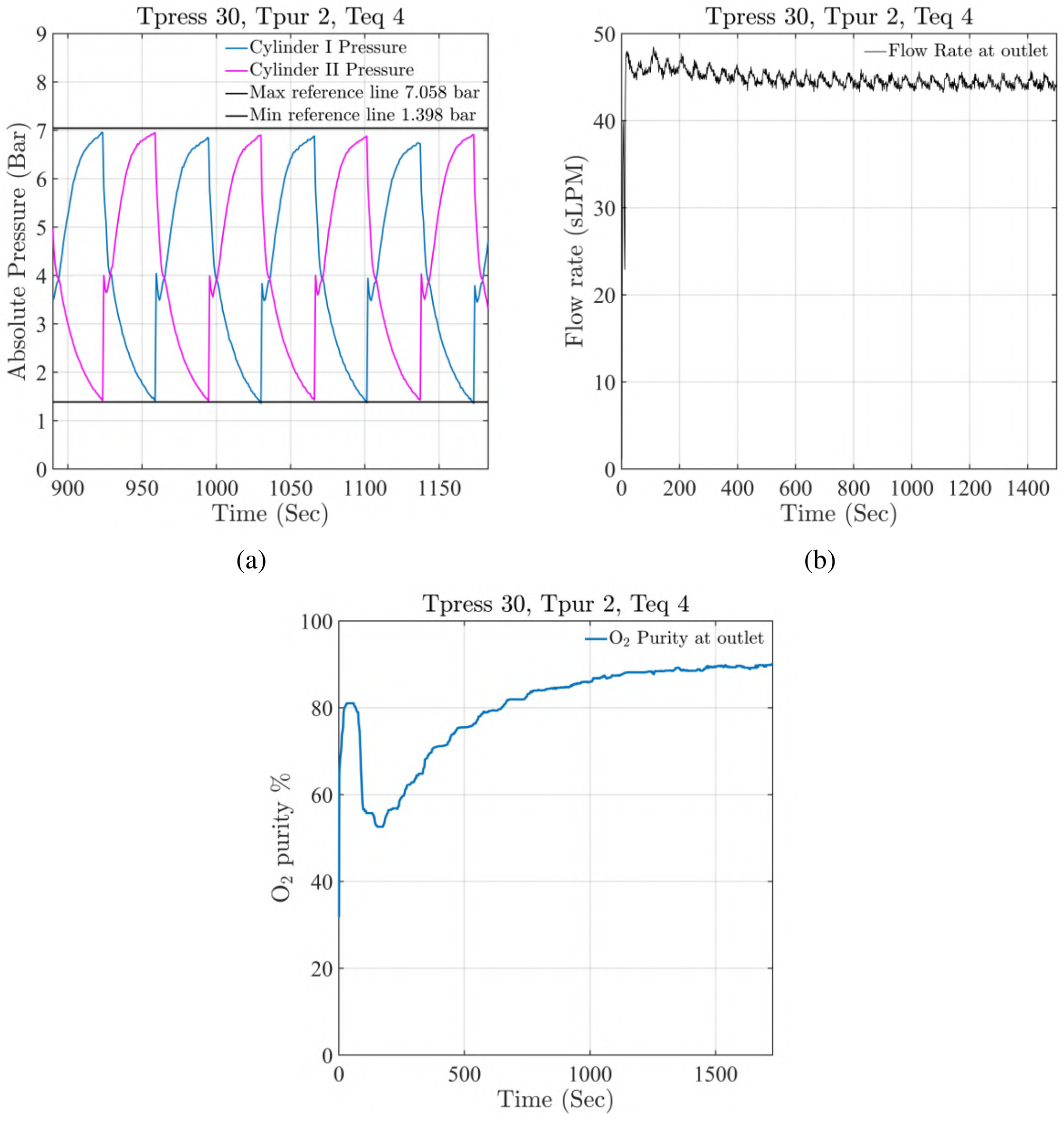

(a)

(b)

(c)

Fig. 3.22 Transient system behaviour for an average flow rate of 45 sLPM: (a) Pressure in cylinders 1 and 2 (b) Output flow rate (c) Oxygen purity

All the results obtained from the current version of the device have been categorised under different tables (Table 3.12 to Table 3.20). The corresponding transient data on cylinders' pressure, flow rate, and oxygen purity have been presented in Figs. 3.19 to 3.22. These tables and figures depict the device's behaviour for different outlet flow rates, pressurisation, purge, and equalisation times. The time for reaching a cyclic steady state(CSS) depends on the dimension of the packed bed. Smaller the system sizing, faster is the attainment of CSS.

The dip in the purity is due to the following reasons:

- When the experiments were started, invariably there was residual oxygen in the pipelines. That residual oxygen gives the initial jump in the purity curve.
- As time progresses, this gets conditioned by concentrated oxygen coming from the zeolite cylinder.
- Thus, the purity of any device should be noted (observed) only at the cyclic steady state.

Note that every time the experiments start for a particular condition, the initial state (concerning the residual concentrated oxygen trapped) is not identical. One can observe the difference in the initial jump for different experimental conditions.

Understandably, the three step-times control the adsorption/desorption process in the zeolite columns, thereby determining the oxygen purity in the out-flowing gas. Hence, optimum values for the three times should be obtained for any given flow rate so that the best performance and recovery can be obtained from the device. We now look at the influence of these times individually.

3.7.1 Influence of pressurization time

Tables 3.12, 3.15, and 3.18 show the output purity and the peak pressure obtained in the columns for average flow rates of 31.1 sLPM, 41.7 sLPM, and 45 sLPM, respectively. The transient pressure data of both the cylinders and the output purity have been specifically plotted for 41.7 sLPM in Figs. 3.20 and 3.21, respectively. It is evident from the isotherm graphs of NaX that the quantity of nitrogen adsorbed and desorbed in the zeolite material is proportional to the maximum and minimum pressures attained in the columns. Thus, the ability of the zeolites to cyclically adsorb nitrogen and thereby supply oxygen-rich output depends on the peak-to-valley pressure ratio in the columns. Note that efficient desorption is as essential as adsorption since the process makes the adsorption sites effectively available for the next cycle. Hence, it is easy to fathom that larger pressure ratios lead to better performance of the device. The pressurisation time effectively determines this ratio for

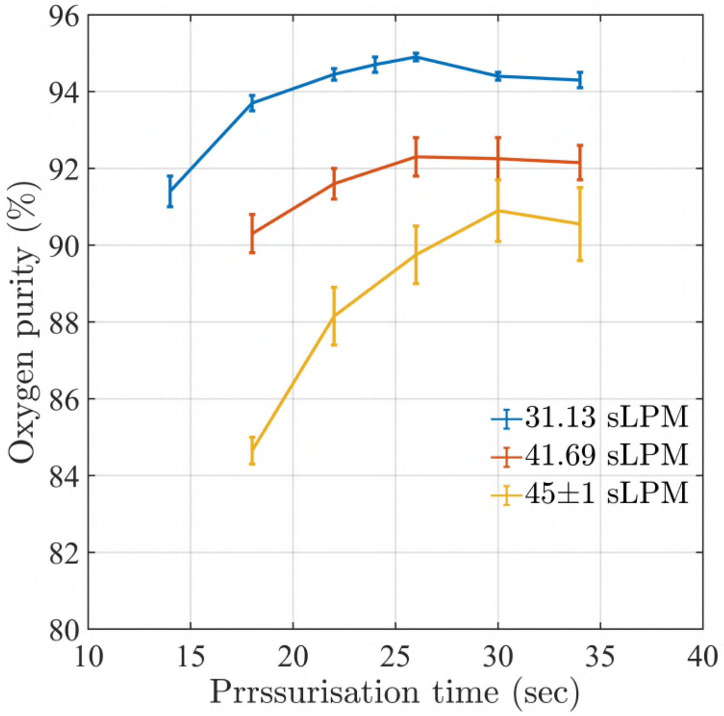

Fig. 3.23 Oxygen purity with varying pressurisation time for different flow rates

a given system. A proper valve of t_{pres} allows sufficient time for adsorption during the pressurization process and desorption during the blow-down process. While the lower valves of t_{pres} lead to insufficiency in both these processes, a larger value results in saturation of the zeolite bed with adsorbed nitrogen. This is precisely evident from Tables 3.12, 3.15, and 3.18 where the optimum pressurisation time at the three different flow rates are 26 s, 26 s, and 30 s, respectively. The behaviour at t_{pres} larger than these values is sub-optimal despite them resulting in a larger peak-to-valley ratio for the column pressure. In these scenarios, the pressure value is closer to saturation, and the N_2 adsorption process could have attained breakthrough. Figure 3.23 summarises the purity obtained for different t_{pres} at the three flow rates considered. Here, the error bar shows the fluctuation of oxygen purity at the outlet.

3.7.2 Influence of purge time

We now follow a similar procedure as above for the purge time. Tables 3.13, 3.16, and 3.19 show the output purity and the pressure extremes obtained in the columns for different purge times and flow rates. As discussed earlier, the purge step essentilly flushs out the remaining desorbed nitrogen from the zeolite cylinder after blow-down so that the columns are fully replenished for the next cycle. Evidently, there is also an optimum value associated with the purge step. A value smaller than this optimum would result in insufficient flushing whereas a larger purge time would result in wasting high purity oxygen mixture. Note that the present valve configuration allows for backflow of high purity oxygen from the buffer tank to the zeolite columns. This configuration greatly helps in shorting the time required for making the flushing process complete. Correspondingly, the optimum purge time for all the flow rates considered is close to 2 s.

3.7.3 Influence of equalisation time

Finally, an optimization process is carried out to identify the proper equalization time for the cycle at different flow rates. Here again, one can expect to obtain an optimum value. Though a larger equalization time would help attain proper equalisation of pressure in the two zeolite cylinders, it is also deleterious as it results in the stoppage of flow to the buffer tank, which can only supply the desired output for a short while. Incidentally, a shorter equalisation time would lead to an incomplete process. Tables 3.14, 3.17, and 3.20 show that the optimum equalisation time for all the flow rates considered is around 4 s.

It can be observed from Tables 3.12, 3.13 and 3.14, outlet oxygen purity does not change very significantly with different parameters at the flow rate of 31.1 sLPM. This indicates that the device is well within its best-operating conditions. Only at the flow rate of 41.7 sLPM, the output purity starts to display the influence of different parameters. Finally, at 45 sLPM, the parametric influences are notable. Beyond 45 sLPM, obtaining oxygen purity greater than 90% would be very challenging.

Note that the local fluctuations in flow rates, as observed in Figs. 3.19b and 3.22b, is essentially due to the fluctuations in the buffer tank pressure. Interestingly, some of the transient oxygen purity curves show a sudden jump in the purity at the start of the device. This behaviour could be essentially due to trapped oxygen inside the zeolite columns and the buffer tank from the previous trials. In the current work, we ignore these initial transients and use the values obtained after 20 mins of device operation.

3.8 Conclusion

In the present chapter, a systematic study of experimental setups, starting from tabletop designs to the fully functional prototype, has been carried out, detailing the optimum performance of the devices, their limitations, etc. Notably, the final design, with its different individual components, types of valves used, valve configuration, etc., have been discussed in detail. A brief summary of the sensors' calibration data has also been included.

The parametric studies have been performed for different flow rates, i.e., 31.13 sLPM, 41.69 sLPM, and 45±1 sLPM, by varying pressurisation, purge, and equalisation times individually. The results explain the dependency of each time on the device performance in detail. The existence of optima for all three time scales has been shown conclusively, along with the logical reasoning behind its existence.

It can be summarized from the current trials that the l/d ratio of the zeolite columns should be between 4 to 6 to avoid both mal-distribution of flow within the column and prevent significant pressure drop in the cylinder. Also, a spring compression mechanism is necessary to avoid particle fluidisation and powder formation. In the process, ensuring that the resulting void volume in the domain is as minimum as possible is essential.

In the next chapter, we deal with the complete modeling of the PSA plant for oxygen concentration.

Chapter 4

Numerical Simulation of PSA plant

4.1 Introduction to the chapter

The experimental results presented in the previous chapter revealed the influence of various input parameters, such as the l/d ratio, the dead volume, the pressurization, purge and equalization times, etc., on the overall performance of the PSA system. Here, the performance was measured solely in terms of the output purity of the oxygen mixture, withdrawn at different flow rates. Despite helping in obtaining the optimum parameters of operation for a particular design, the data do not reveal the intrinsic details of the PSA process, including the extent of active adsorption in the device and the temperature change during the adsorption/desorption process, etc. Thus, an accurate mathematical model of the PSA plant would help investigate the detailed behaviour of the device. Such modeling would focus on obtaining the spatio-temporal evolution of field variables such as pressure, velocity, temperature, and species concentration in the adsorbent bed and the other areas. The numerical model would also act as a niche optimization tool for developing new designs and can help avoid costly and time-consuming experimental testing. The computer simulations should be accurate and fast and offer greater flexibility. In this regard, the current chapter describes a detailed mathematical model of the complete PSA plant developed using an axisymmetric geometry consisting of two zeolite cylinders and one oxygen storage tank.

The model conserves mass, momentum, energy, and species transport in the gas media that contains a mixture of nitrogen and oxygen. The presence of zeolite particles was modelled via the porous media consideration wherein adsorption-desorption processes were accounted for by adding appropriate source/sink terms in the above conservation equations. The sequence of valve actions (opening and closing) installed in the PSA plant was simulated by swapping appropriate boundary conditions from interior/interface to wall and vice versa.

We now begin the chapter with details on different conservation equations, followed by three validation cases performed to authenticate the model. We then describe the numerical model of the present PSA device, followed by detailed simulations and their results.

4.2 Mathematical modelling for species adsorption in porous media

4.2.1 Mass conservation equation

The typical conservation of gas mass in the domain is given as

$$\frac{\partial \rho}{\partial t} + \nabla.(\rho u) = 0, \tag{4.1}$$

where u is the fluid physical velocity and ρ is the density of the fluid. In the zeolite columns (porous), Eq. (4.1) gets modified with porosity ε as

$$\frac{\partial \varepsilon \rho}{\partial t} + \nabla.(\varepsilon \rho u) = S_m, \tag{4.2}$$

where S_m is the volumetric source term that accounts for adsorption and desorption in the zeolite (porous) media. Note that the superficial/Darcy velocity (v) and seepage/interstitial velocity (u) are related as follows:

$$v = \varepsilon u \tag{4.3}$$

The superficial velocity, typically used to describe the flow through porous media, is defined as

$$v = \frac{Q}{A}. \tag{4.4}$$

Here, Q is the volume flow rate in SI units, and A is the cross-sectional area of the porous medium.

4.2.2 Momentum Conservation equation

The equation for momentum conservation for a gas flow through a typical non-porous region like the interconnecting pipes is given as [12]

$$\frac{\partial (\rho u)}{\partial t} + \nabla.(\rho u u) = -\nabla P + \mu \nabla^2 u, \tag{4.5}$$

whereas through a porous media, the momentum conservation equation for the gas flow is written as[12]

$$\varepsilon\frac{\partial(\rho v)}{\partial t}+\nabla.(\rho vv)=-\nabla P+\mu\nabla^2 v+S_f \tag{4.6}$$

Here, μ is the dynamic viscosity of the gaseous mixture, and S_f is the momentum source term contribution from the porous media.

4.2.3 Energy conservation equation

The energy equation assumes a proper thermal equilibrium between the gas and the porous media. The equation accounts for the energy transfer owing to flow advection, pressure work, and thermal diffusion in addition to the energy released/consumed due to adsorption/desorption processes. It is written as [7]

$$\frac{\partial[\varepsilon\rho E_g+(1-\varepsilon)\rho_p E_s]}{\partial t}+\nabla.(v(\rho E_g+P))=\nabla.\left[k_{eff}\nabla T-\sum_i h_i\vec{J}_i+\mu(\nabla v).v\right]+S_E, \tag{4.7}$$

where E_g is the total gas energy, and E_s is the total adsorbent energy. S_E is the source term, h_i is the sensible heat energy ($h=\sum_i y_i h_i$), and $\vec{J}_i$ is the diffusive flux of the gas component i. The parameter k_{eff} is the effective thermal conductive of the bed and is expressed as [7]

$$k_{eff}=\varepsilon k_g+(1-\varepsilon)k_s. \tag{4.8}$$

k_g and k_s are the thermal conductivities of the gas media and the solid, respectively.

4.2.4 Species transport equation

The scalar transport equation associated with the conservation of individual species (N_2 and O_2) along with their adsorption/desorption is written as [12]

$$\frac{\partial(\varepsilon\rho y_i)}{\partial t}+\nabla.(\rho y_i v)=-\nabla.(-\varepsilon\rho D_{disp}\nabla y_i)+S_s, \tag{4.9}$$

where y_i is the mass fraction of the i^{th} species. D_{disp} is the mass dispersion coefficient, and S_s is the source/sink term associated with desorption/adsorption. Note that the axial dispersion coefficient in the species transport equation, Eq.(4.9), can be calculated using the following correlations [12]

$$D_{Disp}=1.968\frac{d_p v}{Re^{0.02}};\ Re=\frac{\rho v d_p}{\mu} \tag{4.10}$$

where d_p is the particle diameter.

4.2.5 The momentum source

The source terms in all the above equations are active only in the porous zeolite media. The momentum source in Eq. (4.6) can be calculated using Ergun's equation [12] as

$$S_f = -\left(\frac{\mu}{\kappa}v_i + \frac{1}{2}C_2\rho|v|v_i\right), \tag{4.11}$$

where μ is the dynamic gas viscosity. $\frac{1}{\kappa}$ is the inverse of permeability of the medium, which is also termed as viscous resistance, and C_2 is the inertial resistance (m^{-1}). Here, the viscous resistance is defined as

$$\frac{1}{\kappa} = \frac{150(1-\varepsilon)^2}{{d_p}^2\varepsilon^3} \tag{4.12}$$

and the inertial resistance is defined as

$$C_2 = \frac{3.5(1-\varepsilon)}{d_p\varepsilon^3} \tag{4.13}$$

4.2.6 The other source terms

As discussed earlier, the process of adsorption/desorption in the porous media gives rise to source terms in the mass, species transport, and energy equations. Correspondingly, the species source term for i^{th} species in Eq. (4.9) is defined as

$$S_S = -(1-\varepsilon)\rho_p M_i\frac{\partial q_i}{\partial t}, \tag{4.14}$$

and the source/sink term in the mass conservation equation, Eq. (4.2), is given as

$$S_m = -(1-\varepsilon)\rho_p\sum_i M_i\frac{\partial q_i}{\partial t}. \tag{4.15}$$

Here ρ_p is the adsorbent particle density (Kg/m^3). q_i is the quantity of particular species adsorbed (mol/kg) and M_i is the molecular weight of the i^{th} species. The energy source term which incorporates the exothermic/endothermic behaviour of the adsorption/desorption process in Eq. (4.7) is defined as

$$S_E = (1-\varepsilon)\rho_p\sum_i \Delta H_i\frac{\partial q_i}{\partial t} \tag{4.16}$$

where ΔH_i is the heat of adsorption for an individual species.

The term $\frac{\partial q_i}{\partial t}$ for any species is estimated via the linear driving force model (LDF), that accounts for the difference between the amount of actual adsorption and the maximum capacity of adsorption derived from the adsorption isotherms. The details of the LDF model are explained in the following section. But, before that, we take a quick look at the other associated equations that help determine different fluid properties.

4.2.7 Associated equations

The physical properties, such as thermal conductivity, viscosity, etc., depend on pressure and temperature; hence, they are calculated using relevant averaging processes. Here, the gas's thermal conductivity and viscosity are obtained using the mixing law [7] as given below.

$$\kappa = \sum_i \frac{x_i \kappa_i}{\sum_j x_j \phi_j}, \quad \mu = \sum_i \frac{x_i \mu_i}{\sum_j x_j \phi_j}, \quad \phi_{ij} = \frac{\left[1 + \left(\frac{\mu_i}{\mu_j}\right)^{\frac{1}{2}} \left(\frac{M_j}{M_i}\right)^{\frac{1}{4}}\right]^2}{\left[8\left(1 + \frac{M_i}{M_j}\right)\right]^{\frac{1}{2}}}, \tag{4.17}$$

where x_i and M_i are the molar fraction and molar mass of the species, i, respectively.
The mixture-gas density is obtained as

$$\rho_g = \frac{P}{RT \sum_i \left(\frac{y_i}{M_i}\right)}, \tag{4.18}$$

where, P is the absolute pressure and y_i is the mass fraction of the i^{th} species.

4.2.8 Modelling adsorption

As mentioned before, the adsorption kinetics are evaluated using the linear driving force (LDF) model, as shown below[76].

$$\frac{\partial q_i}{\partial t} = k_{L,i}(q_i^* - q_i), \tag{4.19}$$

where $k_{L,i}$ is the overall mass transfer coefficient of the species. q_i^* is the maximum quantity of a particular component that can be adsorbed in the zeolite at equilibrium, and q_i is the actual amount of adsorption in the zeolite. The quantity, q_i^*, is a strong function of pressure and temperature, and different adsorption models are available to estimate this value [84]. In the next section, we will have a brief look at the three popular adsorption isotherm models namely: Langmuir, Langmuir-Freundlich, and Toth isotherms.

Multi-component Langmuir isotherm

The multi-component Langmuir isotherm considers a homogeneous distribution of the gas molecules on the surface and is defined as

$$q_i^* = \frac{q_{mi} b_i P_i}{1 + \sum_{j=1}^{n} b_j P_j}, \tag{4.20}$$

where q_{mi}, b_i, and P_i are the maximum adsorption capacity (kg of gas adsorbed / kg of adsorbent), Langmuir isotherm constant, and the partial pressure of the i^{th} species, respectively. Obviously, if $j = 1$, then Eq. (4.20) is known as the single component Langmuir isotherm.

Toth Isotherm

Toth isotherm explicitly incorporates the heterogeneity of the multi-component adsorption process, and its definition is given below. Note that Toth isotherm has been used in the current work for a few validation cases.

$$q_i^* = \frac{q_{mi} K_{eq,i} y_i P_i}{\left(1 + (K_{eq,i} y_i P_i)^{ni}\right)^{\frac{1}{ni}}} \tag{4.21}$$

Here, ni and $K_{eq,i}$ are constants wherein $K_{eq,i}$ is particularly obtain as

$$K_{eq,i} = k_o e^{\left(-\frac{\Delta H}{RT}\right)} \tag{4.22}$$

k_o is a temperature-independent constant, ΔH is the heat of adsorption, and R is the universal gas constant (J/mol-K).

Langmuir-Frendluich Isotherm

The Langmuir–Freundlich (L-F) isotherm considers surface heterogeneity in addition to the basic assumptions of the Langmuir isotherm model. Hence, this isotherm is quite practical and useful for studying adsorption equilibrium. The L-F isotherm is defined as [42]

$$q_i^* = \frac{q_{mi} B_i P^{ni}}{1 + \sum_{j=1}^{n} B_j P_j^{nj}}, \tag{4.23}$$

where $q_m = K_1 + K_2T$, $B = K_3exp\left(\frac{K_4}{T}\right)$, and $ni = K_5 + \frac{K_6}{T}$, is the index of heterogeneity.

4.2.9 Boundary Conditions

Inlet boundary conditions

In the present PSA system, the inlets to the zeolite columns are fitted with pipes, and hence, there is no need for any explicit condition other than specifying the value of pressure, temperature, and species concentration. However, for certain validation cases where the flow directly enters a porous region, there is a need for an explicit balance between the diffusion and advection of heat and mass transport. Such a balance can be achieved using the following relations [35].

$$-\varepsilon D_{m,i}\nabla y_i|_{z=0} = v_{z=0}(y|_{i,feed} - y|_{z=0}) \tag{4.24}$$

$$-\varepsilon k_{eff}\nabla T = v\rho(h|_{i,feed} - h|_{z=0}) \tag{4.25}$$

Outlet boundary conditions

At the outlet of the domain, the conditions for the heat and mass fluxes are written as

$$\nabla y_i = 0 \tag{4.26}$$

$$\nabla T = 0 \tag{4.27}$$

Boundary conditions for heat transfer at the external walls

The heat transfer between the zeolite column wall and the ambient can be obtained as

$$k_w\left(\frac{\partial T_w}{\partial n}\right)_W = h_{ext}(T_W - T_{amb}), \tag{4.28}$$

where n is the local direction cosines normal to the zeolite tank surface, h_{ext} is the external heat transfer coefficient, T_w and T_{amb} are the wall and ambient temperatures, respectively. h_{ext} is calculated using the following Nusselt number correlation.

$$Nu = \frac{h_{ext}D_o}{k_{air}} = \left[0.6 + 0.387\frac{Ra^{\frac{1}{6}}}{\left[1 + \left(\frac{0.559}{Pr_{air}}\right)^{\frac{9}{16}}\right]^{\frac{8}{27}}}\right]^2 \tag{4.29}$$

Here, D_o is the external wall diameter, k_{air} is the air thermal conductivity at average temperature, Pr_{air} is the Prandtl number of air, and Ra is the Rayleigh number. The maximum change in temperature observed at the wall of the tank from the simulations due to adsorption/desorption is around 10°C. Hence in the present work, we consider h_{ext} to be a constant value of 8 $W/m^2 - K$, as obtained from the above correlation for 10°C temperature difference.

4.3 Validation cases

Before venturing into the task of modelling the full PSA plant, we consider three simple cases to assess the performance of the tailored model utilised here against the published literature. These three cases are as follows:

1. *"Modelling a generic breakthrough curve for adsorption process"*[70].
2. *"Separation of Carbon dioxide from CO_2/N_2 mixture"*[12].
3. *"Separation of carbon dioxide-nitrogen using activated carbon in a fixed bed"* [25].

Note that all the simulations in this work have been performed using the commercial package ANSYS-FLUENT where the source terms have been explicitly calculated via user-defined functions (UDFs).

4.3.1 Case 1

The first case is a simple test scenario where a pipe filled with zeolite material is considered, and a single species of gas is made to undergo adsorption in the zeolite. The interest is to essentially find out the time at which the species starts to break through at the other end of the pipe. The following assumptions were considered in the FLUENT simulations [70]:

1. The system is isothermal.
2. The pressure drop across the bed is negligible.
3. Flow velocity is constant across the bed.
4. The mass transfer rate is calculated using the LDF model, as described in Eq.(4.19).
5. Langmuir isotherm (Eq. (4.20)) model is considered.
6. The assumption of ideal plug flow is considered.

The different bed and adsorption properties utilised for the simulations are listed in Table. 4.1. For the sake of comparison, a 1D MATLAB code was written to solve the single species transport equation without the diffusion (Eq.(4.30)) that represents the current behaviour.

$$\frac{\partial C_i}{\partial t} + u\frac{\partial C_i}{\partial x} = \frac{1-\varepsilon}{\varepsilon}\rho_p\frac{\partial q_i}{\partial t} \tag{4.30}$$

Parameter	Value
Bed Length, L (m)	0.5
ε	0.4
u, velocity (m/s)	0.01
k_L (1/sec)	0.5
b, Langmuir constant (m^3/kg)	0.3
q_m (mol/kg)	0.04
c_o, inlet concentration (kg/m^3)	1
ρ_p	1000

Table 4.1 Bed geometry and adsorbent properties for single component adsorption [70]

Figure 4.1 shows an excellent comparison between the two models. One can extend the present problem statement to include multi-component adsorption/breakthrough. This problem is similar to the single component consideration; however, the gas is fed with two species, and the interest is to understand the competition between the two species for the breakthrough. Once again, a MATLAB code was written to solve the species transport equation and the source term individually for each species using the explicit Euler technique. The properties and adsorption constants used for the multi-species case are listed in Table. 4.2.

Parameter	Value
Bed Length, L (m)	0.3
ε	0.4
u, velocity (m/s)	0.01
k_{L1} (1/sec)	1.5
k_{L2} (1/sec)	1.5
b_1 $((m^3/kg))$, Langmuir constant	0.4
b_2 (m^3/kg), Langmuir constant	0.3
q_{m1} (kg/m^3)	0.04
q_{m2} (kg/m^3)	0.03
c_{1o} (kg/m^3), inlet concentration for component 1	0.75
c_{2o} (kg/m^3), inlet concentration for component 2	0.25
ρ_p (kg/m^3)	800

Table 4.2 Bed geometry and adsorbent properties for multi-component adsorption for case 1 (B) [70]

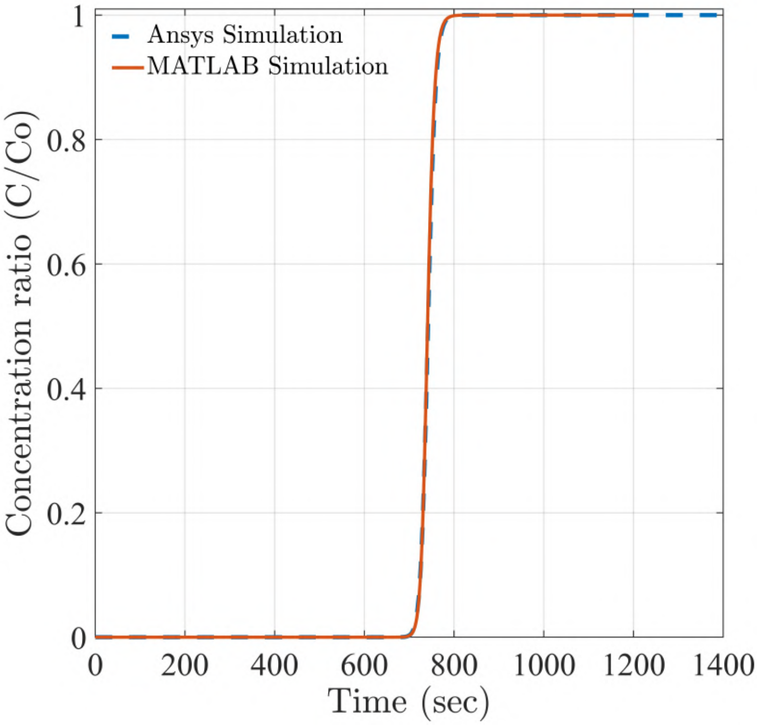

Fig. 4.1 Single component breakthrough curve for case 1

The resulting breakthrough curves for multi-species adsorption are shown in Fig. 4.2. Once again, there is a good agreement between the breakthrough curves obtained from the FLUENT and MATLAB models.

4.3.2 Case 2

The second validation problem offers a more realistic perspective where we solve the complete set of mass, momentum, species transport, and energy conservation equations along with their respective source terms calculated via user-defined functions (UDFs) in ANSYS FLUENT.

The geometry of the problem is shown in Fig. 4.3, and the following assumptions were adopted[12] for the simulations.

- The ideal gas law is followed by the gas phase.
- The flow is assumed to be unsteady and laminar ($Re < 10$).
- Homogeneity is maintained for porous medium
- Constant physical properties of adsorbents is assumed
- Mass transfer during the adsorption process is calculated using the linear driving force (LDF) model.

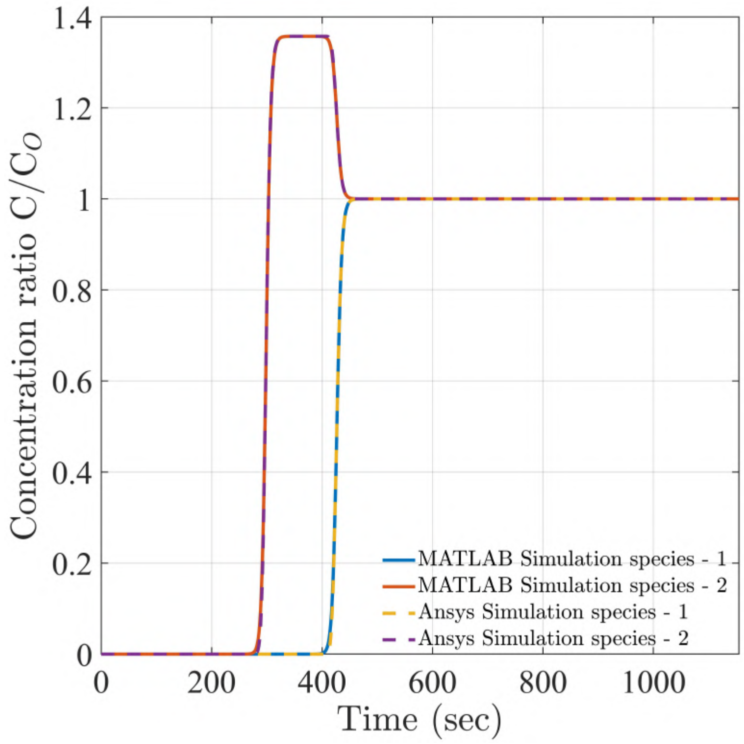

Fig. 4.2 Multi component breakthrough curve for the case I (A)

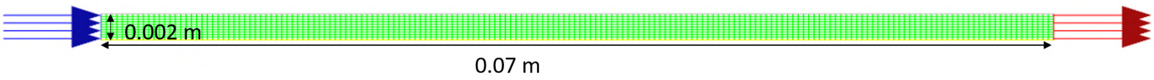

Fig. 4.3 Geometry for case II

- The gas phase and the adsorbent are assumed to be in thermal equilibrium.
- The two species considered are CO_2 and N_2.
- Initially, the bed is filled with helium gas.

The bed geometries and adsorbent constants are listed in Table 4.3[12]. Figure 4.4 shows the comparison of breakthrough curves from the present FLUENT simulations and the experimental/numerical data of Ben-Mansour et al.[12]. It can be observed that the present breakthrough curves reasonably mimic the experimental data of Ben Monsour [12]. However, there is a notable difference between the numerical curves obtained from the two works. The reason for this behaviour can be attributed to the choice of different sub-models in FLUENT. Unfortunately, Ben Monsour et al. [12] have not provided details about all their sub-models, forcing us to make a few choices of our own.

Properties	**Value**
Bed Length, L(m)	0.07
Bed diameter, D(m)	0.004
Bed Wall thickness (m)	0.001
Particle density ρ_p (Kg/m^3)	911
Adsorbent particle size, d_p (m)	0.0002
Bed porosity ε	0.7417
CO_2 inlet molar fraction x_{CO_2}	0.2
N_2 inlet molar fraction x_{N_2}	0.8
CO_2 adsorption time constant coefficient K_{L,CO_2} (1/sec)	0.1182
N_2 adsorption time constant coefficient K_{L,N_2} (1/sec)	0.3043
CO_2 species q_m (mmol/kg)	11.4048
N_2 species q_m (mmol/kg)	6.702
K_{o,CO_2} (1/Pa)	3.089e-11
K_{o,N_2} (1/Pa)	9.36e-10
n_{CO_2}	0.4217
n_{N_2}	1
$-\Delta H_{CO_2}$ (J/mol)	42000
$-\Delta H_{N_2}$ (J/mol)	18000

Table 4.3 Bed geometry and adsorbent properties Case 2 [12]

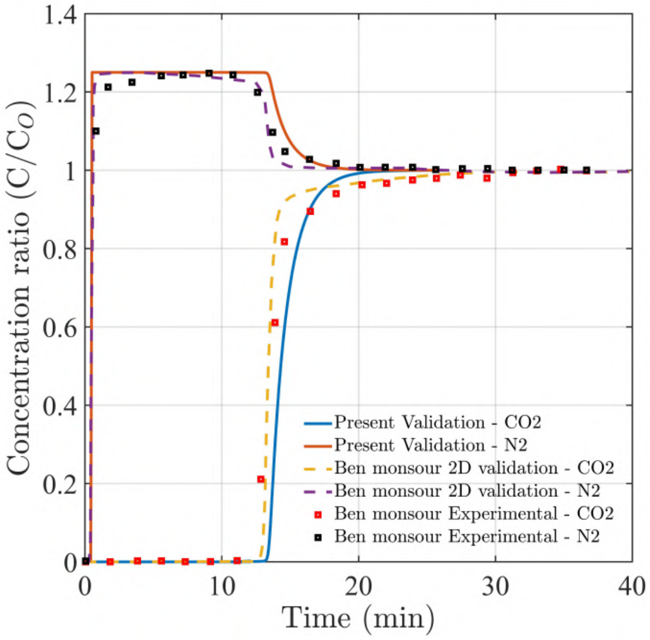

Fig. 4.4 Validation of breakthrough curves for case 2 [12]

4.3.3 Case 3

The third validation case is similar to the second one, except that the bed is assumed to be adiabatic. All data on the adsorption isotherms and the bed geometry are listed in the Table 4.4[25]. The breakthrough curves of the present simulations are compared with that of Dantas et al. [25] in Fig. 4.5.

Properties	**Value**
Bed Length, L (m)	0.171
Bed diameter, D (m)	0.022
Bed Wall thickness (m)	0.0015 m
Particle density ρ_p (Kg/m^3)	1138
Adsorbent particle size, d_p (m)	0.0038
Bed porosity ε	0.52
CO_2 inlet molar fraction x_{CO_2}	0.2
N_2 inlet molar fraction x_{N_2}	0.8
CO_2 adsorption time constant coefficient K_{L,CO_2} (1/sec)	0.032
N_2 adsorption time constant coefficient K_{L,N_2} (1/sec)	0.128
CO_2 species q_m (mmol/kg)	10.05
N_2 species q_m (mmol/kg)	9.74
K_{o,CO_2} (1/Pa)	7.62e-10
K_{o,N_2} (1/Pa)	6.91e-10
n_{CO_2}	0.678
n_{N_2}	0.518
$-\Delta H_{CO_2}$ (J/mol)	21840
$-\Delta H_{N_2}$ (J/mol)	16310

Table 4.4 Bed geometry and adsorbent properties for case 3 [25]

The figure shows a good match between the present numerical simulations and the experimental data though the numerical simulation results are not exactly identical. Once again, the reason for this difference can be attributed to the different choices of sub-models between the two works.

With the three validation cases thus considered, we now proceed to model the full PSA design developed in the current work.

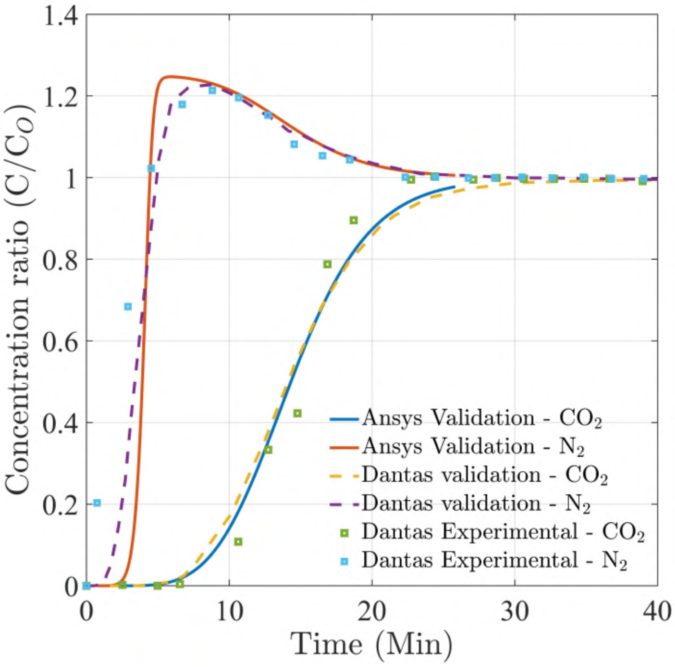

Fig. 4.5 Validation of breakthrough curves for case 3 [25]

4.4 Simulations of the full PSA plant

The essential ideas behind the present numerical simulation effort are to a) mimic the experimental results obtained from our device, b) provide better understanding of the intrinsic operation of the device, and c) provide a numerical design tool for optimization and further development of the device. In this regard, we consider the following assumptions.

- The ideal gas law is considered.
- Darcy's law provides a description of the adsorbent bed's bulk gas flow.
- The porous media in the adsorbent tank is assumed to be homogeneous.
- The species oxygen and argon are assumed to have a similar isotherm constant and considered to be a single species[95].
- Feed is a combination of nitrogen and oxygen in the proportion 78:22.
- Constant gas viscosity is assumed.

Considering these assumptions, we now look at how an optimum mesh can be arrived at for the current set of computations.

4.4.1 Mesh Independent study of single cylinder

The phenomena of primary interest here are the process of adsorption/desorption that results in oxygen concentration at the system's outlet. Hence, the current focus is to arrive at a mesh configuration that, upon further refinement, does not significantly alter the results obtained. In other words, we are looking to arrive at the optimum mesh density for the current set of computations. While one would desire a fine mesh to conserve different quantities of interest sufficiently, it may demand more memory and compute time. On the other hand, a coarser mesh might be inefficient in capturing the desired flow physics. The task of arriving at the optimum was achieved by considering the adsorption and flow processes in a single cylinder. Note that the flow profile in a pipe with tightly packed porous media is often top-hat. Hence, carrying out mesh refinement near the wall region would generally suffice. However, for the current problem with volumetric adsorption/desorption, it becomes essential to have a sufficient number of mesh points in the pipe's core region as well.

In the current work, the mesh was constructed using the mesh generation package ICEM-CFD. The length of the adsorbent tank is 930mm, and the diameter is 168.3mm. The length of the inlet and outlet pipes are 200mm and 50mm, respectively (Fig. 4.6).

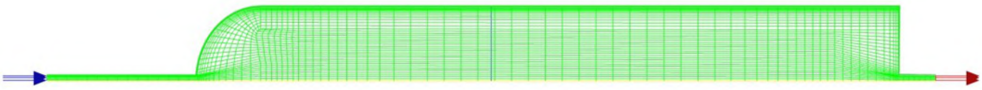

Fig. 4.6 Axisymmetric geometry for grid independence study

Note that the inlet and outlet pipes are clean regions, whereas the cylindrical column is a porous media. Also, the present analysis simplifies the whole domain into an axisymmetric configuration. Hence, the present mesh independence study has been performed with similar considerations. We have utilised different grids with and without the boundary layer mesh, and the overall mesh count was varied between 1000 and 6000 cells with an increment of 1000 cells. The properties of nitrogen, oxygen, bed porosity and boundary conditions are listed in Table 4.5 [60]. The Langmuir isotherm was used to model the adsorption process for the analysis. The adsorption isotherm parameters are listed in the Table 4.6 [60]

The velocity profiles at the mid-section of the zeolite column, $\frac{x}{L} = 0.5$, have been plotted in Fig. 4.7 and Fig. 4.8 for different mesh elements. Here, x is the distance measured from the inlet (590mm), and L is the total length of the adsorbent cylinder. It can be observed that the mesh configuration with 1000 cells underpredicts the velocity peak quite significantly. As we increase the mesh count, the pattern converges to a specific profile beyond 5000 cells. Interestingly, this convergence was observed as early as 3000 mesh count when the boundary layer mesh was utilized. Thus, to reduce the computational cost and effort, 3000

Mass Diffusivity of mixture (m^2/s)	2.88e-5
Species - 1 N_2 properties	
Specific Heat C_P, (J/Kg-K)	Piecewise polynomial $(-0.0011T^2 + 0.42T + 979.04)$[7]
Thermal conductivity K, (W/m-K)	0.0242
Viscosity μ, (Kg/m-s)	1.919e-5
Molecular weight (kg/mol)	28.0134
Species - 2 O_2 properties	
Specific Heat C_P, (J/Kg-K)	Piecewise polynomial $(-0.00015T^2 + 0.3T + 834.83)$[7]
Thermal conductivity K, (W/m-K)	0.0246
Viscosity μ, (Kg/m-s)	1.919e-5
Molecular weight (kg/mol)	31.998
Porous Media Formulation	
Viscous resistance (inverse permeability) $(1/m^2)$	199720555.6
Inertial resistance (1/m)	12944
Bed Porosity	0.46
Solid material	zeolite
Zeolite properties	
Density (Kg/m^3)	1170
Specific heat (J/Kg-K)	1138
Thermal conductivity (W/m-K)	0.13
Inlet Boundary condition	
Inlet gauge pressure (Pa)	606375
Inlet temperature (K)	300
Inlet nitrogen molar fraction	0.78
Inlet oxygen molar fraction	0.22
Outlet Boundary condition	
Outlet gauge pressure (Pa)	303975
Outlet temperature (K)	300
Wall condition (Convection thermal condition)	
Heat transfer coefficient $(W/m^2\text{-}K)$	8

Table 4.5 Parameters and boundary conditions for the grid independence study

elements with boundary layer mesh have been considered for our analysis of the axisymmetric representation of the complete PSA plant.

In the following section, we discuss the geometrical transformation of the complete PSA plant into an axisymmetric model and the implementation of valve sequencing via dynamics changes in the boundary conditions.

Species-1 Nitrogen	
Q_m (mmol/g)	7.2
b_O (1/Pa)	2.154e-9
ΔH_N (J/mol)	-18367.75
Species-2 Oxygen	
Q_m (mmol/g)	2.47
b_O (1/Pa)	3.253e-9
ΔH_N (J/mol)	-12803.04

Table 4.6 Isotherm constant [60]

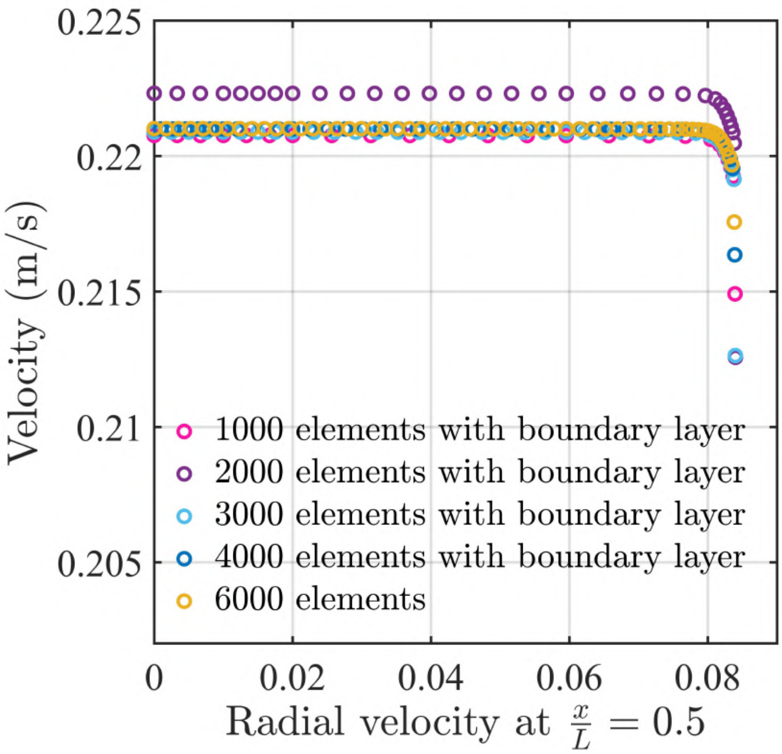

Fig. 4.7 Axial velocity at $\frac{x}{L} = 0.5$ for boundary layer mesh

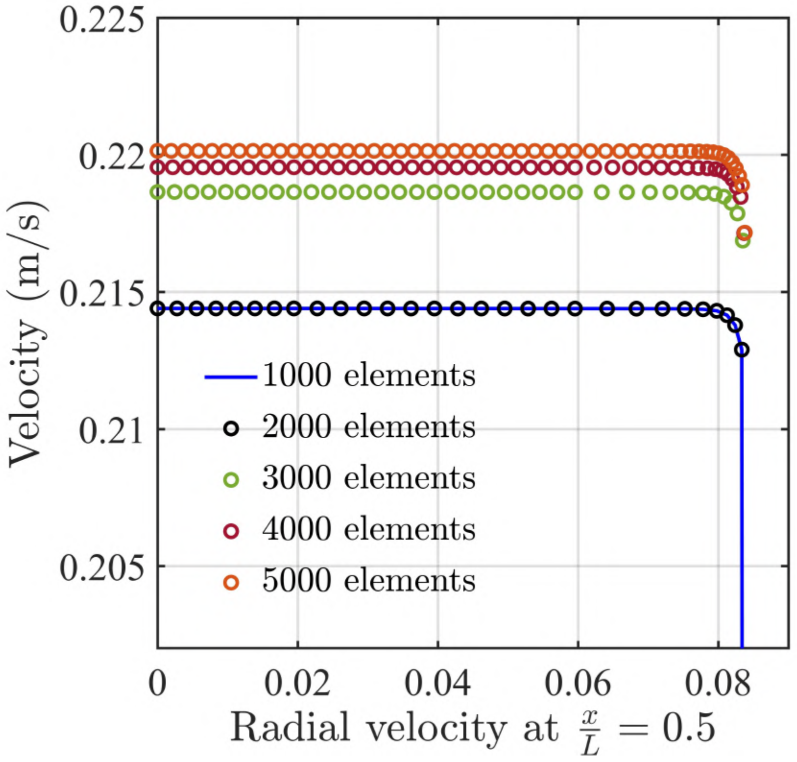

Fig. 4.8 Axial velocity at $\frac{x}{L} = 0.5$ for without boundary layer mesh

4.4.2 PSA plant modelling

In order to save on the computational effort, the complete PSA plant is transformed into an axisymmetric model, as shown in 4.9. The geometry is subdivided into sections I, II, and III. Sections I and II are the zeolite cylinders, which are mirror images of each other. Section III is the oxygen storage tank. The zeolite tank is a Schedule 5 SS pipe with an inner radius of 81.34mm, a wall thickness of 2.77 mm, and a length of 922 mm. A 2:1 ellipsoidal dish end has been attached at the bottom. The oxygen storage tank radius is a schedule 5 pipe with a radius of 33.49mm, a thickness of 3mm, and a length of 568mm with a 2:1 ellipsoidal dish end attached at both ends. The two zeolite tanks are 18 liters of volume each, while the volume of the oxygen storage tank is 2.4 liters.

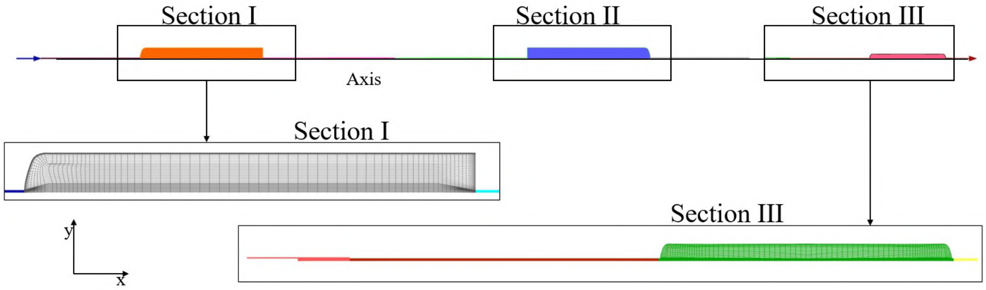

Fig. 4.9 Computational model and sectional view of axisymmetric geometry

As mentioned before, the solenoid valve operation is mimicked here by changing the boundary conditions at the cylinders' inlet and outlet. This will be discussed in the following sub-section.

Valve configuration and Zone nomenclature

In Fig. 4.10, different boundaries are marked with different colours and are given different names. Figure 4.10 shows the nomenclature of appropriate boundaries in the domain. In section I, the inlet/outlet for cylinder 1 is named Face 1. It serves as an inlet when cylinder 1 is being pressurised and, alternatively, as an outlet when it is being depressurised. Recall the PSA process explained in the previous chapter. Similarly, Face 4 is associated with cylinder 2 in section II. The interconnection between cylinder 1 and cylinder 2 is Face 5. Faces 21 and 31 are provided in cylinders 1 and 2, respectively, and they interface with Faces 22 and 32 of section III, corresponding to the oxygen storage tank. They will be linked appropriately based on the steps involved in the cycle.

When necessary, a conformal mesh mapping is performed to link the Faces 1 & 4, 21 & 22, and 31 & 32 using periodic boundary conditions in the FLUENT. The periodic boundary

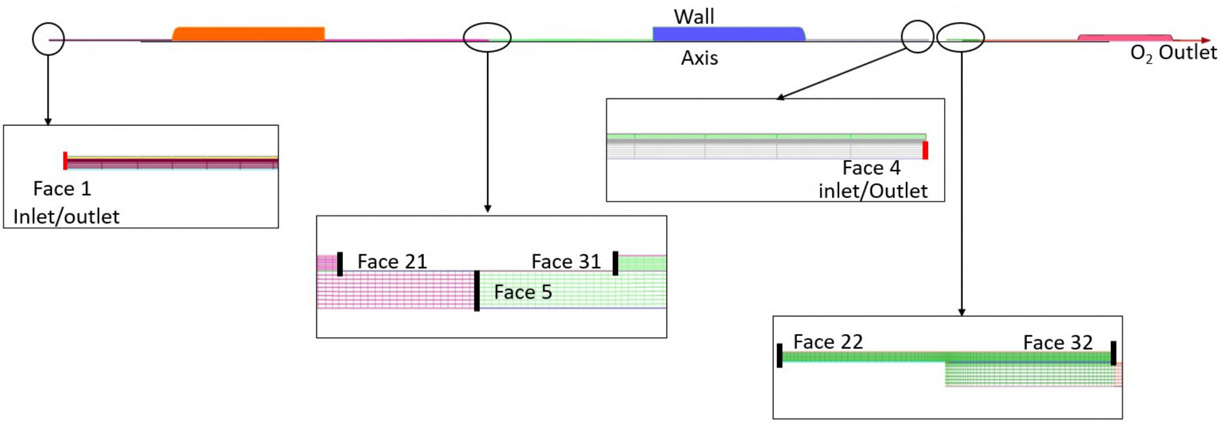

Fig. 4.10 Valve representation

condition allows for 1-to-1 mapping between the face pairs wherein the field variables are identical. In this regard, one must ensure that the faces are in proper pairs and they are physically identical. The translational type of periodic boundary conditions requires the two constituent faces to be parallel to each other so that a single translation transformation can be used by providing an offset. Note that the face pairs mentioned above are altered between interface and wall conditions to mimic the solenoid valve configurations as in the experiments. The complete summary of the boundary condition (valve) sequencing is listed in Table 4.7.

	Face 1	**Face 21**	**Face 22**	**Face 31**	**Face 32**	**Face 4**	**Face 5**
Pres-1	Inlet	Interface with 22	Interface with 21	Wall	Wall	Outlet	Wall
Pur-1	Inlet	Interface with 22	Interface with 21	Wall	Wall	Outlet	Interior
Equ-1	Interface with 4	Wall	Wall	Wall	Wall	Interface with 1	Interior
Pres-2	Outlet	Wall	Wall	Interface with 32	Interface with 31	Inlet	Wall
Pur-2	Outlet	Wall	Wall	Interface with 32	Interface with 31	Inlet	Interior
Equ-2	Interface with 4	Wall	Wall	Wall	Wall	Interface with 1	Interior

Table 4.7 Valve Sequencing in terms of boundary conditions

We now follow through the sequence of steps followed in the experiments and see how these steps in mimicked in the simulations.

- **Pressurization 1**: In this step, the boundary condition on Face 1 is set as a pressure inlet and Face 4 as a pressure outlet. Face 21 is interfaced with Face 22 via a mesh interface. The boundary conditions of Faces 31, 32, and 5 are set as walls. Air (containing 78% nitrogen, 22% oxygen) is fed from Face 1. The flow maintains continuity between Faces 21 and 22 and moves to the O_2 storage tank. Simultaneously, depressurization occurs at cylinder 2, where a pressure outlet boundary condition is implemented on Face 4.

- **Purge 1**: The flow continues to follow the designated path. In order to purge cylinder 2, the boundary condition of Face 5 is changed from wall to interior to allow some fraction of oxygen from cylinder 1 and O_2 storage tank to cylinder 2 for purging.

- **Equalization 1**: In order to obtain the pressure equalization step, Faces 1 and 4 are interconnected via mesh interface by changing the boundary condition to the interface, Face 5 retains the interior boundary conditions, and all the other faces are set as walls.

- **Pressurization 2** - This is the opposite of the Pressurization 1 step. Here, the boundary condition on Face 4 is set as a pressure inlet and Face 1 as a pressure outlet. Face 31 is interfaced with Face 32 via a mesh interface. The boundary conditions of Face 21, 22, and 5 are changed to the wall. The air is fed from valve 4. The flow is continuous between Faces 31 and 32 and moves to the O_2 storage tank as before. Depressurization occurs in cylinder 1, where the Face 1 boundary condition is changed to a pressure outlet.

- **Purge 2** - All the face configurations are the same as the above, except that the boundary condition of Face 5 is changed from wall to interior so that the purging of cylinder 1 can happen by high purity mixture from cylinder 2 and O_2 storage tank.

- **Equalisation 2**: The configuration of faces is the same as those in the Equalization 1 step.

The different properties and boundary pressure values for the above different steps are listed in the Tables 4.8 and 4.9, respectively. All the gas parameters relevant to the kinetic theory were obtained from FLUENT manual [33] and Hirschfelder et al. [38]. The viscous and inertial resistances have been calculated using Eqs. (4.12) and (4.13), respectively. With these details in mind, we now proceed to the methodology of simulations in the next section.

Species - 2 O_2 properties	
Specific Heat C_P, (J/Kg-K)	Kinetic theory ([33], [38])
Thermal conductivity K, (W/m-K)	kinetic theory ([33], [38])
Viscosity μ, (Kg/m-s)	kinetic theory ([33], [38])
Molecular weight (kg/mol)	31.998
L-J characteristic length (angstrom)	3.458
L-J energy parameter (k)	107.4
Degree of freedom	5
Species - 2 N_2 properties	
Specific Heat C_P, (J/Kg-K)	Kinetic theory ([33], [38])
Thermal conductivity K, (W/m-K)	kinetic theory ([33], [38])
Viscosity μ, (Kg/m-s)	kinetic theory ([33], [38])
Molecular weight (kg/mol)	28.0134
L-J characteristic length (angstrom)	3.621
L-J energy parameter (k)	97.53
Degree of freedom	5
Porous Media Formulation	
Viscous resistance (inverse permeability) (1/m^2)	565545733.6
Inertial resistance (1/m)	31100
Fluid Porosity	0.363 [28]
Solid material	zeolite
Zeolite properties	
Density (Kg/m^3)	1133.43
Specific heat (J/Kg-K)	1138
Thermal conductivity (W/m-K)	0.08[20]

Table 4.8 Fluent settings for axisymmetric geometry

Boundary condition - pressurization 1	
Valve 1 (pressure inlet)	600000 Pa
Valve 4 (Pressure outlet)	0 Pa
Valve 21 and Valve 22	Interface
Boundary condition - Purge 1	
Valve 1 (pressure inlet)	600000 Pa
Valve 4 (Pressure outlet)	0 Pa
Valve 21 and Valve 22	Interface - valve open
Valve 5	Interior - valve open
Boundary condition - Equalisation 1	
Valve 1 and Valve 4	Interface - valve open
Valve 5	interior - valve open
Boundary condition - pressurization 2	
Valve 4 (pressure inlet)	600000 Pa
Valve 1 (Pressure outlet)	0 Pa
Valve 31 and Valve 32	Interface - valve open
Boundary condition - Purge 2	
Valve 4 (pressure inlet)	600000 Pa
Valve 1 (Pressure outlet)	0 Pa
Valve 31 and Valve 32	Interface - valve open
Valve 5	Interior - valve open
Boundary condition - Equalisation 2	
Valve 1 and Valve 4	Interface - valve open
Valve 5	interior - valve open
Wall condition (Convection thermal condition)	
Heat transfer coefficient (W/m^2-K)	8

Table 4.9 Boundary conditions for Valve sequencing

4.5 Numerical modelling of PSA plant and results

4.5.1 Solution methodology

In the present set of simulations for the complete PSA plant, different changes in the boundary conditions have been incorporated automatically via a journal file written in accordance with the FLUENT software. Here, each simulation was performed for 40 complete cycles to make the resulting behavior cyclically steady. Table 4.9 lists the boundary conditions for different steps. In the numerical modelling, the inlet pressure was not set as 6 bar, as in the experiments, but was set to the peak pressure value observed in the experiments. This was done to account for the fact that the experiments were carried out with a 5hp compressor and a 220-liter buffer tank. Additionally, a dryer was used to remove moisture from the feed air, bringing its own purge losses. Hence, the overall system acts as a finite source and does not allow the peak pressure to reach the set value of 6 bar. In the present work, all the numerical simulations have been performed for the oxygen delivery rate of 41.69 sLPM. This corresponds to a value of 0.0009038 kg/s at the outlet of the oxygen storage tank.

In reality, the molar percentage of O_2, Ar, and N_2 are about 0.21, 0.01, and 0.78, respectively. However, note that the adsorbent (13X) has a similar propensity for adsorbing oxygen and argon; hence, we combine these two species into one pseudo-species[95] and treat air as a mixture of two species, O_2 and N_2, having molar fraction ratio 22:78. While extracting the information, a factor of $\left(\frac{21}{22}\right)$ is multiplied to get the oxygen purity individually.

As the first test case for simulation, we consider the scenario where the pressurization, purge, and equalisation times are 26, 2, and 4 seconds, respectively. Here, Langmuir-Freundlich isotherm is used to model the adsorption process in the complete PSA plant. Figure 4.11 shows the pressure profile for both cylinders. There is a notable difference between these profiles and the experimental data presented in Fig. 3.19. Unlike the experimental curves, which do not saturate completely during the pressurisation steps, the simulation profiles quickly saturate to the set pressure. This difference can be attributed to the insufficient feed air source in the experimental setup, whereas the source is of infinite strength in the numerical simulations. The transient evolution of oxygen purity from the simulation is shown in fig 4.12, which indicates a peak performance of approximately 91%. It is observed from the graph that after 1200 seconds, the system reaches a cyclic steady state.

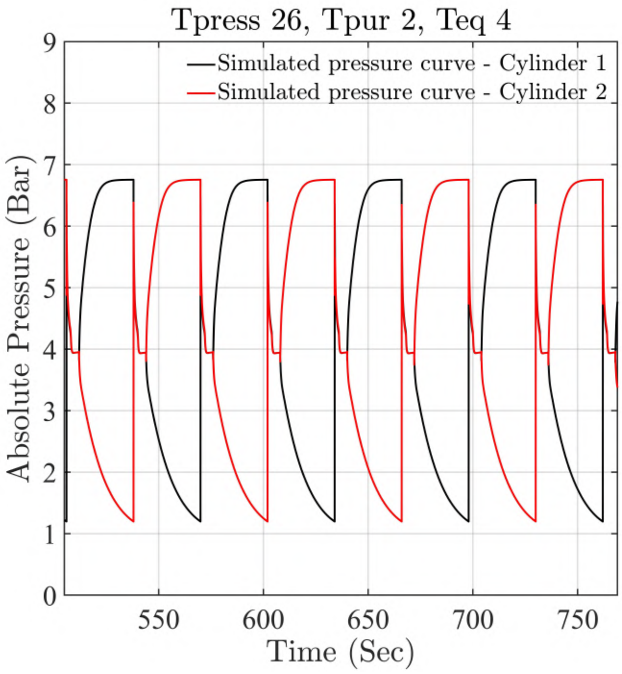

Fig. 4.11 Simulated pressure curve for T_{Press} = 26, T_{Purge} = 2, T_{Eq} = 4

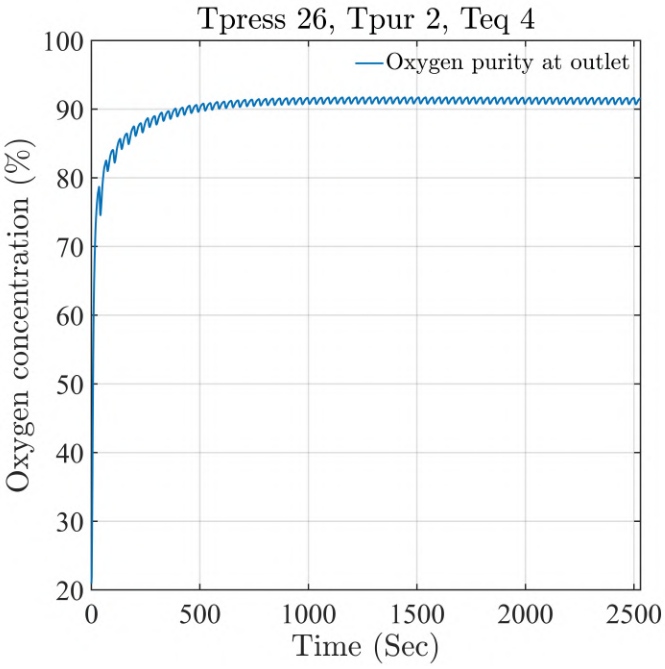

Fig. 4.12 Simulated Oxygen purity at outlet for T_{Press} = 26, T_{Purge} = 2, T_{Eq} = 4

4.5.2 Revisiting the adsorption isotherm models

While reviewing the different adsorption isotherm models and the associated constants in the literature, one can observe a notable inconsistency and lack of uniformity in the different models presented. Since it was difficult to single out the most appropriate version from the available variants, we have conducted simulations using some notable models and compared them against the experimental data here. One such model is the Langmuir-Freundlich isotherm which has different published versions. The first version of the Langmuir-Freundlich isotherm is given as [42]

$$q_1^* = \frac{q_{m1} b_1 P_1^{n1}}{1 + b_1 P_1^{n1} + b_2 P_2^{n2}} \tag{4.31}$$

$$q_2^* = \frac{q_{m2} b_2 P_2^{n2}}{1 + b_1 P_1^{n1} + b_2 P_2^{n2}} \tag{4.32}$$

where $q_m = K_1 + K_2 T$, $b_i = b_{oi} exp\left(\frac{K_4}{T}\right)$, and $n_i = K_5 + \frac{K_6}{T}$.

The second version of the Langmuir-Freundlich isotherm (b_n corrected) is expressed as[56]:

$$q_1^* = \frac{q_{m1} b_1^{n1} P_1^{n1}}{1 + b_1^{n1} P_1^{n1} + b_2^{n1} P_2^{n2}} \tag{4.33}$$

$$q_2^* = \frac{q_{m2} b_2^{n2} P_2^{n2}}{1 + b_1^{n1} P_1^{n1} + b_2^{n2} P_2^{n2}} \tag{4.34}$$

where $q_m = K_1 + K_2 T$, $b_i = b_{oi} exp\left(\frac{K_4}{T}\right)$, and $n_i = K_5 + \frac{K_6}{T}$.

Constant	N_2	O_2
K_1x10^3 (mol/g)	12.52	6.705
K_2x10^5 (mol/g-K)	-1.785	-1.435
K_3x10^5 (1/atm) [42]	2.154	3.253
K_3x10^4 (1/atm) [60], [45])	2.154	3.253
K_4 (K) (	2333	1428
K_5 (-)	1.666	-0.3169
K_6 (K)	-245.2	387.8
Heat of adsorption, Q (cal/mol)	4390	3060
LDF constant (1/sec)	0.197	0.62

Table 4.10 Different constants for LF adsorption isotherm

The various constants utilised for the model are listed in Table 4.10. The values of q_m, b_i have been taken from the articles of Kakavandi et al. ([45], Jee et al. [42], and Mofarahi and Shokroo [60]). As highlighted in the Table 4.10, one may note that different literature have used different values for K_3. Once again, it was challenging to speculate the correct data. Hence, we have carried out simulations using both these values. In total, we have performed simulations using the following four models.

- Langmuir isotherm with K_3 of the order 10^{-5}
- Langmuir-Freundlich isotherm with K_3 of the order 10^{-5}
- Langmuir-Freundlich isotherm with K_3 of the order 10^{-4}
- Langmuir-Freundlich isotherm (b_n corrected) with K_3 of the order 10^{-5}

In the next section, we compare the performance of the above adsorption models with the experimental results for the different pressurization times (22 s, 26 s, and 30 s). The delivery flow rate was maintained at 41.69 sLPM while the purge and equalisation times were kept as 2 s and 4 s, respectively.

4.5.3 Simulations to understand the variation in pressurization time

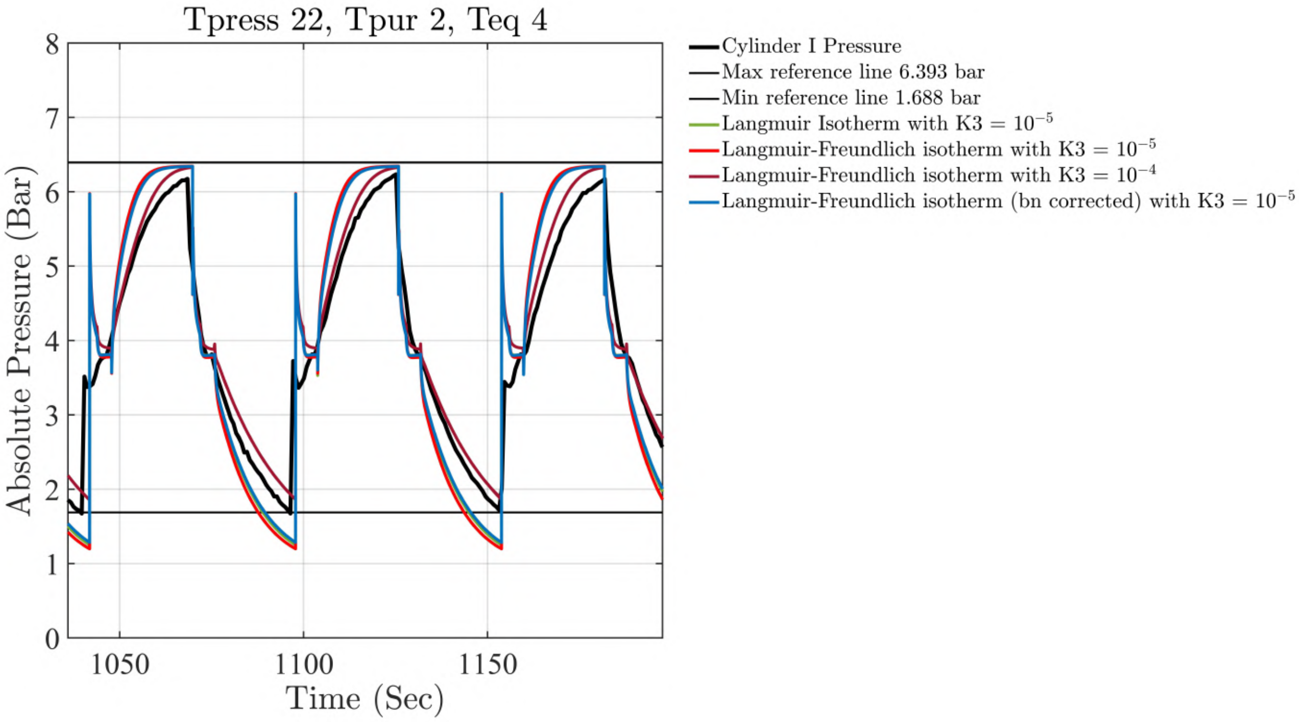

Fig. 4.13 Comparison of cylinder 1 pressure. t_{press} = 22 s

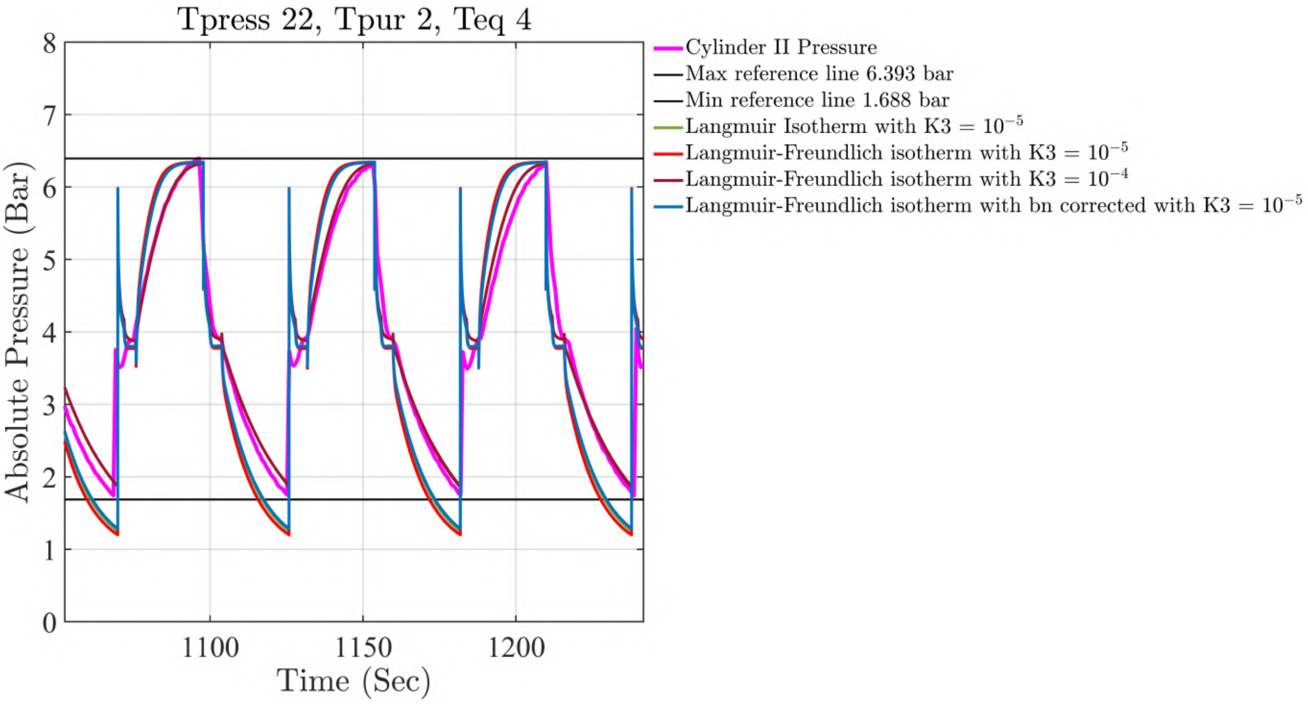

Fig. 4.14 Comparison of cylinder 2 pressure. t_{press} = 22 s

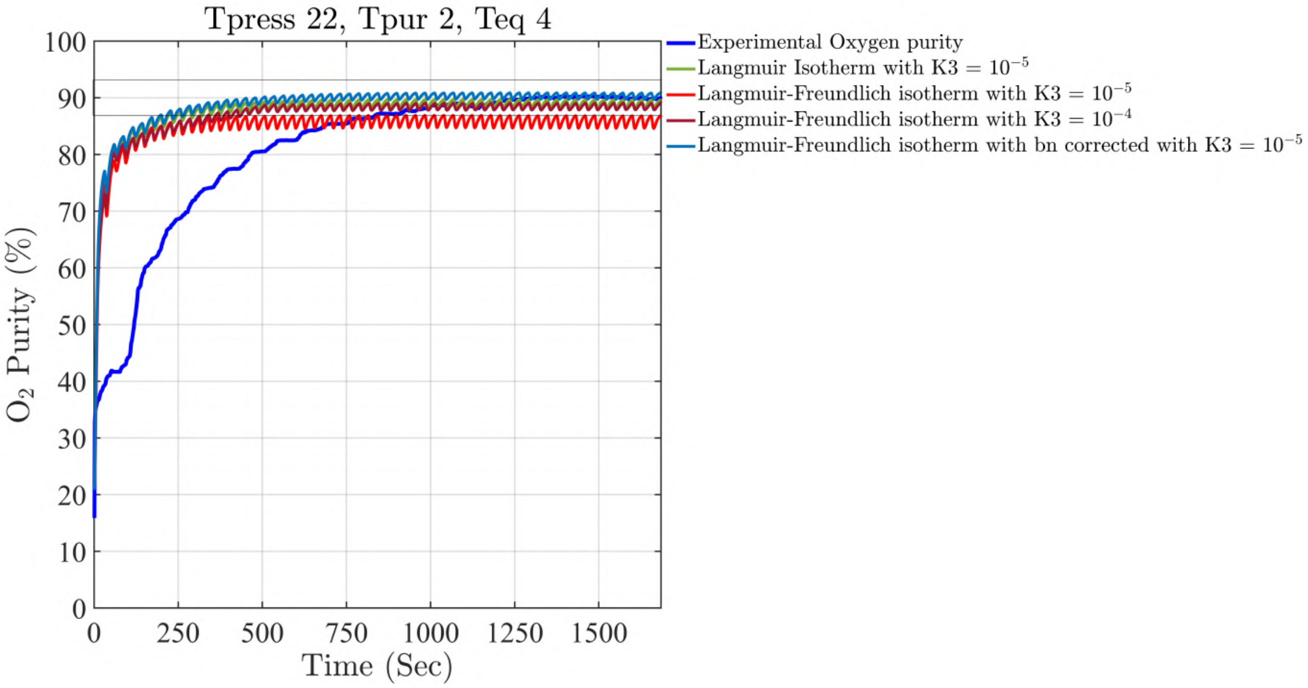

Fig. 4.15 Comparison of transient evolution of oxygen purity. t_{press} = 22 s

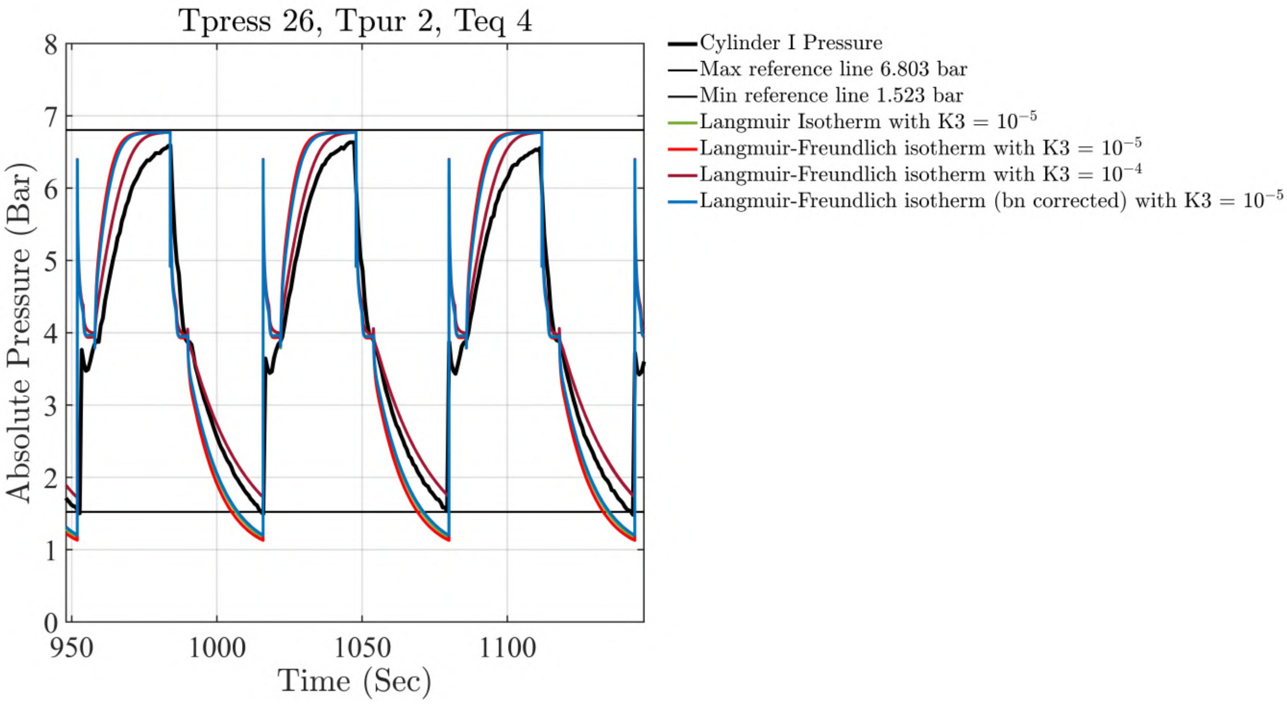

Fig. 4.16 Comparison of cylinder 1 pressure. t_{press} = 26 s

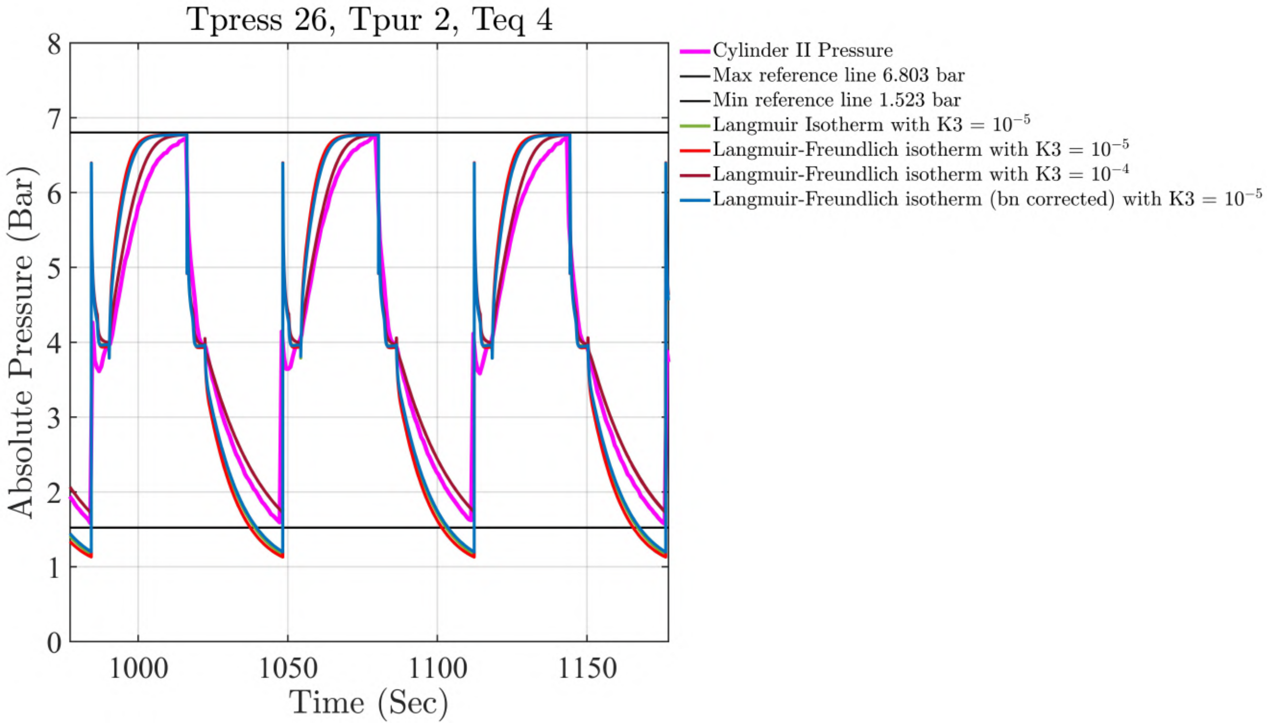

Fig. 4.17 Comparison of cylinder 2 pressure. t_{press} = 26 s

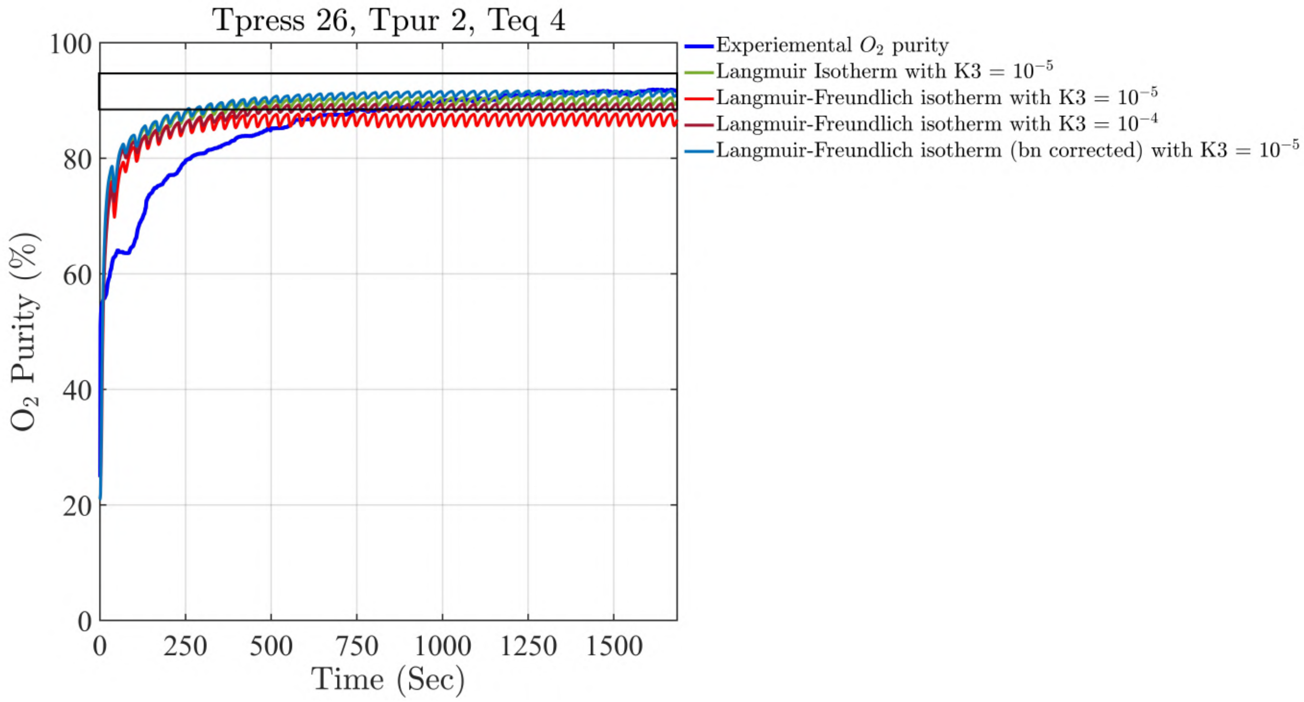

Fig. 4.18 Comparison of oxygen purity. t_{press} = 26 s

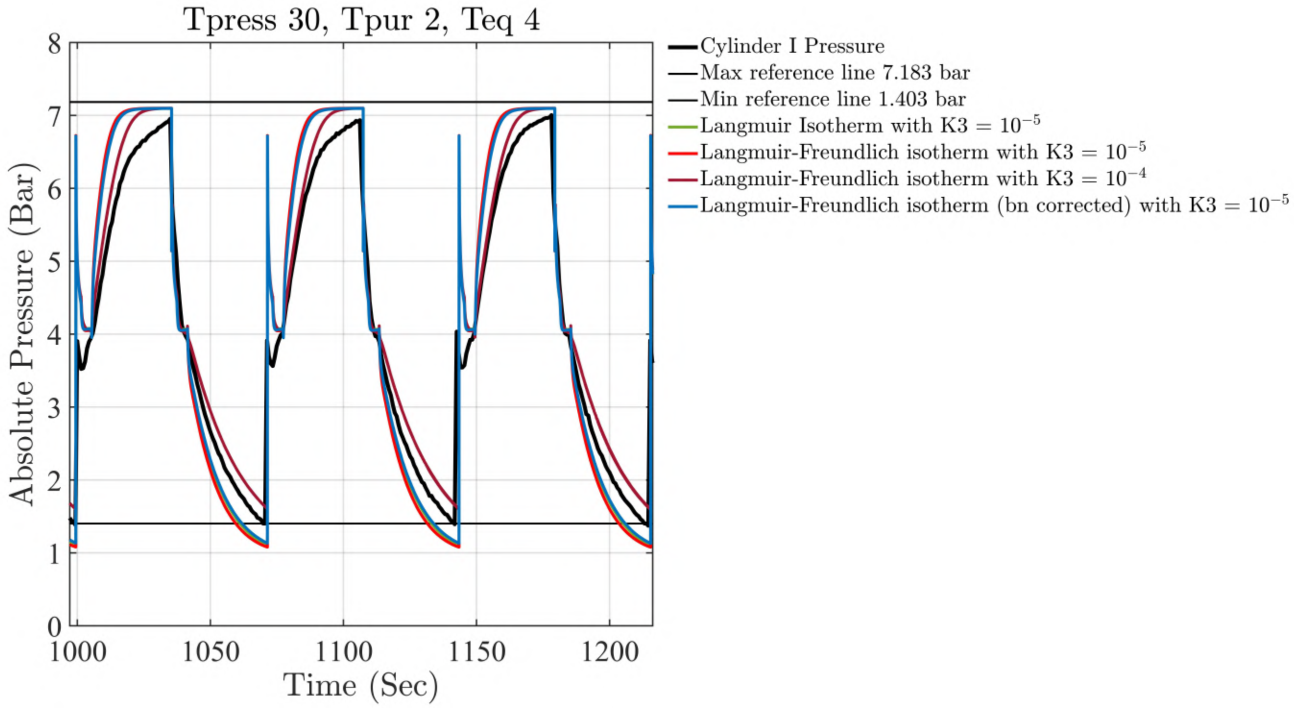

Fig. 4.19 Comparison of cylinder 1 pressure. t_{press} = 30 s

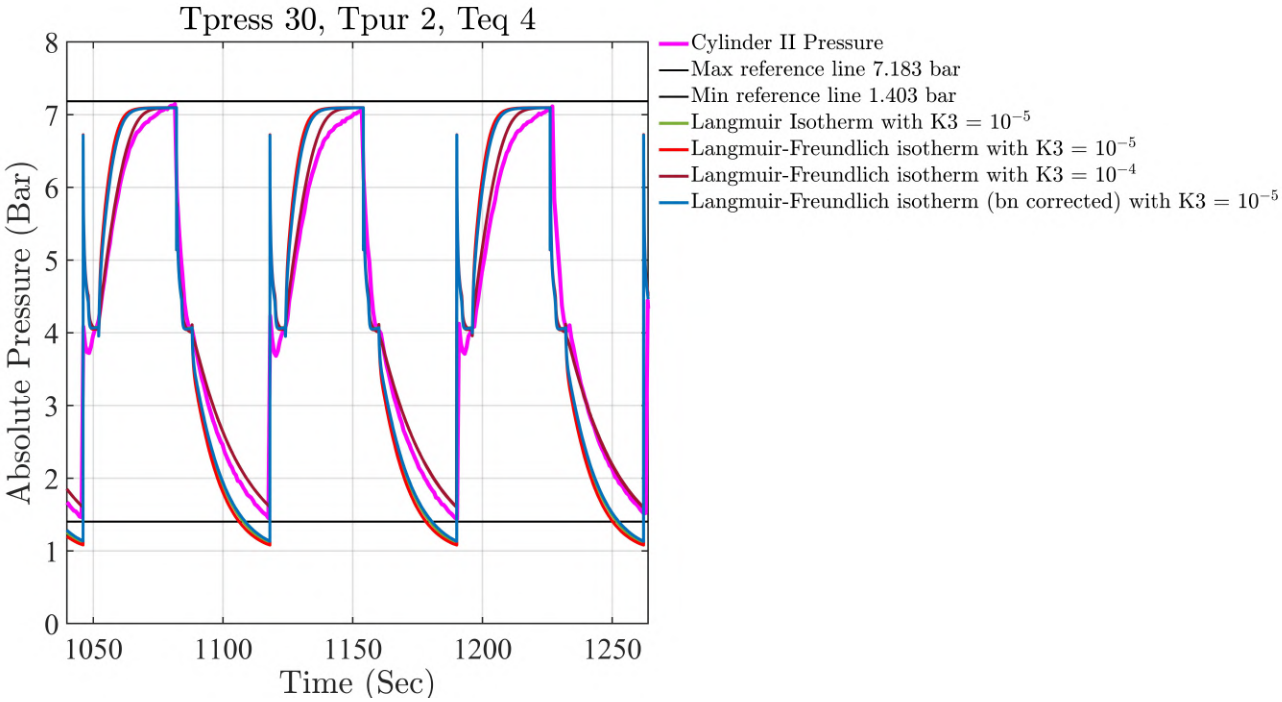

Fig. 4.20 Comparison of cylinder 2 pressure. t_{press} = 30 s

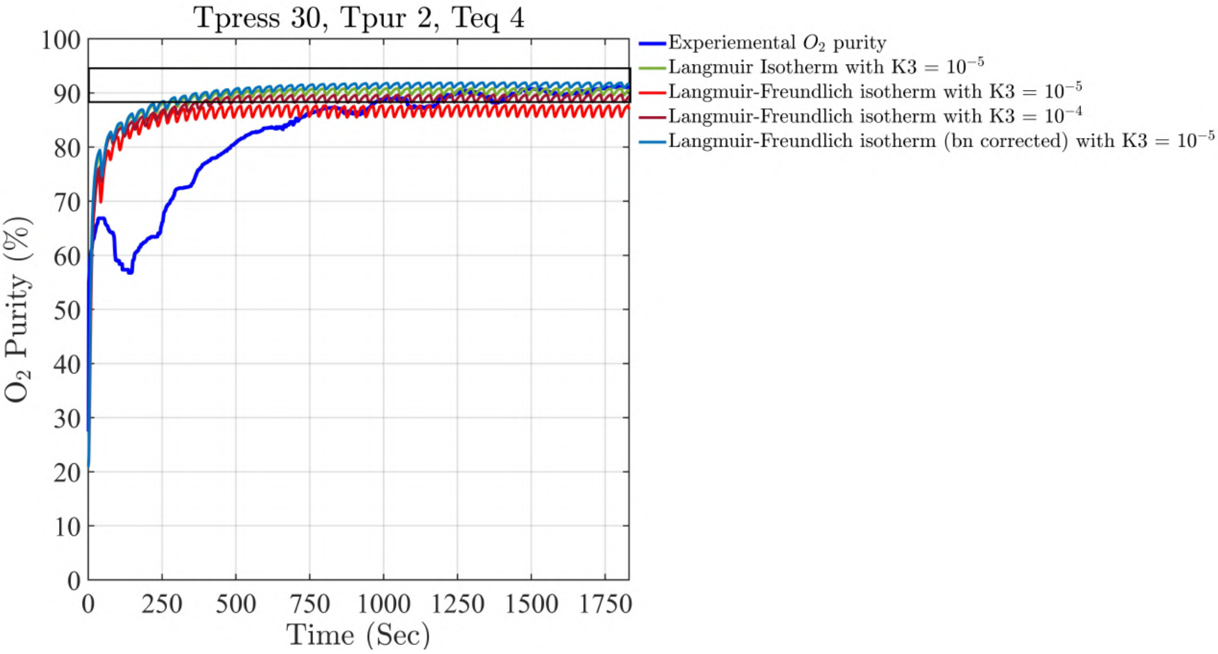

Fig. 4.21 Comparison of oxygen purity curve. t_{press} = 30 s

The process of comparing the experimental results with the different adsorption isotherm models is now begun with the simulation of the case wherein t_{press} = 22 s, t_{pur} = 2 s, and

t_{equ} = 4 s. Figure 4.13 and figure 4.14 shows the comparison of the pressure curves for zeolite cylinder 1 and 2 obtained after the system has attained a cyclic steady state. Here, the reference lines at the top and bottom show the average maximum and minimum pressure values obtained experimentally. By comparing these figures, one can quickly observe the difference in experimental peak pressures of the two cylinders. Such a difference manifests due to the minor geometric asymmetry in the two zeolite columns. One can also observe that for both the cylinders, the Langmuir-Freundlich isotherm with $K_3 = 10^{-4}$ follows the experimental pressure curves more closely as compared to the other isotherm models, namely, Langmuir isotherm with $K_3 = 10^{-5}$, Langmuir-Freundlich isotherm with $K_3 = 10^{-5}$, and Langmuir-Freundlich (b_n corrected) with $K_3 = 10^{-5}$. In fact, the latter models almost overlap each other. The reason for this behaviour can be linked to the strength of adsorption in the models. $K_3 = 10^{-4}$ manifests stronger adsorption, and it takes a while for the pressure to attain saturation since the sink strength is significant. On the other hand, $K_3 = 10^{-5}$ accounts for weaker adsorption; hence, the pressure in the cylinders quickly rises and attains saturation. One can use the same arguments to corroborate the observations at the valley of the pressure curves where the system is essentially undergoing desorption. It is evident that the models with $K_3 = 10^{-5}$ manifest pressure values lower than the experimental data, whereas the lowermost pressure attained by $K_3 = 10^{-4}$ model is slightly higher than the experimental value. These behaviours are directly linked to the total quantity of gas adsorbed in the zeolites. The former models with low sink strength result in lower cumulative gas adsorption in the zeolites, and during the desorption process, the quantity of gas released from zeolites is small. Hence, the pressure quickly falls down in the cylinders. Whereas the latter model, with its reasonable adsorption, results in the slower decay of pressure in the cylinders. Figure 4.15 compares the oxygen purity at the delivery side. The oxygen purity in the experimental data is greater than 90%. The two horizontal lines correspond to the experimental upper and lower limits of the oxygen purity from the device, i.e., the saturated experimental value and ±3%. In Fig. 4.15, there is a notable mismatch between the numerical and the experimental oxygen evolution curves. This could be due to the residual condition of the O_2 buffer tank before the experiments start. Thus, it is pertinent to compare the data only after a cyclic steady state is attained. From figure 4.15, it can be observed that the Langmuir-Freundlich model with $K_3 = 10^{-5}$ underpredicts the oxygen purity, while the rest of the three models are well within the error bar limit. In fact, the Langmuir-Freundlich (b_n corrected) model matches well with the experimental data.

In order to verify the consistency of the above observations, simulations are performed at other pressurisation times, such as 26 s and 30 s. Figures 4.16, 4.17, and 4.18 show the comparison of the pressure curves and oxygen purity for t_{press} = 26 s. The same comparisons have been carried out for t_{press} = 30 s in Figs. 4.19, 4.20, and 4.21. From these figures, we can reconfirm the observations made from the simulations of t_{press} = 22 s. Once again, the Langmuir-Freundlich isotherm with $K_3 = 10^{-4}$ follows the experimental pressure curves more closely than any other isotherm model and the Langmuir-Freundlich isotherm K_3=10^{-5} under predicts the oxygen purity. In contrast, the other three isotherm models are well placed within the experimental error bars.

To summarise, the numerical simulations involving different adsorption isotherm models reveal that the models, Langmuir-Freundlich (b_n corrected) with K_3=10^{-5}, Langmuir-Freundlich with K_3=10^{-5}, and Langmuir isotherm with K_3=10^{-5}, well predict the evolution of oxygen purity in the system. However, from the pressure data, the only reasonable model is the Langmuir-Freundlich with K_3=10^{-4}. Based on these, we only choose the Langmuir-Freundlich (b_n corrected) with K_3=10^{-5} and the Langmuir-Freundlich with K_3=10^{-4} for performing the next sets of simulation where the purge and equalisation times have been varied.

4.5.4 Variation of purge and equalization times

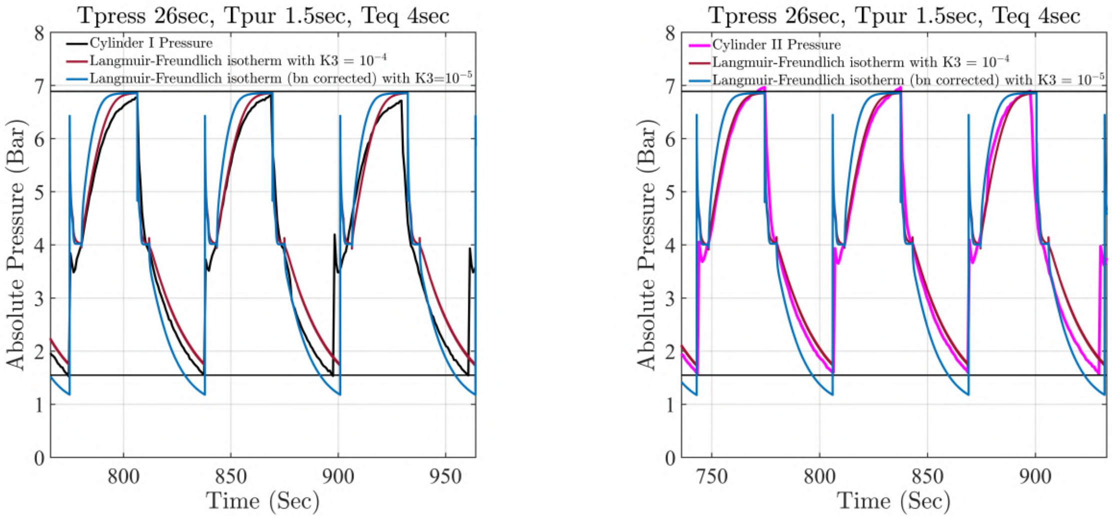

(a)

(b)

Fig. 4.22 Comparison of pressure curves for t_{pur} = 1.5 s (a) Pressure curves for cylinder 1 (b) Pressure curves for cylinder 2

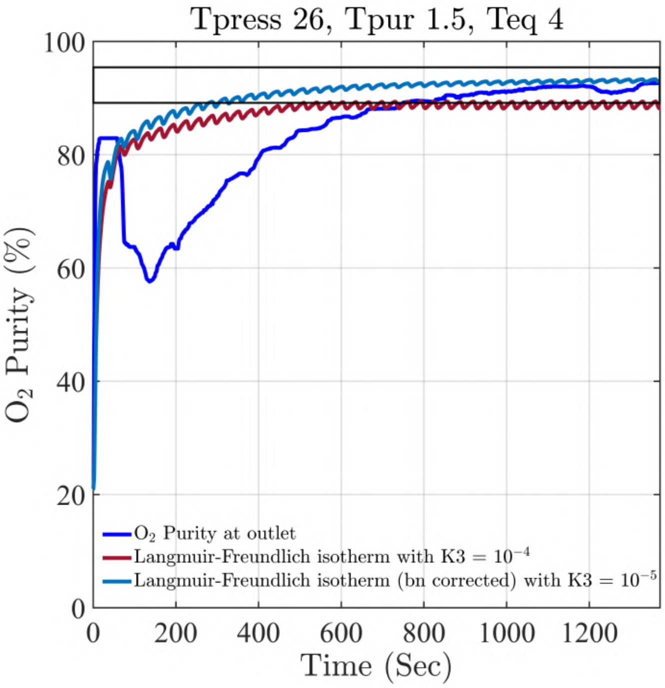

Fig. 4.23 Comparison of oxygen purity curve for t_{pur} = 1.5 s

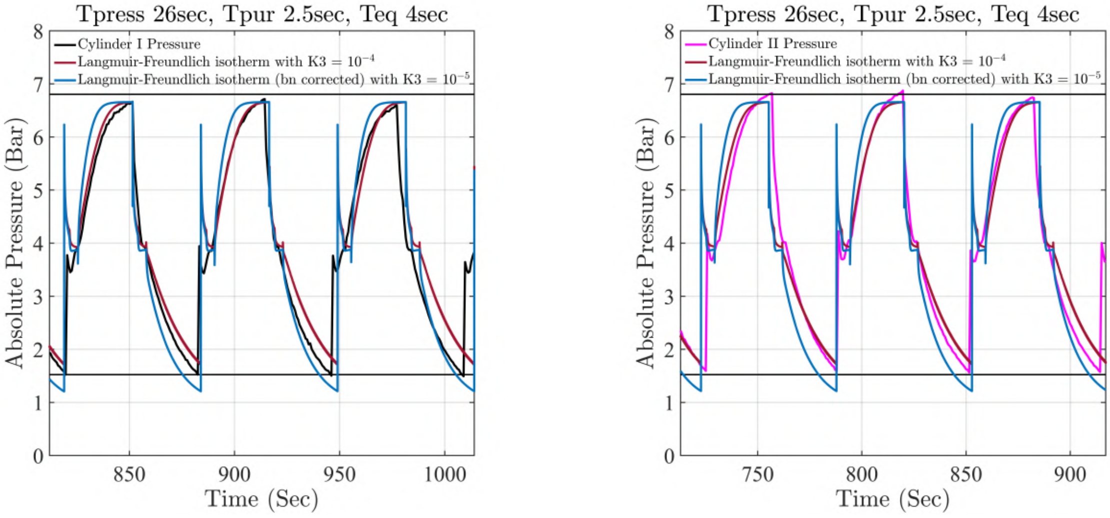

(a) (b)

Fig. 4.24 Comparison of pressure curves for t_{pur} = 2.5 s (a) Pressure curves for cylinder 1 (b) Pressure curves for cylinder 2

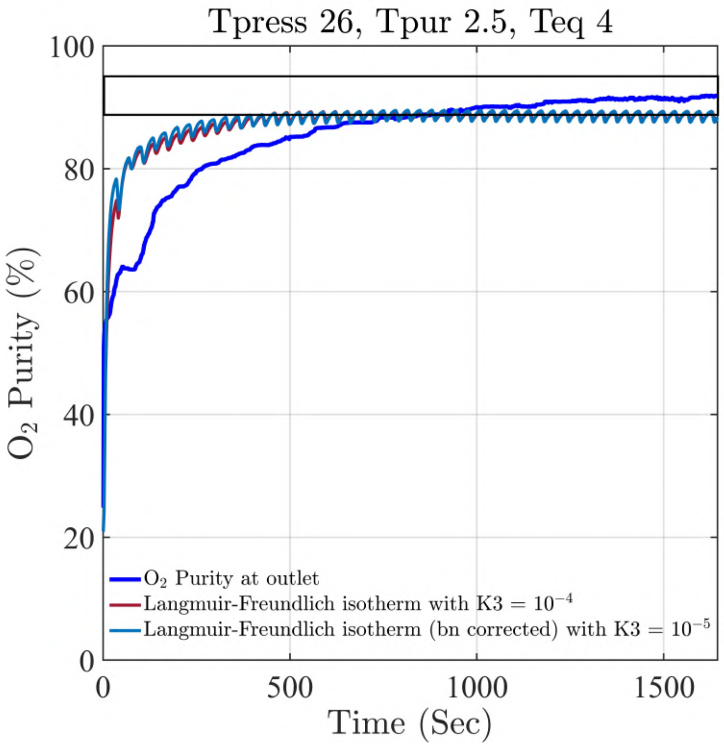

Fig. 4.25 Comparison of oxygen purity curve for t_{pur} = 1.5 s

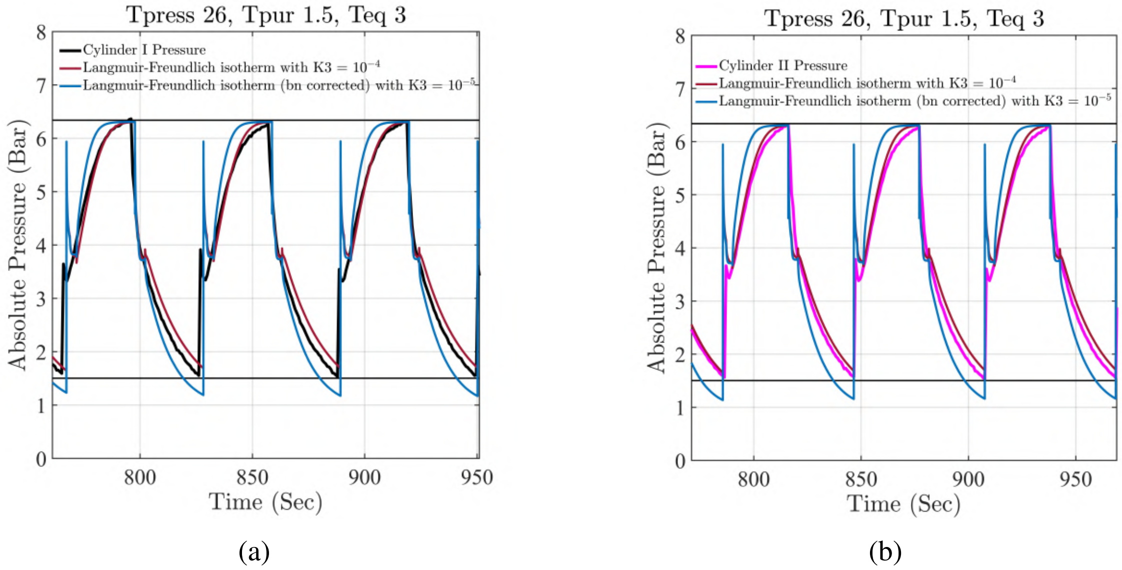

(a) (b)

Fig. 4.26 Comparison of pressure curves for t_{equ} = 3 s (a) Cylinder 1 (b) Cylinder 2

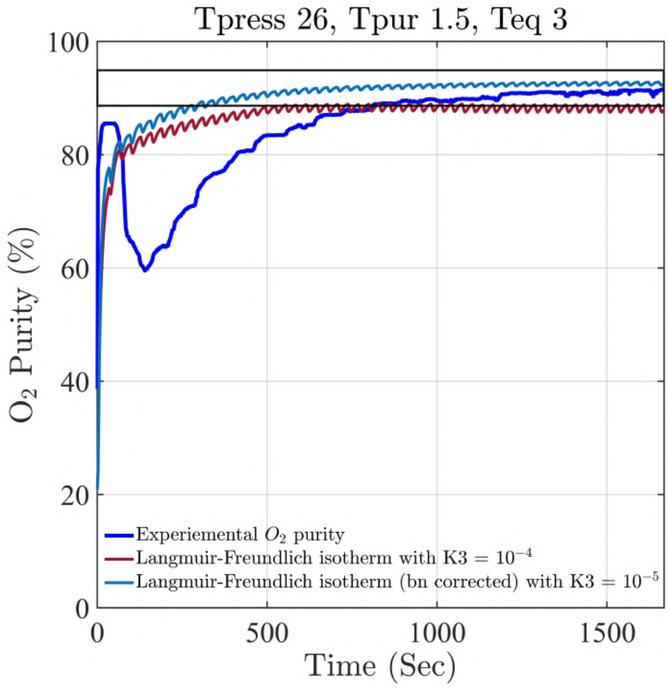

Fig. 4.27 Comparison of oxygen purity curve for t$_{equ}$ = 3 s

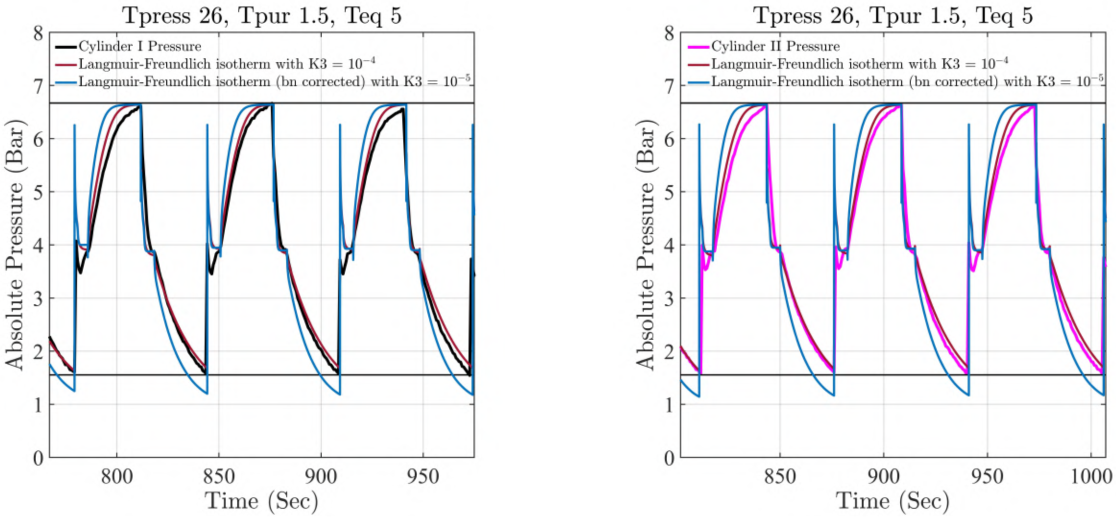

(a) (b)

Fig. 4.28 Comparison of pressure curves for t$_{equ}$ = 5 s (a) Cylinder 1 (b) Cylinder 2

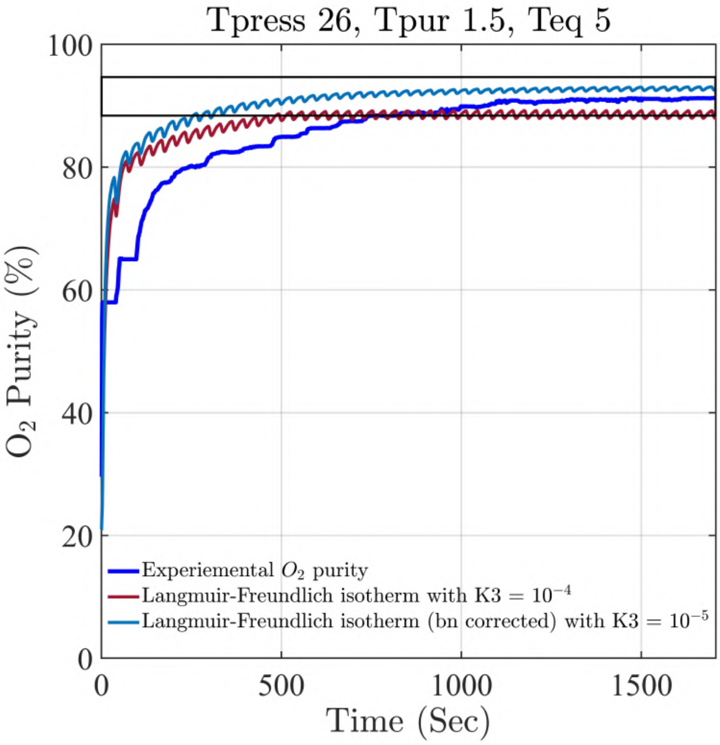

Fig. 4.29 Comparison of oxygen purity curve for t_{equ} = 5 s

We now perform simulations to see if we can mimic the experimental behaviour pertaining to the variation of purge and equalisation times, as shown in the previous chapter. The simulations presented here use the optimum pressurisation time of 26 s corresponding to the flow rate of 41.69 sLPM. Figures 4.22a, 4.22b, and 4.23 show the comparison of pressure curves for cylinder 1 and 2 and oxygen purity for a purge time of 1.5 s and an equalisation time of 4 s. As mentioned before, only two adsorption isotherm models, namely, the Langmuir-Freundlich model with $K_3=10^{-4}$ and the Langmuir-Freundlich model (b_n corrected) with $K_3=10^{-5}$, has been used for the current analysis. The same analysis has been repeated for the purge time of 2.5 s, and the comparison curves are shown in Figs. 4.24a, 4.24b, and 4.25, respectively. From the figures, it is evident that the numerical simulations can properly account for the change in the purge time of the cycle. Also, we can corroborate the previous observation that the Langmuir-Freundlich model with $K_3=10^{-4}$ predicts the pressure well with the experiments, whereas the Langmuir-Freundlich (b_n corrected) with $K_3=10^{-5}$ predicts the oxygen purity within the error bar.

With the completion of simulations pertaining to the variation in pressurisation and purge times, we now characterise the influence of the equalisation time. For these simulations, the pressurisation and purge times were 26 s and 1.5 s, respectively. Figures 4.26a, 4.26b, and 4.27 show the pressure curves for two cylinders and oxygen purity at the outlet for the equilibrium time of 3 s whereas similar plots for 5 s are shown in Figs. 4.28a, 4.28b, and 4.29, respectively. Once again, we can corroborate the variation observed in the experiments and the inference on the performance of different adsorption isotherms.

All these simulations convincingly prove the aptness and usefulness of the present numerical model, both in terms of its ability to reproduce experimental physics and as a potent tool for developing newer designs.

4.6 Conclusion

In the current work, a comprehensive numerical model of the PSA plant has been developed to reproduce the experimental findings. This model realistically conserves quantities such as mass, momentum, species transport, and energy. Additional source terms are added to these conservation equations to account for the adsorption/desorption process inside the adsorbent bed. Ergun's equation was utilised to incorporate the flow transports in the porous media.

Before modelling the complete PSA plant, three sample cases from the literature were considered for validating the tailor-made model. For all three cases, a good agreement was observed. In order to optimise the effort to perform the numerical modelling, the complete

PSA plant was converted into an axisymmetric geometry, and different solenoidal valve configurations were replicated via modifications to the boundary conditions and interfaces.

We have also tried to address the discrepancies in the data for various adsorption models, particularly the Langmuir-Freundlich isotherm model. In this regard, we have conducted simulations involving four adsorption models. A systematic parametric study involving the variation in pressurisation, purge, and equalisation times was carried out, and the results were compared with the corresponding experimental data.

Chapter 5

Summary and scope for extension

In order to address the medical oxygen shortage during the second wave of the pandemic, a portable mini-pressure swing adsorption plant has been developed in the current for small hospital use in tier II/tier III cities. The important outcomes of the present work are listed as follows.

- The current work has shown a classic example of developing a commercially viable prototype starting from tabletop experimental setups. In the present work, the first tabletop version of the device gave a purity of 90.3% at 1 sLPM, whereas the final prototype was gradually scaled to yield 45 ± 1 sLPM of flow at 90.9% oxygen purity. This prototype can support up to 6-8 beds in a small hospital setup.

- The performance of the modified PSA cycle in the device was controlled by the three flow times, i.e., pressurisation time: duration of pressurisation and depressurisation (adsorption/desorption) of the zeolite tank, purge time: duration for flushing out the remaining nitrogen from the zeolite tank, and equalisation time: duration for the equalising the pressure among the two zeolite cylinder to conserve energy. For any flow rate, these three times must be optimised to get the maximum oxygen recovery at the outlet. Interestingly, the device's behaviour is insensitive to the change in pressurisation, purge and equalisation times for lower flow rates. However, for higher flow rates, the performance and recovery of the device are sensitive to the change in the three times.

- The ratio of length and diameter of the zeolite tank is an important parameter which governs the overall performance of the PSA plants. There is an optimum value of this ratio, between 4 and 6, for which the system exhibits the best performance. It was observed that a shorter L/d ratio of the zeolite cylinder would lead to a mal-distribution of flow inside the tank, and there would be less utilisation of zeolite for nitrogen adsorption. On the contrary, a large L/d ratio would lead to a significant drop in the pressure across the zeolite tank. Hence, the pressure ratio upon which the adsorption and desorption take place decreases significantly, reducing the oxygen recovery.

- It was observed that the dead volume of the zeolite cylinder should be as low as possible to significantly reduce the trapping of nitrogen inside the void spaces of the zeolite cylinder. A significant reduction of performance was observed in one of the designs where the dead volume was approximately 22.2% of the total volume of the cylinder. However, reducing this factor to 0.16% increased the oxygen recovery at higher flow rates.
- Alongside the prototype development and experimental analysis, detailed numerical modelling for a PSA plant using an axisymmetric geometry has been developed in the current work. The simulation process involved solving all the relevant conservation equations using ANSYS FLUENT, wherein user-defined functions were used to incorporate the adsorption and desorption processes.
- A thorough and detailed study was performed to address the discrepancies in the adsorption isotherm models in the published literature. It was observed that the Langmuir-Freundlich adsorption isotherm with $K_3=10^{-5}$ underpredicts the experimentally measured oxygen purity limit. The adsorption isotherm models, Langmuir-Freundlich adsorption isotherm with $K_3=10^{-5}$, Langmuir-Freundlich adsorption isotherm (b_n corrected) with $K_3=10^{-5}$ exhibit the saturation of the pressure curve and they exceed the experimentally measured pressure due to the weak adsorption. Alternatively, the adsorption isotherm model Langmuir-Freundlich with $K_3=10^{-4}$ matched well with the experimental pressure curves. Langmuir-Freundlich adsorption isotherm (b_n corrected) with $K_3=10^{-5}$ did a decent job in predicting oxygen purity at different conditions.
- Eventually, we have been able to successfully develop a design tool that could reproduce the experimental results. This can be used for further optimisation of the device.

5.1 Scope for future work

There are many avenues by which the scope of the present work can be extended. These include

- Extention leading to analysis of other adsorbents for sequestration of other gas components. One could use Carbon molecular sieves to purify nitrogen from the air. This could involve both experimental and numerical analysis, for which the current work acts as a baseline.
- Study involving other design configurations and operation parameters. In the present work, optimisation of pressurisation, purge, and equalisation times was essentially performed for the flow rate of 41.69 sLPM. Nevertheless, it can be further extended to more pressurisation, purge and equalisation time for higher flow rates and newer designs.
- Apart from newer gases, the current PSA cycle can also be modified to attain better purity and recovery from the device. For example, it is possible to obtain oxygen as pure as 99

References

[1] Ackley, M. (2019). Medical oxygen concentrators: a review of progress in air separation technology. *Adsorption*, 25:1–38.

[2] Ahari, J. S., Pakseresht, S., Mahdyarfar, M., Shokri, S., Zamani, Y., Pour, A. N., and Naderi, F. (2006). Predictive dynamic model of air separation by pressure swing adsorption. *Chemical engineering & technology*, 29(1):50–58.

[3] Akulinin, E., Golubyatnikov, O., Dvoretsky, D., and Dvoretsky, S. (2019). Numerical study of cyclic adsorption processes of air oxygen enrichment in dynamics. In *Journal of Physics: Conference Series*, volume 1278, page 012005. IOP Publishing.

[4] Akulinin, E., Golubyatnikov, O., Dvoretsky, D., and Dvoretsky, S. (2020). Optimization and analysis of pressure swing adsorption process for oxygen production from air under uncertainty. *Chemical Industry and Chemical Engineering Quarterly*, 26(1):89–104.

[5] Alpay, E. and Scott, D. (1992). The linear driving force model for fast-cycle adsorption and desorption in a spherical particle. *Chemical engineering science*, 47(2):499–502.

[6] Andrews, M., Areekal, B., Rajesh, K., Krishnan, J., Suryakala, R., Krishnan, B., Muraly, C., and Santhosh, P. (2020). First confirmed case of covid-19 infection in india: A case report. *The Indian journal of medical research*, 151(5):490.

[7] ANSYS (2016). Ansys fluent - cfd software | ansys.

[8] Arora, A. and Hasan, M. (2021). Flexible oxygen concentrators for medical applications. *Scientific Reports*, 11(1):1–14.

[9] Arvind, R., Farooq, S., and Ruthven, D. (2002). Analysis of a piston psa process for air separation. *Chemical Engineering Science*, 57(3):419–433.

[10] Bechaud, C., Melen, S., Lasseux, D., Quintard, M., and Bruneau, C. (2001). Stability analysis of a pressure swing adsorption process. *Chemical engineering science*, 56(10):3123–3137.

[11] Beeyani, A., Singh, K., Vyas, R., and Kumar, S. (2010). Parametric studies and simulation of psa process for oxygen production from air. *Polish journal of chemical technology*, 12(2):18–28.

[12] Ben-Mansour, R., Qasem, N. A., and Antar, M. A. (2018). Carbon dioxide adsorption separation from dry and humid co2/n2 mixture. *Computers & Chemical Engineering*, 117:221–235.

[13] Berlin, N. H. (1966). Method for providing an oxygen-enriched environment. US Patent 3,280,536.

[14] Bliss, P. L., Atlas, C. R., and Halperin, S. C. (2010). Portable oxygen concentrator. US Patent 7,837,761.

[15] Bonjour, J., Chalfen, J.-B., and Meunier, F. (2002). Temperature swing adsorption process with indirect cooling and heating. *Industrial & engineering chemistry research*, 41(23):5802–5811.

[16] Budner, Z., Dula, J., Podstawa, W., and Gawdzik, A. (1999). Study and modelling of the vacuum swing adsorption (vsa) process employed in the production of oxygen. *Chemical Engineering Research and Design*, 77(5):405–412.

[17] Burns, T. D., Pai, K. N., Subraveti, S. G., Collins, S. P., Krykunov, M., Rajendran, A., and Woo, T. K. (2020). Prediction of mof performance in vacuum swing adsorption systems for postcombustion co2 capture based on integrated molecular simulations, process optimizations, and machine learning models. *Environmental science & technology*, 54(7):4536–4544.

[18] Cen, P. and Yang, R. T. (1985). Separation of a five-component gas mixture by pressure swing adsorption. *Separation Science and Technology*, 20(9-10):725–747.

[19] Chai, S. W., Kothare, M. V., and Sircar, S. (2011). Rapid pressure swing adsorption for reduction of bed size factor of a medical oxygen concentrator. *Industrial & Engineering chemistry research*, 50(14):8703–8710.

[20] Chan, K. C., Chao, C. Y., and Wu, C. (2015). Measurement of properties and performance prediction of the new mwcnt-embedded zeolite 13x/cacl2 composite adsorbents. *International Journal of Heat and Mass Transfer*, 89:308–319.

[21] Chang, C.-S., Ni, S.-H., Yang, H.-S., and Chou, C.-T. (2021). Simulation study of separating oxygen from air by pressure swing adsorption process with semicylindrical adsorber. *Journal of the Taiwan Institute of Chemical Engineers*, 120:67–76.

[22] Chiang, A., Chung, Y., Cheng, C.-W., Hung, T.-H., and Lee, T. (1994). Experimental study on a four-bed psa air separation process. *AIChE journal*, 40(12):1976–1982.

[23] Chica, A. (2013). Zeolites: promised materials for the sustainable production of hydrogen. *International Scholarly Research Notices*, 2013.

[24] Chou, C.-t. and Huang, W.-C. (1994). Simulation of a four-bed pressure swing adsorption process for oxygen enrichment. *Industrial & engineering chemistry research*, 33(5):1250–1258.

[25] Dantas, T. L., Luna, F. M. T., Silva Jr, I. J., de Azevedo, D. C., Grande, C. A., Rodrigues, A. E., and Moreira, R. F. (2011). Carbon dioxide–nitrogen separation through adsorption on activated carbon in a fixed bed. *Chemical Engineering Journal*, 169(1-3):11–19.

[26] Das, N. K., Chaudhuri, H., Bhandari, R. K., Ghose, D., Sen, P., and Sinha, B. (2008). Purification of helium from natural gas by pressure swing adsorption. *Current Science*, pages 1684–1687.

[27] De, M. P. G. and Daniel, D. (1964). Process for separating a binary gaseous mixture by adsorption. US Patent 3,155,468.

[28] De Klerk, A. (2003). Voidage variation in packed beds at small column to particle diameter ratio. *AIChE journal*, 49(8):2022–2029.

[29] Doong, S. and Yang, R. (1987). A comparison of gas separation performance by different pressure swing adsorption cycles. *Chemical Engineering Communications*, 54(1-6):61–71.

[30] Dubois, A., Bodelin, P., and Vigor, X. (2003). Portable oxygen concentrator. US Patent 6,520,176.

[31] Engineer09, W. C. (2021). Cryogenic oxygen plant. [Online; accessed 30-December-2021].

[32] Ferreira, D., Barcia, P., Whitley, R. D., and Mendes, A. (2015). Single-stage vacuum pressure swing adsorption for producing high-purity oxygen from air. *Industrial & Engineering Chemistry Research*, 54(39):9591–9604.

[33] Fluent, I. (2002). Fluent 14.5 user guide. *Fluent Inc., Lebanon. NH-03766*.

[34] Google (2021). Covid oxygen crisis statistics. [Online].

[35] Haghpanah, R., Majumder, A., Nilam, R., Rajendran, A., Farooq, S., Karimi, I. A., and Amanullah, M. (2013). Multiobjective optimization of a four-step adsorption process for postcombustion co2 capture via finite volume simulation. *Industrial & Engineering Chemistry Research*, 52(11):4249–4265.

[36] Hamed, H. H. (2015). Oxygen and nitrogen separation from air using zeolite type 5a. *Al-Qadisiyah Journal for Engineering Sciences*, 8(2):147–158.

[37] Hasan, M. F., Karimi, I., Farooq, S., Rajendran, A., and Amanullah, M. (2011). Surrogate-based vsa process optimization for post-combustion co2 capture. In *Computer Aided Chemical Engineering*, volume 29, pages 402–406. Elsevier.

[38] Hirschfelder, J. O., Curtiss, C. F., and Bird, R. B. (1964). Molecular theory of gases and liquids. *Molecular theory of gases and liquids*.

[39] Hosseinzadeh Hejazi, S. A., Estupinan Perez, L., Rajendran, A., and Kuznicki, S. (2017). Cycle development and process optimization of high-purity oxygen production using silver-exchanged titanosilicates. *Industrial & Engineering Chemistry Research*, 56(19):5679–5691.

[40] Hosseinzadeh Hejazi, S. A., Rajendran, A., Sawada, J. A., and Kuznicki, S. M. (2016). Dynamic column breakthrough and process studies of high-purity oxygen production using silver-exchanged titanosilicates. *Industrial & Engineering Chemistry Research*, 55(20):5993–6005.

[41] Jagger, T. W., Van Brunt, N. P., Kivisto, J. A., and Lonnes, P. B. (2011). Ambulatory oxygen concentrator containing a three phase vacuum separation system. US Patent 8,020,553.

[42] Jee, J.-G., Lee, J.-S., and Lee, C.-H. (2001). Air separation by a small-scale two-bed medical o2 pressure swing adsorption. *Industrial & engineering chemistry research*, 40(16):3647–3658.

[43] Jee, J.-G., Lee, S.-J., Kim, M.-B., and Lee, C.-H. (2005). Three-bed pvsa process for high-purity o2 generation from ambient air. *AIChE journal*, 51(11):2988–2999.

[44] Juntgen, H., Knoblauch, K., Reichenberger, J., Heimbach, H., and Tarnow, F. (1981). Process for the recovery of nitrogen-rich gases from gases containing at least oxygen as other component. US Patent 4,264,339.

[45] Kakavandi, I. A., Shokroo, E., Baghbani, M., and Farniaei, M. (2017). Dynamic modeling of nitrogen adsorption on zeolite 13x bed. *Fluid Mech Res Int*, 1(1):00004.

[46] Kim, Y. H., Lee, D. G., Moon, D. K., Byeon, S.-H., Ahn, H. W., and Lee, C. H. (2014). Effect of bed void volume on pressure vacuum swing adsorption for air separation. *Korean Journal of Chemical Engineering*, 31(1):132–141.

[47] Knaebel, K. S. and Hill, F. B. (1985). Pressure swing adsorption: development of an equilibrium theory for gas separations. *Chemical Engineering Science*, 40(12):2351–2360.

[48] Kratz, W. C. and Sircar, S. (1984). Pressure swing adsorption process for a medical oxygen generator for home use. US Patent 4,477,264.

[49] Krishnamurthy, S., Haghpanah, R., Rajendran, A., and Farooq, S. (2014). Simulation and optimization of a dual-adsorbent, two-bed vacuum swing adsorption process for co2 capture from wet flue gas. *Industrial & Engineering Chemistry Research*, 53(37):14462–14473.

[50] Le Bec, R. (2005). Method for purifying hydrogen-based gas mixtures using a calcium x-zeolite. US Patent 6,849,106.

[51] Lee, C.-H., Yang, J., and Ahn, H. (1999). Effects of carbon-to-zeolite ratio on layered bed h2 psa for coke oven gas. *AIChE journal*, 45(3):535–545.

[52] Lee, S.-J., Jung, J.-H., Moon, J.-H., Jee, J.-G., and Lee, C.-H. (2007). Parametric study of the three-bed pressure- vacuum swing adsorption process for high purity o2 generation from ambient air. *Industrial & engineering chemistry research*, 46(11):3720–3728.

[53] Lü, Y., Doong, S.-J., and Bülow, M. (2005). Tuning of pressure swing adsorption systems based on differential pressure profile. *Adsorption*, 11(3):315–324.

[54] Mahdi, A. H., Ahmed, S. M., Salih, S. S., and Ayuob, H. S. (2020). Simulation study of two units of pressure swing adsorption for producing oxygen and nitrogen simultaneously. In *AIP Conference Proceedings*, volume 2213, page 020166. AIP Publishing LLC.

[55] Makarem, M. A., Mofarahi, M., Jafarian, B., and Lee, C.-H. (2019). Simulation and analysis of vacuum pressure swing adsorption using the differential quadrature method. *Computers & Chemical Engineering*, 121:483–496.

[56] Malek, A. and Farooq, S. (1996). Comparison of isotherm models for hydrocarbon adsorption on activated carbon. *AIChE Journal*, 42(11):3191–3201.

[57] Malek, A. and Farooq, S. (1998). Hydrogen purification from refinery fuel gas by pressure swing adsorption. *AIChE Journal*, 44(9):1985–1992.

[58] Maruyama, R. T., Pai, K. N., Subraveti, S. G., and Rajendran, A. (2020). Improving the performance of vacuum swing adsorption based co2 capture under reduced recovery requirements. *International Journal of Greenhouse Gas Control*, 93:102902.

[59] Mendes, A. M., Costa, C. A., and Rodrigues, A. E. (2000). Analysis of nonisobaric steps in nonlinear bicomponent pressure swing adsorption systems. application to air separation. *Industrial & engineering chemistry research*, 39(1):138–145.

[60] Mofarahi, M. and Shokroo, E. J. (2013). Comparison of two pressure swing adsorption processes for air separation using zeolite 5a and zeolite 13x. *Petroleum & coal*, 55(3).

[61] Moran, A. and Talu, O. (2018). Limitations of portable pressure swing adsorption processes for air separation. *Industrial & Engineering Chemistry Research*, 57(35):11981–11987.

[62] Murali, R. S., Sankarshana, T., and Sridhar, S. (2013). Air separation by polymer-based membrane technology. *Separation & Purification Reviews*, 42(2):130–186.

[63] Murray, J. W. (1997). *Air separation by rapid pressure swing adsorption*. PhD thesis, University of Cambridge.

[64] Occhialini, J. M., Whitley, R. D., Wagner, G. P., Labuda, M. J., and Steigerwalt, C. E. (2007). Weight-optimized portable oxygen concentrator. US Patent 7,279,029.

[65] Pan, M., Omar, H. M., and Rohani, S. (2017). Application of nanosize zeolite molecular sieves for medical oxygen concentration. *Nanomaterials*, 7(8):195.

[66] Papai, I., Goursot, A., Fajula, F., Plee, D., and Weber, J. (1995). Modeling of n2 and o2 adsorption in zeolites. *The Journal of Physical Chemistry*, 99(34):12925–12932.

[67] Ramamurthy, V., Shailaja, J., Kaanumalle, L. S., Sunoj, R., and Chandrasekhar, J. (2003). Controlling chemistry with cations: photochemistry within zeolites. *Chemical communications*, (16):1987–1999.

[68] Rao, V. R., Kothare, M. V., and Sircar, S. (2014). Novel design and performance of a medical oxygen concentrator using a rapid pressure swing adsorption concept. *AIChE Journal*, 60(9):3330–3335.

[69] Rege, S. U. and Yang, R. T. (1997). Limits for air separation by adsorption with lix zeolite. *Industrial & engineering chemistry research*, 36(12):5358–5365.

[70] Roy, S. and Moharir, A. S. (2019). Modeling the generic breakthrough curve for adsorption process. *arXiv preprint arXiv:1907.00195*.

[71] Sanni, E. S., Sadiku, E. R., and Okoro, E. E. (2021). Novel systems and membrane technologies for carbon capture. *International Journal of Chemical Engineering*, 2021.

[72] Santos, J., Portugal, A., Magalhaes, F., and Mendes, A. (2006). Optimization of medical psa units for oxygen production. *Industrial & engineering chemistry research*, 45(3):1085–1096.

[73] Shin, H.-S., Kim, D.-H., Koo, K.-K., and Lee, T.-S. (2000). Performance of a two-bed pressure swing adsorption process with incomplete pressure equalization. *Adsorption*, 6(3):233–240.

[74] Shokroo, E. J., Farsani, D. J., Meymandi, H. K., and Yadollahi, N. (2016). Comparative study of zeolite 5a and zeolite 13x in air separation by pressure swing adsorption. *Korean Journal of Chemical Engineering*, 33(4):1391–1401.

[75] Sircar, S. (1988). Fractionation of multicomponent gas mixtures by pressure swing adsorption. US Patent 4,790,858.

[76] Sircar, S. and Hufton, J. (2000). Why does the linear driving force model for adsorption kinetics work? *Adsorption*, 6:137–147.

[77] Smith, J. (1980). Barrer. zeolites and clay minerals as sorbents and molecular sieves. london and new york (academic press), 1978 viii+ 497 pp., 181 figs. price£ 25.00. *Mineralogical Magazine*, 43(330):829–830.

[78] Soo, C., Lai, Y., Chuah, T., Mustapha, S., and Choong, T. (2005). On the effect of axial dispersion in the numerical simulation of fast cycling adsorption processes. *Jurnal Teknologi*, pages 1â–13.

[79] Stocker, J., Whysall, M., and Miller, G. (1998). years of psa technology for hydrogen purification. *UOP LLC*.

[80] Subramanian Balashankar, V. and Rajendran, A. (2019). Process optimization-based screening of zeolites for post-combustion co2 capture by vacuum swing adsorption. *ACS Sustainable Chemistry & Engineering*, 7(21):17747–17755.

[81] Taveira, A. P. G. and Mendes, A. M. M. (2008). Xenon external recycling unit for recovery, purification and reuse of xenon in anaesthesia circuits. US Patent 7,442,236.

[82] Todd, R. S. and Webley, P. A. (2006). Mass-transfer models for rapid pressure swing adsorption simulation. *AIChE journal*, 52(9):3126–3145.

[83] W John Thomas, F. and Crittenden, B. (1998). *Adsorption technology and design*. Butterworth-Heinemann.

[84] Wang, J. and Guo, X. (2020). Adsorption isotherm models: Classification, physical meaning, application and solving method. *Chemosphere*, 258:127279.

[85] Webley, P. A. and He, J. (2000). Fast solution-adaptive finite volume method for psa/vsa cycle simulation; 1 single step simulation. *Computers & Chemical Engineering*, 23(11-12):1701–1712.

[86] Whitley, R. D., Wagner, G. P., and Labuda, M. J. (2007). Dual mode medical oxygen concentrator. US Patent 7,273,051.

[87] Xu, J., Rarig, D. L., Cook, T. A., Hsu, K.-K., Schoonover, M., and Agrawal, R. (2003). Pressure swing adsorption process with reduced pressure equalization time. US Patent 6,565,628.

[88] Xu, J. and Weist Jr, E. L. (2002). Six bed pressure swing adsorption process with four steps of pressure equalization. US Patent 6,454,838.

[89] Yang, J., Park, M.-W., Chang, J.-W., Ko, S.-M., and Lee, C.-H. (1998). Effects of pressure drop in a psa process. *Korean Journal of Chemical Engineering*, 15(2):211–216.

[90] Yang, R. T. (1994). Pressure swing adsorption by dm ruthven, s. farooq, ks knaebel. *Chemical Engineering Education*, 28(3):192–193.

[91] Yang, R. T. (1997). *Gas separation by adsorption processes*, volume 1. World Scientific.

[92] Yang, R. T. (2003). *Adsorbents: fundamentals and applications*. John Wiley & Sons.

[93] Yang, X., Wang, H., Chen, J., Li, Z., Liu, Y., Zhang, C., and Xing, Y. (2019). Two-dimensional modeling of pressure swing adsorption (psa) oxygen generation with radial-flow adsorber. *Applied Sciences*, 9(6):1153.

[94] Zhang, J., Webley, P. A., and Xiao, P. (2005). Experimental pilot-scale study of carbon dioxide recovery from flue gas streams by vacuum swing adsorption. In *AIChE Annual Meeting 2005*, page 2302. AIChE.

[95] Zheng, X., Liu, Y., and Liu, W. (2010). Two-dimensional modeling of the transport phenomena in the adsorber during pressure swing adsorption process. *Industrial & engineering chemistry research*, 49(22):11814–11824.

[96] Zhu, X., Sun, Y., Liu, Y., Sun, X., and Shi, J. (2022). Experimental performance analysis of vacuum pressure swing adsorption air separation process under plateau special conditions. *Separation Science and Technology*, pages 1–9.